Control of spin dynamics for applications in Nuclear Magnetic Resonance

Thesis advisor

Navin Khaneja

Author

Van Do Mai Koroleva

Control of spin dynamics for applications in Nuclear Magnetic Resonance

Abstract

Sophisticated electromagnetic pulse sequences that control spin dynamics have been developed in Nuclear Magnetic Resonance (NMR) over the last few decades. However, due to more and more demanding criteria, such as unknown parameters, larger bandwidths, higher signal to noise ratio (SNR), less power consumption, etc., new pulse sequences are constantly needed. This thesis presents new pulse sequences for several important applications of NMR.

We first study the problem of decoupling two homonuclear spins that are coupled by weak isotropic scalar coupling. Most existing approaches employ selective irradiation targeting one of the spins. Selective irradiation, however, is not applicable when the resonance frequencies of the spins are unknown or not well separated. We describe non-selective pulse sequences that eliminate the coupling. In our design, the chemical shifts are scaled down by a known factor, allowing us to reconstruct their true values. Decoupling is achieved when the difference in the effective chemical shifts is sufficiently larger than the coupling strength.

We next modify the pulse sequence found above to reduce coupling between spins in quantum registers. Being a global pulse, i.e. applicable to all spins in one operation, it has low complexity and therefore has a clear advantage over non-global pulses. With

the application of a gradient field, Ising coupling in a coupled multi-spin system with nearest-neighbor coupling can be reduced, potentially resulting in prolonged coherence.

Finally, we investigate an echo-generating sequence called the CPMG sequence in applications where the dispersion in the static field is much larger than the amplitude of the irradiation. The CPMG sequence is commonly used in the exploration of oil and gas reserves to study earth formations. We find a new class of symmetric-phase-alternating refocusing pulses that significantly increase the SNR with little increase in power consumption. These pulses, when matched with suitable finite-amplitude excitation pulses, increase the SNR by over threefold.

Using tools from control theory and optimization, the pulse sequences found in this thesis are one step forward in the continuing quest for better NMR pulse sequences.

Contents

Title Page i
Abstract iii
Table of Contents v
List of Figures vii
List of Tables xi
Citations to Previously Published Work xii
Acknowledgments xiii

1 Introduction **1**

2 Review of NMR concepts and mathematical methods **8**
2.1 Representation of spins in quantum mechanics 8
2.1.1 Spin-$\frac{1}{2}$ operators 9
2.1.2 Measurement and density matrix 11
2.1.3 The spin Hamiltonian 14
2.2 Chemical shift 15
2.3 Bloch equation 16
2.4 Relaxation 18
2.5 Average Hamiltonian 19

3 Homonuclear decoupling in liquid-state NMR **23**
3.1 Overview of coupling 23
3.2 Ising coupling 28
3.2.1 The 4-segment pulse sequence 33
3.2.2 Simulation results 37
3.3 Isotropic coupling - weaker coupling strength 40
3.3.1 The 6-segment pulse sequence 41
3.3.2 Scaling of the frequency offsets 44
3.3.3 Compensating cycle for the case of unknown ω^- 45
3.3.4 Simulation results 46
3.3.5 Discussion 49

3.4 Isotropic coupling - stronger coupling strength 50
3.4.1 Compensation for unknown chemical shift difference 57
3.4.2 Scaling of the frequency offsets and rf amplitude modulation . 58
3.4.3 Simulation results 59
3.5 Discussion of experimental issues 59
3.6 Conclusion and outlook 63

4 Reducing coupling between quantum bits using global pulses 65
4.1 Introduction 65
4.2 Reducing decoherence with global pulses 68

5 New refocusing and excitation pulses for the CPMG sequence 76
5.1 NMR well logging 76
5.2 CPMG sequence 77
5.3 Challenges in improving signal-to-noise ratio 80
5.4 Spin dynamics in inhomogeneous fields 81
5.5 Method of optimizing SNR 84
5.6 Short refocusing pulses 89
5.6.1 Short Symmetric Phase Alternating pulses 89
5.6.2 Experimental verification 96
5.6.3 Summary 101
5.7 Excitation pulse 101
5.7.1 AMEX pulses 103
5.7.2 Phase cycling 107
5.7.3 Experimental verification 110
5.8 Conclusion 110

Bibliography 113

List of Figures

1.1 The basic components of an NMR experiment 5

3.1 (a) shows the evolution of the rf Hamiltonian for spin I in the toggling frame of the chemical shift Hamiltonian. The four stages of the cycle, corresponding to the chemical shift Hamiltonian being $(\omega_I I_z + \omega_S S_z)$, $-(\omega_I I_z + \omega_S S_z)$, $-(\omega_I I_z + \omega_S S_z)$ and $(\omega_I I_z + \omega_S S_z)$, are numbered in the figure. (b) shows a block of the 4-segment pulse sequence that makes the chemical shift and the rf Hamiltonian execute the cycle in (a). This basic building block is repeated throughout the decoupling time. Short windows of free evolution to acquire the signal are denoted by the arrow in the figure. 34

3.2 The coordinate transformation that aids the calculation of the effective field and coupling strength. 36

3.3 This figure shows the simulation results for the Ising coupling. The parameters used are $\omega_I/(2\pi) = 0.5$ kHz, $\omega_S/(2\pi) = 1$ kHz, $J/(2\pi) = 10$ Hz, $\Delta t = 31.8$ μs, $A/(2\pi) = 1$ kHz, $\theta = 1/5$. The observation time is 2 s. All π pulses are assumed to be ideal delta pulses with negligible durations. The first row shows the results for the coupled system. The second row shows the results for the decoupled system due to the application of the 4-segment decoupling sequence. (a) and (d) show the evolution of the total magnetization of spin I, $\sqrt{\langle I_x\rangle^2 + \langle I_y\rangle^2 + \langle I_z\rangle^2}$. In (d), the red circles are the plot of $\cos(\theta^2 Jt/6)$, which perfectly matches the simulation result. (b) and (e) show the evolution of the total x-magnetization of the two spins (the FID signal). (c) and (f) show the Fourier transform of the FID. The locations of the peaks are exactly as expected. It is clear that the applied pulse sequence shows great improvement in preserving the magnetization and increasing the intensity of the peaks. 38

3.4 (a) plots $\sqrt{\langle I_x\rangle^2 + \langle I_y\rangle^2 + \langle I_z\rangle^2}$ as a function of time under the application of the 4-segment pulse sequence. The red, slowly decaying curve shows the result for the Ising system, and the blue, fast oscillating curve shows the result for the isotropic system. (b) shows the conception of the new sequence by examining the evolution of the planar coupling in the interaction frame of the Zeeman terms. The 4-segment pulse sequence represented by four small arcs, numbered 1, 2, 3, 6, creates $I_xS_x + I_yS_y$ in the positive direction. The two additional free evolution times represented by the two large arcs, numbered 4, 5, create $I_xS_x + I_yS_y$ in the negative direction. 41

3.5 Almost linear scaling of the frequency offsets for the 6-segment pulse sequence. The horizontal axis shows the frequency $\omega/(2\pi)$. The vertical axis shows the scaled frequency $\mathrm{sinc}^2\left(\frac{\omega\Delta t}{2}\right)\frac{A\Delta t}{2}\frac{\omega}{2\pi}$. In this plot $\Delta t = 50\mu$s. $A/(2\pi) = 1$ kHz. 46

3.6 A basic building block of the 6-segment decoupling pulse sequence that is repeated throughout the decoupling time. The free evolution times τ_i vary for different blocks and are determined by minimizing the quantity in Eq. (3.51). 47

3.7 The first row shows the signal and spectrum of a coupled system with isotropic coupling $J/(2\pi) = 10$ Hz, $\omega_I/(2\pi) = 1$ kHz, $\omega_S/(2\pi) = 2$ kHz. The remaining rows show the results due to decoupling for a system that has $J/(2\pi) = 10$ Hz, $\omega_I/(2\pi) = 1$ kHz, $\omega_S/(2\pi) = [2, 2.1, 2.2, 2.3, 2.4, 2.5]$ kHz. The first column plots $\sqrt{\langle I_x\rangle^2 + \langle I_y\rangle^2 + \langle I_z\rangle^2}$, the second column plots the Fourier transform of the FID signal $\langle I_x + S_x\rangle$. The designed parameters are $\Delta t = 50\ \mu s$, $A/(2\pi) = 1$ kHz, $\{\tau_i\} = \{0.4434, 0.5197, 0.6151, 0.9511\}$ ms. All π pulses are ideal δ pulses with negligible durations. The results show the robustness of the pulse sequence over the dispersion of the chemical shift difference. 48

3.8 Nonlinear scaling of the frequency offsets under modulation of Δt and rf amplitudes. The horizontal axis shows $\omega/(2\pi)$, the vertical axis shows $\omega_{\text{scaled}}/(2\pi)$ according to Eq. (3.78). For this plot, $\Delta t = [0.1650,\ 0.5309,\ 0.4900,\ 0.8739]$ ms, $A/(2\pi) = [200,\ 100,\ 120,\ 60]$ Hz. 60

3.9 The first row shows the signal and spectrum of a coupled system that has chemical shift difference equal to 1 kHz and frequency offsets located at 0.6 and 1.6 kHz. The spectrum consists of two doublets each with 2 peaks separated by the coupling strength. The remaining rows show the results due to decoupling for a system that has frequency offsets $\omega_I/(2\pi) = 0.6$ kHz, $\omega_S/(2\pi) = [1.6,\ 1.7,\ 1.8,\ 1.9,\ 2.0,\ 2.1]$ kHz. The first column plots $\sqrt{\langle I_x\rangle^2 + \langle I_y\rangle^2 + \langle I_z\rangle^2}$, and the second column plots the Fourier transform of the FID signal $\langle I_x + S_x\rangle$. The designed parameters are $\Delta t = [0.1650,\ 0.5309,\ 0.4900,\ 0.8739]$ ms, $A/(2\pi) = [200,\ 100,\ 120,\ 60]$ Hz. All π pulses are ideal δ pulses. In all cases , $J/(2\pi) = 20$ Hz, which is twice as big as the coupling in the 6-segment pulse sequence case. The results show the robustness of our pulse sequence over the dispersion of the chemical shift difference. . 61

4.1 Spin topology: (a) Linear Chain (b) Square Lattice 68
4.2 Periodic gradient magnetic field on a spin chain. 68
4.3 Pulse sequence for decoupling. 71
4.4 he simulation was on a square lattice with four qubits, the coupling strengths of four edges of this lattice follow independent normal distributions with mean values $2\pi[10, 12.1, 11.4, 9.2]$ and variance equal to the square of mean of the mean values $\bar{J} = 10.7$ Hz. The Zeeman splitting caused by the gradient field is $2\pi 10^4[1.729, 3.235, 1.0, 3.24]$ respectively, $\Delta t = 10^{-7}$, $\theta = \frac{1}{20}$, $A \approx 2\pi 8 \times 10^3 = 8kHz$. The blue line shows the fidelity without the decoupling pulses, the red circles show the fidelity with the application of the decoupling pulses. 74

5.1 (a) Illustration of the CPMG sequence. t_E is the echo spacing. t_p is the length of the refocusing pulse. For a rectangular pulse, $t_p = \frac{1}{2A}$, where A is the rf. amplitude measured in Hz. τ indicates a free precession period.(b) The echo peaks decay exponentially with time constant T_2 caused by the spin-spin relaxation. 78
5.2 Profile of an SPA pulse. A is the nominal rf amplitude. The pulse has constant amplitude and alternating phases $-y$ and y. A rectangular hard pulse corresponds to $\alpha = 0$, $\beta = \pi$. 91
5.3 $\sum \hat{n}_y^2$ for different combinations of α and β. The color bar shows improving performance in the upward direction. 92
5.4 $\hat{n}_y^2$ over the field inhomogeneities for different pulses. The echo spacing is $t_E = 6t_{180} + t_p$, where t_p is the corresponding pulse duration. A is the nominal rf. amplitude. 93
5.5 The asymptotic echo shape for different pulses with rf. inhomogeneity assuming a perfect initial 90° pulse. A is the nominal rf. amplitude . 94

5.6 SNR in the presence of rf inhomogeneity. SNR normalized to the SNR of the standard refocusing pulse at the nominal rf amplitude A. A perfect 90° excitation pulse is assumed. The SPA pulses are clearly less sensitive to mis calibration of rf. amplitude than the standard 180° pulse. The acquisition window is $t_p + 6t_{180}$, where t_p is the pulse length. 95
5.7 Asymptotic echo shapes produced by different excitation and refocusing pulses. The left figure shows the result obtained by simulation, while the right one shows the experimental results. The peak amplitude for each echo is normalized with respect to that of the standard CPMG sequence. The sample was dionized (DI) water with transverse relaxation time $T_2 = 1.9$ s. $t_{180} = 500\mu$ s. The echo spacing was 6.5 ms. The acquisition time for each echo was 3.07 ms long. Data taken with permission from the co-authors in [1] 98
5.8 Asymptotic magnetization, the y component of $\vec{M}_{asy}$, produced by different excitation and refocusing pulses. The left figure shows the results obtained by simulation, while the right one shows the experimental results. The sample was deionized (DI) water with transverse relaxation time T_2= 1.9 sec. $t_{180} = 500\mu$ s. The echo spacing was 6.5 ms. The acquisition time for each echo was 3.07 ms long. Data taken with permission from the co-authors in [1] 99
5.9 Measured echo amplitudes of (a) NiCl solution with $T_1 = T_2$ and (b) skim milk with $T_1 > T_2$. The echo amplitudes are normalized with respect to the amplitudes extrapolated to $t = 0$. Data taken with permission from the coauthors in Ref. [2]. 100
5.10 Amplitude and phase of $AMEX_{SPA,0}$. The nominal rf amplitude used is $A = 5kHz$. Therefore, $t_{180} = 100\mu$ s. The pulse is 1 ms long. 104
5.11 Comparison of the echo shapes generated from 3126 spins in a constant gradient. The green curves show the echo shape of the standard refocusing pulse with a hard 90° pulse and a reduced delay free precession time t_{180}/π. The red curves show the echo shape of SPA-1.0 with the new excitation pulse. The solid curves show the in phase components, while the dotted curves show the out of phase components. 105
5.12 Echo shapes for different pairs of excitation and refocusing pulses. Black curves show the results obtained by simulation. Red curves are experimental data for the in-phase components. Blue curves are experimental data for the out-of-phase components, which are almost identically zero as expected. Data were taken with permission from the co authors in Ref. [3] 111
5.13 Amplitudes of the first ten echoes for different pairs of excitation and refocusing pulses. Solid lines show results obtained by simulation while red crosses show experimental results. Data were taken with permission from the co authors in Ref. [3]. 112

List of Tables

5.1 SNR of the standard refocusing pulse and SPA pulses with a perfect 90° excitation pulse. The SNR is normalized with respect to the SNR for the hard 180° pulse with a perfect 90° excitation pulse. We assume nominal rf amplitude for all these calculations. The acquisition window is $t_p + 6t_{180}$, where t_p is the pulse length. 96

5.2 The table shows the SNR obtained by using different pairs of excitation and refocusing pulses. All SNRs are normalized with respect to the SNR obtained by using the standard excitation and refocusing pulse. The perfect 90° brings all magnetization to the y axis. The perfect $AMEX$ brings all magnetization to the corresponding axes of the refocusing cycle. 103

Citations to Previously Published Work

Chapter 3 is based on

"Homonuclear decoupling for liquid-state NMR," Van D. M. Koroleva and Navin Khaneja, J. Chem. Phys. **137**, 094103 (2012).

Chapter 5 is based on

"Broadband CPMG sequence with short composite refocusing pulses," Van D. M. Koroleva, Soumyajit Mandal, Yi-Qiao Song, and Martin D. Hürlimann, J. Mag. Reson **230**, 64 (2013).

"Axis-matching excitation pulses for CPMG-like sequences in inhomogeneous field," Soumyajit Mandal, Van D. M. Koroleva, Troy W. Borneman, Yi-Qiao Song, Martin D. Hürlimann, to appear in J. Mag. Reson.

Acknowledgments

First of all, I would like to express my special thanks to Prof. Navin Khaneja for his scientific advice and support during my Ph.D study. I would like to thank my other thesis committee members Prof. Vahid Tarokh, Prof. Roger Brockett, and Prof. Gerhard Wagner for guidance, advice and encouragement.

While the work on homonuclear decoupling was done closely with Prof. Navin Khaneja, other collaborations have helped enrich my experience and broaden my knowledge. I am thankful to Prof. Haidong Yuan for introducing and working with me on the problem of reducing decoherence in quantum information processing. The work on the CPMG sequence started when I was an intern at Schlumberger-Doll Research. I am indebted to Dr. Martin Hürlimann, Dr. Soumyajit Mandal, Dr. Troy Borneman, and Dr. Yi-Qiao Song for fruitful collaborations and discussions.

I would also like to thank my current and former lab mates Jamin Sheriff, Paul Coote, Philip Owrutsky, and James Lin for being always helpful and supportive. And last but not least, a big thank you to my family and all the wonderful friends with whom I can share the challenges and the joy of life.

This page is left intentionally blank

Chapter 1

Introduction

Nuclear Magnetic Resonance (NMR) was first predicted and observed by Rabi using molecular beams [4] in 1937 followed by Bloch [5] and Purcell [6] in 1946 who observed the phenomenon in bulk materials. NMR is a physical phenomenon in which nuclei absorb or emit electromagnetic radiation when irradiated by an electromagnetic field, usually in the range of radio frequency, whose frequency matches that of the difference between energy levels in the nuclei. Not only is NMR a beautiful physical phenomenon, it also finds far reaching applications in other areas of science, medicine, and engineering. In chemistry, NMR spectroscopy is an indispensable tool to study the three dimensional structures of macromolecules at atomic precision [7]. In medicine, Magnetic Resonance Imaging (MRI) is a state-of-the art technology to scan images of various parts of the human body [8] for clinical use. Outside the laboratory, NMR is a powerful tool used to characterize fluid properties in earth formations deep underground [9, 10]. Recently, NMR has also been used as a testbed for quantum computing [11, 12] and techniques well developed in traditional NMR

are also used in quantum information processing (QIP) performed in other solid state systems.

Together with mass and electric charge, *spin* is an intrinsic property of an atomic nucleus. It can be thought of as a source of nuclear magnetism, which, even though much weaker than the magnetism generated by an electric current, is of fundamental importance. Nuclei with an odd mass number or with an even mass number and an odd atomic number have nonzero spins. Those in the first category have half-integral spin quantum numbers, which are called fermions, while those in the second category have integral spin quantum numbers called bosons. Some of the most important nuclei in NMR spectroscopy of biomolecules are ${}^{1}H$,${}^{13}C$ and ${}^{15}N$.

The nuclear spin angular momentum is a vector quantity denoted $\mathbf{I}$ whose magnitude is

$$|\mathbf{I}| = \hbar\sqrt{I(I+1)}, \tag{1.1}$$

where I is the nuclear spin angular momentum quantum number. As a kind of angular momentum, only one component of $\mathbf{I}$ can be specified with certainty, the other two are now known due to the uncertainty principle. The specified component is often chosen to be the z component:

$$I_z = \hbar m \tag{1.2}$$

Here m is the spin quantum number that takes on values $m = (-I, -I+1, \ldots, I)$. For example, for spins with $I = \frac{1}{2}$, m can only be equal to $\pm\frac{1}{2}$.

Spin and magnetism of a nucleus are closely related. In particular, the spin angular momentum is related to the nuclear magnetic moment, $\boldsymbol{\mu}$ through the equation

$$\boldsymbol{\mu} = \gamma \boldsymbol{I}, \tag{1.3}$$

in which γ is the gyromagnetic ratio that is characteristic for a given nucleus. In the presence of an external magnetic field $\boldsymbol{B}$, the spin states of the nucleus have energies

$$\boldsymbol{E} = -\boldsymbol{\mu} \cdot \boldsymbol{B} \tag{1.4}$$

In a typical NMR experiment, the applied static magnetic field $\boldsymbol{B}$ points in the z direction having magnitude B_o. Since $\boldsymbol{\mu}$ is quantized just like $\mathbf{I}$, the energy levels are also quantized according to

$$E_m = -m\hbar\gamma B_o, \tag{1.5}$$

that is we have $2I + 1$ equally spaced energy levels called *nuclear Zeeman levels*.

Transitions between energy levels are effected via an electromagnetic radiation, often in the radio frequency (rf.) range. For a magnetic dipole transition, the selection rule is $\Delta m = \pm 1$. Therefore, the required energy to drive a transition from one spin state to another is

$$\Delta E = -\hbar\gamma B_o. \tag{1.6}$$

The quantity $\omega_o = \frac{E}{\hbar} = -\gamma B_o$ is the *resonance frequency* of the nuclear spin. It is called the *Larmor frequency*.

Nuclear spins give rise to nuclear magnetism that interacts with other magnetic fields. This provides us with a very useful and powerful tool to study the structure and many dynamical processes at the atomic level. The starting point of most NMR experiments is the creation of a *thermal equilibrium* state. In general, the *spin polarization axis*, which is the direction of $\mathbf{I}$ can point in any direction. This direction is parallel to the direction of the magnetic moment as seen in Eq. 1.3. Consider a sample in the absence of an external magnetic field. The distribution of magnetic

moments is isotropic leading to a zero total magnetization. When a large external magnetic field B_o is applied to the sample, individual spins start to precess around this external field at the Larmor frequency while keeping the angle between the field and the spin magnetic moment constant. Over a long enough period of time, due to local fluctuations of the magnetic field, the net distribution of spin orientations will be more probable in the direction of the external magnetic field. This is call the thermal equilibrium state. Consider specifically the case of spin-$\frac{1}{2}$. As stated earlier, the spin states denoted as $|\uparrow\rangle$ and $|\downarrow\rangle$ have angular momentum quantized in the z direction corresponding to $m = \pm\frac{1}{2}$. Therefore they occupy two energy levels $E_{1,2} = \mp\frac{1}{2}\hbar\gamma B_o$. In thermal equilibrium, the ratio of populations between spins in these two states is given by the Maxwell-Boltzmann distribution:

$$\begin{aligned} \frac{N_u}{N_d} &= \exp(-\frac{\Delta E}{k_B T}) \\ &= \exp(-\frac{\hbar\gamma B_o}{k_B T}), \end{aligned} \tag{1.7}$$

where the Boltzmann constant $k_B = 1.38 \times 10^{-23} JK^{-1}$, $\hbar = 1.05457173 \times 10^{-34} Js$. At room temperature $T = 300K$. The gyromagnetic ratio for protons is $\gamma = 2.6752 \times 10^8 (Ts)^{-1}$. At $B_o = 11.7\ T$, the population difference is only 4.3 per 10^5. This insensitivity nature of NMR is a challenge that can be overcome by two reasons. First, we usually work with a very large number of spins and second, resonance is the key to pick up the signal in the receiver coil. Nevertheless, Eq. 1.7 explains the impetus to increase sensitivity in high resolution NMR spectroscopy by creating ever more powerful magnets.

After the spins have reached the equilibrium state, radio frequency (rf.) pulses are then used to bring the spins to the transverse plane and manipulate their dynamics.

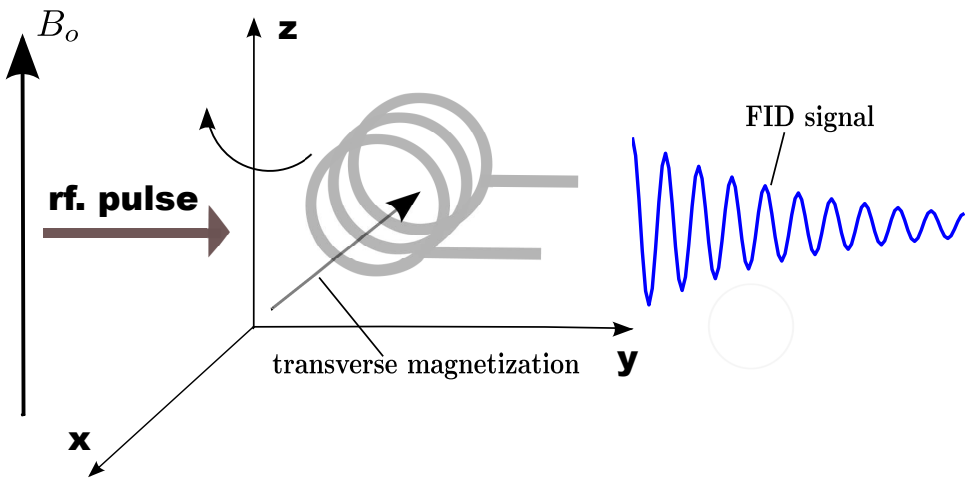

Figure 1.1: The basic components of an NMR experiment

When the radio frequencies are turned off, the spins still precess around the B_o field at the Larmor frequency. If we place a coil near the sample, the changing magnetization will induce an electric current in the coil according to Faraday's law. The voltage measured in the coil is called the *free induction decay* (FID) signal. Figure. 1 shows the basic components of an NMR experiment.

While the B_o field is usually static during the course of the experiment, the rf. pulses, on the other hand, are time varying that reflect the level of control we have on the system. They come in all lengths and shapes ranging from simple, constant phase and amplitude pulses to complex phase- and amplitude-modulated pulses. With proper designs, we can use these pulses to control the spin dynamics in order to obtain useful structural and dynamical information such as chemical shifts, relaxation times, suppress unwanted effects such as coupling in high resolution NMR spectroscopy, or enhance effects such as polarization transfer [13]. In this thesis, we propose and analyze the performance of several rf. pulses with applications in high resolution

NMR spectroscopy, quantum computing and the study of earth formations.

It is fair to say that NMR spectroscopy has been the biggest driving force for the development of NMR techniques. Although there are a formidable literature in high resolution NMR spectroscopy, there are still many challenging problems, among which is the problem of homonuclear decoupling. Chapter 3 presents a solution to the problem of homonuclear decoupling in liquid-state NMR. We propose a new pulse sequence that effectively decouples a two-spin half system that has weak *isotropic* scalar coupling.

In quantum computing, liquid-state NMR is mainly used as test beds for quantum algorithms [12]. Current research is moving towards solid-state systems for their scalability potential compared to liquid-state NMR. Examples are nitrogen-vacancy (NV) color centers in diamond, phosphorous donors in silicon and quantum dots to realize quantum computers. Nevertheless, techniques developed in NMR have found very useful applications in the manipulation of electron spins in these solid-state systems. For instance, spin echo sequences that were first developed in NMR are routinely used to decouple the coupling between the electron spin of the NV center in a diamond lattice and the nuclear spins of ^{13}C present in the lattice [14, 15, 16]. In chapter 4, we extended the use of the sequence in chapter 3 to reduce decoherence in quantum registers. We will show that this pulse sequence is capable of decoupling the Ising interaction between the spins as well the coupling between the spins and the environment. This is important in maintaining the coherence of the spin system, a big challenge in the implementation of quantum computer.

Moving away from the traditional laboratory settings where the sample is placed

inside a huge magnet, in the so call single-sided NMR [17] the object to be studied is placed to one side of the magnet. This configuration offers new challenges as well as convenience and promises for many important applications of NMR. Recently, portable NMRs are commercially available for use in biology, medicine, and for studying cultural heritages such as paintings [17]. Still, the earliest and probably the most important application of single-sided NMR is the study of earth formations in, for example, the exploration of oil and gas reservoirs. Of particular importance in these applications is the Carr-Purcell-Meiboom-Gill sequence that generates spin echoes. Chapter 5 deals with the design of new refocusing and excitation pulses for this sequence. The new pulses have the potential to triple the signal to noise ratio in highly inhomogeneous field. Experimental results confirm the effectiveness of the new pulse sequences.

A detailed description of each problem will be given in the corresponding chapter. We will begin in chapter 2 by reviewing relevant NMR concepts and mathematical methods that are helpful in understanding the spin dynamics and the pulse sequences in subsequent chapters.

Chapter 2

Review of NMR concepts and mathematical methods

2.1 Representation of spins in quantum mechanics

The evolution of the wave function or the state of a quantum system is described by the Schroëdinger equation

$$i\hbar\frac{d}{dt}|\psi(t)\rangle = H(t)|\psi(t)\rangle, \tag{2.1}$$

where $|\psi(t)\rangle$ is the state and $H(t)$ is the Hamiltonian of the system. The Hamiltonian in matrix form is a Hermitian matrix, i.e. $H(t) = H(t)^\dagger$. In NMR, the Hamiltonian can be considered to be the nuclear spin Hamiltonian only. This assumption is justified by the fact that for most practical purposes, the motion of the electrons are so rapid that the nuclear spins only see the average effect of the electrons. The nuclear spin Hamiltonian contains the interaction between the nuclear spins with the time

average effect of the fields generated by the electrons as well as the externally applied fields.

In order to solve the spin dynamics, we need to describe the spin states, the Hamiltonians, as well as the observables for measurement.

2.1.1 Spin-$\frac{1}{2}$ operators

We limit the discussion to spin-$\frac{1}{2}$, which serves our purposes since we will mainly work with spin-$\frac{1}{2}$ particles including ^1H, ^{13}C, and ^{15}N. A set of convenient matrices to describe these spins is Pauli matrices

$$\sigma_x = \begin{pmatrix} 0 & 1 \\ 1 & 0 \end{pmatrix}, \sigma_y = \begin{pmatrix} 0 & -i \\ i & 0 \end{pmatrix}, \sigma_z = \begin{pmatrix} 1 & 0 \\ 0 & -1 \end{pmatrix}. \tag{2.2}$$

$I_x = \frac{1}{2}\sigma_x$, $I_y = \frac{1}{2}\sigma_y$, and $I_z = \frac{1}{2}\sigma_z$ are the spin-$\frac{1}{2}$ operators. $\{iI_x, iI_y, iI_z\}$ form a basis for $\mathfrak{su}(2)$, the 2×2 skew-Hermitian traceless matrices.

Some formulas involved the spin operators and the Pauli matrices that can be easily verified are:

$$[I_x, I_y] = iI_z, \quad [I_y, I_z] = iI_x, \quad [I_z, I_x] = iI_y, \tag{2.3}$$

$$e^{-i\theta\hat{n}\cdot\boldsymbol{\sigma}} = \cos(\theta)\mathbf{1} + i\sin(\theta)\hat{n}\cdot\boldsymbol{\sigma}. \tag{2.4}$$

$$(\vec{a}\cdot\boldsymbol{\sigma})(\vec{b}\cdot\boldsymbol{\sigma}) = (\vec{a}\cdot\vec{b})\mathbf{1} + i\boldsymbol{\sigma}\cdot(\vec{a}\times\vec{b}), \tag{2.5}$$

where $\mathbf{1}$ is the identity matrix, $\vec{a}$ and $\vec{b}$ are any real value vectors, and $\boldsymbol{\sigma} = [\sigma_x, \sigma_y, \sigma_z]'$.

Using the commutation rules between the spin operators, we have

$$e^{-iI_x\theta} I_y e^{iI_x\theta} = I_y\cos(\theta) + I_z\sin(\theta) \tag{2.6}$$

We call any set of matrices that obeys the same commutation rules of the spin operators an isomorphic copy of the spin operators. If (A, B, C) is such a set, then we also have

$$e^{-A\theta} B e^{A\theta} = B\cos(\theta) + C\sin(\theta). \tag{2.7}$$

Spin up and down are represented by the two eigen states of I_z with eigen values $\frac{1}{2}$ and $-\frac{1}{2}$

$$|\uparrow\rangle = \begin{pmatrix} 1 \\ 0 \end{pmatrix}, \quad |\downarrow\rangle = \begin{pmatrix} 0 \\ 1 \end{pmatrix}.$$

These are called Zeeman basis.

In NMR, however, most of the time we are working with an ensemble of spins. The basis for a system of N coupled spins has the form

$$|\psi\rangle = |s_1\rangle \otimes |s_2\rangle \otimes \cdots |s_N\rangle,$$

where each s_i can be either $|\uparrow\rangle$ or $|\downarrow\rangle$. This results in 2^N bases. In the case of two spins, the Zeeman basis would be

$$\begin{aligned} |\uparrow\uparrow\rangle &= \begin{bmatrix} 1 \\ 0 \end{bmatrix} \otimes \begin{bmatrix} 1 \\ 0 \end{bmatrix} = \begin{bmatrix} 1 \\ 0 \\ 0 \\ 0 \end{bmatrix} \qquad |\uparrow\downarrow\rangle = \begin{bmatrix} 1 \\ 0 \end{bmatrix} \otimes \begin{bmatrix} 0 \\ 1 \end{bmatrix} = \begin{bmatrix} 0 \\ 1 \\ 0 \\ 0 \end{bmatrix} \\ |\downarrow\uparrow\rangle &= \begin{bmatrix} 0 \\ 1 \end{bmatrix} \otimes \begin{bmatrix} 1 \\ 0 \end{bmatrix} = \begin{bmatrix} 0 \\ 0 \\ 1 \\ 0 \end{bmatrix} \qquad |\downarrow\downarrow\rangle = \begin{bmatrix} 0 \\ 1 \end{bmatrix} \otimes \begin{bmatrix} 0 \\ 1 \end{bmatrix} = \begin{bmatrix} 0 \\ 0 \\ 0 \\ 1 \end{bmatrix} \end{aligned} \tag{2.8}$$

The algebra that describes an N spin system is therefore $\mathfrak{su}(2^N)$. A commonly used basis for the $\mathfrak{su}(2^N)$ algebra is $\{iB_s\}$ [18, 13] where

$$B_s = 2^{(q-1)}\Pi_{k=1}^{N}(I_{k,\alpha})^{a_{ks}}, \tag{2.9}$$

where q is the number of operators in the product, $a_{ks} = 1$ for q of the spins, and $a_{ks} = 0$ for the remaining $N - q$ spins, and

$$I_{k,\alpha} = \mathbf{1} \otimes \mathbf{1} \cdots \otimes I_\alpha \cdots \otimes \mathbf{1},$$

I_α appears at the k^{th} position in the product. For example, the basis operators for a 2 spin-$\frac{1}{2}$ system are

$$\begin{aligned} q = 1 \quad & I_{1x}, I_{1y}, I_{1z}, I_{2x}, I_{2y}, I_{2z}, \\ q = 2 \quad & 2I_{1x}I_{2x}, 2I_{1x}I_{2y}, 2I_{1x}I_{2z}, \\ & 2I_{1y}I_{2x}, 2I_{1y}I_{2y}, 2I_{1y}I_{2z}, \\ & 2I_{1x}I_{2x}, 2I_{1x}I_{2y}, 2I_{1x}I_{2z}. \end{aligned}$$

Operators that involve more than one spin are referred to as product operators.

2.1.2 Measurement and density matrix

A physically observable quantity is represented in quantum mechanics by a Hermitian operator A that has a complete set of orthonormal eigen functions. The wave function can be decomposed in terms of these eigen functions

$$|\psi\rangle = \sum_n c_n |n\rangle. \tag{2.10}$$

Upon measurement of A, the wave function appears to be in one of these functions or eigenstates, a phenomenon called the collapse of the wave function. The probability of collapsing into eigen state $|n\rangle$ is $p_n = c_n c_n^*$. The value of the measurement

is the corresponding eigenvalue of A, λ_n. Since $A|n\rangle = \lambda_n|n\rangle$, we can denote the measurement as the expectation value of A in the eigen state $|n\rangle$

$$\langle A\rangle = \langle n|A|n\rangle = \lambda_n \tag{2.11}$$

A quantum system that can be described by a wave function that obeys the Schröedinger equation is said to be in a *pure state*. The wave function contains all the information about the system. However, when the system is part of a larger system about which we do not have a complete knowledge, the system is no longer represented by a wave function. It is said to be in a *mixed state*.

The mixed state can be described by an ensemble of wave function $|\psi_j\rangle$ with probability p_j. The statistical value of the expectation value of an observable A is then

$$\langle A\rangle = \sum_j p_j \langle \psi_j|A|\psi_j\rangle \tag{2.12}$$

If we represent a wave function using a set of orthonormal basis $|n\rangle$, which are not necessarily the eigen functions of A, then we can further write $\langle A\rangle$ as

$$\begin{aligned} \langle A\rangle &= \sum_{m,n}\sum_j p_j c^*_{mj}\langle m|A|n\rangle c_{nj} \\ &= \sum_{m,n} \overline{c_n c^*_m}\langle m|A|n\rangle \end{aligned} \tag{2.13}$$

While $\langle m|A|n\rangle$ stays the same, the quantity $\overline{c_n c^*_m}$ depends on the system. It is called the statistical ensemble average of the system. The matrix formed by $\overline{c_n c^*_m}$ in the orthonormal basis $|n\rangle$ is called the *density matrix* denoted ρ_{mn} that describes the mixed state. It plays the role of the wave function when the system is in a pure state.

Equation 2.13 can be recast in the more commonly used form

$$\begin{aligned}\langle A\rangle &= tr(|n\rangle \sum_{m,n} \overline{c_n c_m^*}\langle m|A) \\ &= tr(\rho A).\end{aligned} \tag{2.14}$$

For example, let $\mathbf{M}$ denote the sum of individual nuclear magnetic moments. The expectation of M_x, which is $tr(M_x\rho)$ is the bulk magnetization that we observe in the x direction.

In NMR, we usually work with a very large number of spins, on the order of 10^{22} so the density matrix is a natural way to describe the system. Once we know the density matrix at a given time, we will know the density matrix at any other time after that because the evolution of the density matrix follows the Liouville equation

$$i\hbar\frac{d\rho}{dt} = [H, \rho]. \tag{2.15}$$

The question is how do we determine the density matrix at the initial time. As the rule of thumb, the starting point is always the thermal equilibrium state. If we leave the system alone for a long enough amount of time, it will come to the thermal equilibrium state. The density matrix for an isolated spin in thermal equilibrium derived from the Boltzmann distribution is

$$\rho_{eq} = \frac{1}{2}\mathbf{1} + \frac{1}{2}\mathcal{B}I_z, \tag{2.16}$$

where $\mathcal{B}$ denotes the Boltzmann factor

$$\mathcal{B} = \frac{\hbar\gamma B_o}{k_B T} \tag{2.17}$$

It should be noted that although the density matrix is a rigorous and general description of a quantum system, in NMR it is often convenient to use the product operators as introduced in Sec. 2.1.1.

2.1.3 The spin Hamiltonian

The nuclear spin Hamiltonian describes the interaction between the nuclear magnetic moment and nuclear electric charges with the surrounding fields. We will distinguish between external and internal spin Hamiltonian.

The external spin Hamiltonian comes from the interaction of the nuclear magnetic moment with the the applied magnetic fields. Below, we list the form of the Hamiltonian for a single spin. Generalization to multiple spins is straightforward. The static magnetic field in the z direction gives rise to the Larmor Hamiltonian

$$H_{Larmor} = -\gamma I_z B_o = \omega_o I_z. \tag{2.18}$$

Usually B_o is very homogeneous but there are applications, such as in MRI, in which it has a gradient along a particular direction.

The rf. pulses create the rf. Hamiltonian

$$H_{rf} = u(t)I_x + v(t)I_y, \tag{2.19}$$

where the transverse components of the rf. field are

$$\begin{aligned} u(t) =& \omega_1 \cos(\omega_{rf} t + \phi) \\ v(t) =& \omega_1 \sin(\omega_{rf} t + \phi). \end{aligned} \tag{2.20}$$

For spins-$\frac{1}{2}$, internal spin interactions are purely magnetic. The internal spin Hamiltonian captures the interactions between the nuclear magnetic moment with the surrounding electrons and other nuclear spins. They include chemical shift, direct dipole-dipole coupling, J coupling, and spin-rotation interaction. Chemical shift will be discussed in Sec. 2.2. J coupling and dipole-dipole coupling will be discussed

in Sec. 3.1. We will omit spin-rotation interaction because it is small for most applications in NMR. Even though dipole-dipole coupling is averaged to zero in liquids, it is not zero at any given point and is responsible for the spin-spin relaxation, which is discussed in Sec. 2.4.

2.2 Chemical shift

When an external magnetic field is applied to a sample, the electrons, which also have a magnetic moment many times bigger than that of the nuclei, create an induced magnetic field around them. Each nucleus feels a magnetic field which is the sum of the external field and the induced field. Since the electron distributions vary, nuclei at different sites of the same molecule experience a slightly different magnetic field. This effect is called the *chemical shift*.

The local magnetic field can be represented by

$$\boldsymbol{B}_{loc} = \boldsymbol{B}_{ext} + \boldsymbol{B}_{ind}. \tag{2.21}$$

To a very good approximation, in general

$$\boldsymbol{B}_{ind} = \boldsymbol{\delta} \cdot \boldsymbol{B}_{ext} \tag{2.22}$$

where δ is called the chemical shift tensor, a 3×3 real matrix.

In isotropic liquids, where the molecules are free to tumble around equally in all directions, the observed chemical shift can be simply defined as

$$\omega_o^{'} = -\gamma B_o(1 + \delta) \tag{2.23}$$

where as usual, γ is the gyromagnetic ratio of the nucleus, B_o is the static field and δ depends on the local chemical environment. δ is defined using a reference frequency ω_{ref}

$$\delta = \frac{\omega_o^{'} - \omega_{ref}}{\omega_o} \tag{2.24}$$

where ω_o is the operating frequency of a spectrometer, which, for example is $500MHz$ for proton at 11.7 T. δ is often referred to as the chemical shift. Its value is so small that it is usually measured in part-per-million (ppm).

2.3 Bloch equation

A single spin-$\frac{1}{2}$ has a well defined spin angular momentum $\mathbf{I}$ that precesses around a magnetic field like a spinning top. For an ensemble of non-interacting spins, the *magnetization vector* $\mathbf{M}$, the sum of individual nuclear magnetic moments, also behaves in the same way. Instead of using the density matrix formalism, in this case, we can use the Bloch equation to describe the evolution of $\mathbf{M}(t)$

$$\frac{d}{dt}\begin{bmatrix} M_x \\ M_y \\ M_z \end{bmatrix} = -\gamma \boldsymbol{B}(t) \times \boldsymbol{M}(t) = \begin{bmatrix} 0 & -\omega_o & -\gamma B_y(t) \\ \omega_o & 0 & +\gamma B_x(t) \\ \gamma B_y(t) & -\gamma B_x(t) & 0 \end{bmatrix} \begin{bmatrix} M_x \\ M_y \\ M_z \end{bmatrix} \tag{2.25}$$

or equivalently

$$\frac{d}{dt}\begin{bmatrix} M_x \\ M_y \\ M_z \end{bmatrix} = \begin{bmatrix} 0 & -\omega_o & v(t) \\ \omega_o & 0 & -u(t) \\ -v(t) & u(t) & 0 \end{bmatrix} \begin{bmatrix} M_x \\ M_y \\ M_z \end{bmatrix} \tag{2.26}$$

We can also cast the above vector equation in the form

$$\frac{d}{dt}\mathbf{M}(t) = (\omega_o\Omega_z + u(t)\Omega_x + v(t)\Omega_y)\mathbf{M}(t), \tag{2.27}$$

where $\Omega_{x,y,z}$ form $SO(3)$ and are given explicitly as

$$\Omega_x = \begin{bmatrix} 0 & 0 & 0 \\ 0 & 0 & -1 \\ 0 & 1 & 0 \end{bmatrix} \quad \Omega_y = \begin{bmatrix} 0 & 0 & 1 \\ 0 & 0 & 0 \\ -1 & 0 & 0 \end{bmatrix} \quad \Omega_z = \begin{bmatrix} 0 & -1 & 0 \\ 1 & 0 & 0 \\ 0 & 0 & 0 \end{bmatrix} \tag{2.28}$$

Since $\Omega_{x,y,z}$ are skew-symmetric matrices, the norm of $\mathbf{M}(t)$ is preserved. The three components of the magnetization are said to evolve on the Bloch sphere.

A rotation around x by an angle α counter clockwise has rotation matrix

$$R_x(\theta) = \exp(\Omega_x\theta) = \begin{bmatrix} 1 & 0 & 0 \\ 0 & \cos\alpha & -\sin\alpha \\ 0 & \sin\alpha & \cos\alpha \end{bmatrix} \tag{2.29}$$

Similar expressions for rotations around the y and z axis apply. Using the commutation rules

$$\exp(\Omega_x\alpha)\exp(\Omega_y\theta)\exp(-\Omega_x\alpha) = \exp(\Omega_y\theta\cos\alpha + \Omega_z\theta\sin\alpha) \tag{2.30}$$

and similarly for the cyclic permutation of $\{\Omega_x, \Omega_y, \Omega_z\}$ we see that any rotations can be written in the form

$$R_z(\alpha)R_y(\beta)R_z(\gamma)R_y(-\beta)R_z(-\alpha). \tag{2.31}$$

The Bloch equation is often regarded as a semiclassical description of spins because it describes the evolution of the bulk magnetization in the language of classical

physics, which is very useful for many applications, but the description is only valid for a system of non-interacting spins. When we have to take into account, for example, the coupling between spins, a full quantum mechanics description of spins is needed.

2.4 Relaxation

Spins interact with each other and with the lattice. This leads to relaxation. There are two basic relaxation mechanisms: the *spin-lattice relaxation* and the *spin-spin relaxation*. The spin-lattice relaxation involves the exchange of energy between the spins and the surrounding, thereby bringing the the spin populations back to the Boltzman distribution. It is also called longitudinal relaxation. The spin-spin relaxation is due to the interaction between the spins that lead to the lost of coherences, i.e. relative phases between them.

For an ensemble of non-interacting spin-$\frac{1}{2}$, there is a single constant associated with the spin-lattice relaxation called T_1. It is the time over which the z-magnetization looses or gains e times its initial magnetization. Similarly, there is a single constant associated with the spin-spin relaxation called T_2.

When taking relaxations into account, the Bloch equation is modified according to

$$\begin{aligned}
\frac{dM_x(t)}{dt} &= (\mathbf{M}(t) \times \mathbf{B}(t))_x - \frac{M_x(t)}{T_2} \\
\frac{dM_y(t)}{dt} &= (\mathbf{M}(t) \times \mathbf{B}(t))_y - \frac{M_y(t)}{T_2} \\
\frac{dM_z(t)}{dt} &= (\mathbf{M}(t) \times \mathbf{B}(t))_z - \frac{M_z(t) - M_0}{T_1}
\end{aligned} \tag{2.32}$$

2.5 Average Hamiltonian

The average Hamiltonian is a method commonly used in NMR to approximate a time varying Hamiltonian over a certain period of time by a supposedly simpler Hamiltonian that has the same effect over the same period of time. It is a simple yet powerful method that is often deployed in the design of numerous pulse sequences in NMR. Let us first look at the context where such usage is needed.

In NMR, the total Hamiltonian of a system often comprises of three terms

$$H(t) = H_o + H_{int} + H_{rf}, \tag{2.33}$$

H_o is the Zeeman Hamiltonian that reflects the effect of the static magnetic field B_o. H_{int} describes the interaction between different constituents of the system such as coupling. While H_o and H_{int} are stationary, the third term H_{rf} is usually time varying. It represents the rf. pulses, the control that we have on the system.

The evolution of a density matrix ρ under the Hamiltonian H is described by the Liouville equation

$$i\hbar\frac{d\rho}{dt} = [H, \rho].$$

Consider the interaction frame of the time invariant Hamiltonian H_o whose unitary propagator is $U_o = e^{-iH_o t}$. This frame is called the rotating frame indicating the fact that we are making observations in a frame that is rotating at an appropriate frequency with respect to the lab frame. We make the following transformation to the density matrix $\tilde{\rho} = U_o^\dagger \rho U_o$ and hope to find a new Hamiltonian $\tilde{H}$ that governs the evolution of $\tilde{\rho}$ according to

$$i\hbar\frac{d\tilde{\rho}}{dt} = [\tilde{H}, \tilde{\rho}], \tag{2.34}$$

It is easy to show that $\tilde{H} = U_o^\dagger(H_{int} + H_{rf})U_o$, i.e. the Hamiltonian is transformed to the interaction frame in a similar manner as that of the density matrix.

In the same way, we can also choose to observe the system in the interaction frame of the rf. Hamiltonian, called the *toggling frame*. In some situations, successive transformations to several frames are needed. From now on, we will assume that the internal Hamiltonians are time independent and denote the total Hamiltonian of the system as $H_s = H_o + H_{int}$. Often the rf. Hamiltonian is not time independent so the corresponding unitary operator U_{rf} does not have a simple exponential form as U_o. It is the solution of the Schroëdinger equation

$$i\hbar\frac{dU_{rf}}{dt} = H_{rf}(t)U_{rf}, \tag{2.35}$$

with the initial condition $U_{rf}(0) = \boldsymbol{I}$. The complication in calculating U_{rf} arises due to the fact that $[H_{rf}(t), H_{rf}(s)]$ is not equal to zero for all values of t and s. Let us denote $U_{rf}(t_1, t_2)$ as the propagator from time t_1 to time t_2.

In quantum mechanics, the solution to Eq. 2.35 is denoted as

$$U_{rf}(t_1, t_2) = T\exp\left(\int_{t_1}^{t_2} -iH_{rf}(t')dt'\right), \tag{2.36}$$

where T indicates the Dyson time-ordering operation. This means

$$T\{H(t_1)H(t_2)\} = \begin{cases} H(t_1)H(t_2) & \text{for} \quad t_1 > t_2 \\ H(t_2)H(t_1) & \text{for} \quad t_2 > t_1. \end{cases} \tag{2.37}$$

In control theory, the solution is given by the *Peano-Baker series* [19]

$$U_{rf}(t_1, t_2) = \boldsymbol{I} - i\int_{t_1}^{t_2} H_{rf}(\sigma_1)d\sigma_1 + (-i)^2\int_{t_1}^{t_2} H_{rf}(\sigma_1)\int_{t_1}^{\sigma_1} H_{rf}(\sigma_2)d\sigma_2 d\sigma_1 + \ldots \tag{2.38}$$

A more detailed mathematical treatment is given in Ref. [20].

Using the interaction frame picture, we can rewrite the unitary propagator $U(t)$ of the Hamiltonian $H(t) = H_s + H_{rf}(t)$ as

$$U(t) = U_{rf}(t)\tilde{U}_s(t), \tag{2.39}$$

where $\tilde{U}_s(t)$ is the propagator corresponding to

$$\tilde{H}_s(t) = U_{rf}(t)^\dagger H_s U_{rf}(t). \tag{2.40}$$

The average Hamiltonian is developed with the following assumptions which are often satisfied in NMR

- The rf. Hamiltonian is *periodic* with period T. $H_{rf}(t) = H_{rf}(t + nT)$ for $n = 0, 1, 2, \ldots$.
- The rf. Hamiltonian is *cyclic*, i.e. $U_{rf}(T) = \boldsymbol{I}$. This means over one full cycle, the rf. has no effect on the system.

From the periodicity of H_{rf} we can see from Eq. 2.40 that $\tilde{H}_s(t)$ is also periodic with period T. And using the cyclicity condition, from Eq. 2.39, we see that

$$U(T) = \tilde{U}_s(T). \tag{2.41}$$

In addition,

$$U(nT) = \tilde{U}_s(T)^n. \tag{2.42}$$

These results mean that for *stroboscopic observation* in synchronism with the periodic rf. pulses, the evolution can be described by the periodic propagator $\bar{U}_s(T)$ which corresponds to the Hamiltonian of the system in the interaction frame. This

Hamiltonian $\bar{H}_s(T)$ is called the average Hamiltonian and it is given in terms of the Magnus expansion

$$\bar{H}_s(T) = \bar{H}_s^{(0)} + \bar{H}_s^{(1)} + \bar{H}_s^{(2)} + \ldots, \tag{2.43}$$

with

$$\begin{aligned}
\bar{H}_s^{(0)} &= \frac{1}{T}\int_0^T dt\tilde{H}_s(t), \\
\bar{H}_s^{(1)} &= \frac{-i}{2T}\int_0^T dt \int_0^t dt'[\tilde{H}_s(t), \tilde{H}_s(t')], \\
\bar{H}_s^{(2)} &= \frac{-1}{6T}\int_0^T dt \int_0^t dt' \int_0^{t'} dt''\{[\tilde{H}_s(t), [\tilde{H}_s(t'), \tilde{H}_s(t'']] + [[\tilde{H}_s(t), \tilde{H}_s(t')], \tilde{H}_s(t'')].\}
\end{aligned} \tag{2.44}$$

If we wish to eliminate some unwanted terms in the system Hamiltonian, the rf. pulses should be designed such that these terms vanish in the toggling frame. For example, in the zero-order term, their time averages should be zero. The higher order terms involve the commutators, that is the interaction, between different parts of the Hamiltonian.

Note that the cyclic condition is not a requirement in using this approach. However, when this condition is not met, the average Hamiltonian depends on $U_{rf}(T)$ making the solution susceptible to fluctuations of the rf. pulses.

If the condition $T|\tilde{H}_s| << 1$ is met, the Magnus expansion converges fast and we can use the average Hamiltonian to study the system for an extended period of time, i.e. many times longer than T.

Chapter 3

Homonuclear decoupling in liquid-state NMR

3.1 Overview of coupling

Coupled spin systems are ubiquitous in NMR [13, 21]. In NMR, the coupling between spins causes multiplets in the spectrum of the Free Induction Decay (FID) signal [21]. These multiplets degrade the signal to noise ratio and complicate the interpretation of the data. For example, to determine the structure of a large protein, it is desirable that these multiplets be collapsed into singlets in order to increase the intensity of the peaks.

There are two types of coupling: *dipolar* coupling and *scalar* coupling [11]. The first one is mediated through space while the latter is mediated through chemical bonds. Dipolar decouling is due to the interaction of a spin to the dipolar field produced by another spin. The energy associated with the classical interaction between

two magnetic dipoles $\boldsymbol{\mu}_1$ and $\boldsymbol{\mu}_2$ is

$$E = \frac{\mu_o}{4\pi}\left(\frac{\boldsymbol{\mu}_1 \cdot \boldsymbol{\mu}_2}{r^3} - \frac{3(\boldsymbol{\mu}_1 \cdot \boldsymbol{r})(\boldsymbol{\mu}_2 \cdot \boldsymbol{r})}{r^5}\right) \tag{3.1}$$

where $\boldsymbol{r}$ is the vector joining the magnetic dipoles and $\mu = 4\pi 10^{-7}$ Tm/A is the permeability of free space.

For two nuclear spins $I^{(1)}$ and $I^{(2)}$, the dipolar Hamiltonian is

$$H_d = \frac{\mu_o}{4\pi}\frac{\gamma_1\gamma_2\hbar^2}{r^3}(1 - 3\cos^2\theta)(2I_z^{(1)}I_z^{(2)} - I_x^{(1)}I_x^{(2)} - I_y^{(1)}I_y^{(2)}), \tag{3.2}$$

where θ, the polar angle in the spherical coordinates, is the angle between the internuclear vector $\boldsymbol{r}$ and the external magnetic field.

Dipolar coupling can be intermolecular or intramolecular because it is mediated through space without the help of the electrons. For this reason, it is also called direct coupling. Since dipolar coupling depends on the distance between the nuclei, measuring its value between pairs of nuclei provides direct information on the geometrical structure of the molecules.

In isotropic liquid-state NMR, where spins are free to tumble around in all directions, the average value of $\cos^2\theta$ when integrated over a solid angle is

$$\overline{\cos^2\theta} = \frac{1}{4\pi}\int_0^{2\pi} d\phi \int_0^{\pi} \cos^2\theta \sin\theta d\theta = \frac{1}{3} \tag{3.3}$$

Therefore, to first order, dipolar coupling is zero. This is of course only valid upon the condition that the rotational motion must be faster than the coupling frequency. This condition is usually satisfied in practice. For example, the frequency associated with the dipolar coupling for the amide group in protein using the gyromagnetic ratio

of ^1H and ^{15}N is [22],

$$\begin{aligned}\Delta\omega &= \frac{\mu_o}{4\pi}\frac{\hbar\gamma_1\gamma_2}{r^3}(3\cos^2\theta - 1)|_{\theta=0} \\ &= \frac{4\pi 10^{-7}}{4\pi}\frac{(1.054\times10^{-34})(2.67\times10^{8})(-2.71\times10^{7})}{(1.08\times10^{-10})^3}(3\cos^3 0 - 1) \\ &= -120\times10^{3}{}_{\text{rad/sec}}\end{aligned} \tag{3.4}$$

This translates into a frequency of 19.3 kHz. The rotation frequencies are on the order of 10^8 Hz. Hence, it is safe to say that dipolar coupling is averaged to zero for isotropically tumbling molecules. As a consequence, in isotropic liquid-state NMR, we are generally concerned with the *scalar* or J coupling.

J coupling is mediated through electrons so it is a purely intramolecular effect. The nuclear spins do not couple together directly but through the interaction with the electrons, hence the alternate name *indirect* spin-spin coupling. The ful form of J coupling between two spins I^1 and I^2 is

$$H_J = \boldsymbol{I}^{(1)} \cdot \boldsymbol{J}_{12} \cdot \boldsymbol{I}^{(2)} \tag{3.5}$$

where $\mathbf{J}_{12}$ is the coupling tensor, a 3×3 matrix. This tensor depends on moleculr orientation and has both isotropic and anisotropic parts.

In anisotropic liquids (liquid crystals) and in solids, the anisotropic part is non zero but it is very small and is hard to distinguish from the dipole-dipole coupling. Hence, in both these cases and especially in isotropic liquids, the J coupling has the form

$$H_J^{isotropic} = J_{12}\boldsymbol{I}^{(1)} \cdot \boldsymbol{I}^{(2)}, \tag{3.6}$$

where $J_{12} = \frac{1}{3}(J_{xx}^{12} + J_{yy}^{12} + J_{yy}^{12})$.

Within J coupling, there are *heteronuclear* and *homonuclear* couplings. In heteronuclear coupling, the coupled spins belong to different nuclear species, and therefore they have very different values for the Larmor frequencies. Let us look the example of carbon ^{13}C and proton ^{1}H. The gyromagnetic ratio of ^{1}H is $\gamma_H = 42.576$ MHz/T and that of ^{13}C is $\gamma_C = 10.705$ MHz/T. Therefore, at applied field $B_o = 11.7$ T, the Larmor frequency of ^{1}H is $\omega_o = \gamma_H B_o \approx 500$ MHz, and the Larmor frequency of ^{13}C is only around 126 MHz. The J coupling, on the other hand, is only on the order of a few hundred Hz. This situation, where the coupling is much smaller than the difference in Larmor frequencies between the two spins

$$J \ll |\Delta\omega| \tag{3.7}$$

qualifies for the high-field, or weak-coupling approximation [23]. Under this approximation, the coupling Hamiltonian is truncated to

$$H_J^{het} = J_{12} I_z^{(1)} I_z^{(2)}. \tag{3.8}$$

Because the Larmor frequencies of the heteronuclear spins are well separated it is possible to selectively irradiate only one species by applying rf. irradiation at the resonance frequency of the targeted spin species. The most common method to decouple heteronuclear spins is to irradiate one spin species with a sufficiently strong field so as to invert the spins fast enough. When one spin is inverted rapidly on a time scale faster than the time scale dictated by the coupling strength between the two spins, and the other spin is not perturbed by the applied field, the interaction between the spins rapidly changes sign and as a result, averages out to zero. This essentially decouples one spin species from the other. Successful methods have been found to initially

decouple proton, whose bandwidth is 10ppm, while observing carbon, whose bandwidth is 200ppm, and later decouple carbon while observing proton. Some common sequences for heteronuclear decoupling are GARP [24], WALTZ-16 [25], WURST [26], adibatic [27], CHIRP [28], and more recently MODE [29]. These were designed using techniques such as composite pulses [30, 31], adiabatic passage, multiple rotating frame and numerical methods.

Decoupling is more challenging when the two coupled spins are homonuclear spins, i.e. they belong to the same species. Their Lamor frequencies are only separated by the chemical shifts. While Larmor frequencies between ^1H and ^{13}C can be on the order of several hundred MHz, the chemical shift difference between protons is only on the order of kHz [7]. This small difference in frequencies makes it difficult to selectively address one spin rapidly without disturbing its neighbors, especially when the precise chemical shifts are unknown and are actually the parameters to be determined. In special cases, where the coupled homonuclear spins lie in distinct frequency bands, band-selective shaped pulses have been used to successfully decouple the spins [32, 33, 34]. Another case is when there are two homonuclear spins whose chemical shifts are close enough to each other but if we know their precise chemical shifts, then we can still selectively invert one by very weak irradiation. However, when the chemical shifts do not organize into distinct frequency bands, or when this information is unavailable, selective irradiation is not an option. Here, assuming almost no knowledge of the chemical shifts, we present new pulse sequences that decouple homonuclear spins without the need for selective inversion over a broad range of frequencies. From the control point of view, this is an interesting problem

because we are only allowed to apply the same control to decouple two different spins. Our immediate goal is to collapse multiplets into singlets in a systematic way in order to determine the locations of the resonances.

The Hamiltonian H of a coupled two spin $\frac{1}{2}$, I and S, in the rotating frame at the rf frequency, usually chosen close to the Larmor frequency of the spin species, is

$$H = \omega_I I_z + \omega_S S_z + J(\boldsymbol{I} \cdot \boldsymbol{S}), \tag{3.9}$$

where ω_I and ω_S are the frequency offsets of the spins. $\boldsymbol{I} \cdot \boldsymbol{S} = I_x S_x + I_y S_y + I_z S_z$. $I_x = \frac{\sigma_x}{2} \otimes \mathbf{1}$, $S_x = \mathbf{1} \otimes \frac{\sigma_x}{2}$, and similarly for y, z.

We first solve the problem of decoupling when the coupling between the homonuclear spins has the Ising form JI_zS_z because the solution is simpler and we can use it to illustrate some basic ideas. We then extend the solution to the problem of isotropic coupling $J(\boldsymbol{I} \cdot \boldsymbol{S})$. The solution for isotropic coupling is divided into two parts: the first part deals with very weak coupling strength compared to the difference in the chemical shifts, and the second part with relatively stronger coupling strength at the cost of nonlinear scaling of the chemical shifts. Finally, we discuss the merits and limitations of our pulse sequences.

3.2 Ising coupling

In this section, we assume coupling of the Ising type, i.e. a Hamiltonian of the form

$$H_{\text{Ising}} = \omega_I I_z + \omega_S S_z + JI_zS_z, \tag{3.10}$$

where $J \ll |\omega_I - \omega_S|$.

In the absence of coupling, $J = 0$, the spectrum of the FID signal $\langle I_x + S_x \rangle$ shows two sharp peaks at frequencies ω_I and ω_S. We normalize the intensity of these peaks to one. In the presence of J, each peak is split into a doublet with half the intensity. This is seen below.

The energy levels and the corresponding eigenstates of H_{Ising} are

$$\begin{aligned} E(|\downarrow\downarrow\rangle) &= \frac{1}{2}(-\omega_I - \omega_S + J/2), \\ E(|\downarrow\uparrow\rangle) &= \frac{1}{2}(-\omega_I + \omega_S - J/2), \\ E(|\uparrow\downarrow\rangle) &= \frac{1}{2}(\omega_I - \omega_S - J/2), \\ E(|\uparrow\uparrow\rangle) &= \frac{1}{2}(\omega_I + \omega_S + J/2), \end{aligned} \tag{3.11}$$

where, as usual, $|\uparrow\rangle$ and $|\downarrow\rangle$ are the eigenstates of σ_z.

Observable transitions are transitions whose change in the magnetic quantum number Δm is equal to ± 1. As a result, the spectrum of the FID signal shows two doublets at frequencies corresponding to ΔE equal to $\omega_I \pm J/2$, and $\omega_S \pm J/2$.

Our goal is to collapse these doublets into singlets using non-selective rf. pulses.

First, examine the following Hamiltonian

$$\begin{aligned} H' &= k(\omega_I I_y + \omega_S S_y) + J I_z S_z \\ &= \omega'_I I_y + \omega'_S S_y + J I_z S_z. \end{aligned} \tag{3.12}$$

H' represents an effective y field which is linearly proportional to the original frequency offsets and perpendicular to the zz coupling term. In the interaction frame represented by $\omega'_I I_y + \omega'_S S_y$, the coupling term $J I_z S_z$ is oscillating and will therefore be averaged out to zero provided that $J \ll |\omega'_I \pm \omega'_S|$. It follows that the Hamiltonian (3.12) eliminates the coupling.

We now calculate the evolution of the FID signal under the Hamiltonian $\omega_I I_y + \omega_S S_y + J I_z S_z$. First, rewrite the Hamiltonian as

$$H = \omega^+ \frac{I_y + S_y}{2} + \frac{J}{2}(I_z S_z - I_x S_x) + \omega^- \frac{I_y - S_y}{2} + \frac{J}{2}(I_z S_z + I_x S_x), \tag{3.13}$$

where $\omega^+ = \omega_I + \omega_S$, $\omega^- = \omega_I - \omega_S$.

Let

$$H_1 = \omega^+ \frac{I_y + S_y}{2} + \frac{J}{2}(I_z S_z - I_x S_x),$$
$$H_2 = \omega^- \frac{I_y - S_y}{2} + \frac{J}{2}(I_z S_z + I_x S_x).$$

Since $H = H_1 + H_2$ and $[H_1, H_2] = 0$, the evolution operator is

$$U = e^{-iHt} = \underbrace{e^{-iH_1 t}}_{U_1} \underbrace{e^{-iH_2 t}}_{U_2}. \tag{3.14}$$

The density matrix for the initial state where both spins point in the x direction is

$$\rho(0) = \frac{1}{2}(\mathbf{1} + \sigma_x) \otimes \frac{1}{2}(\mathbf{1} + \sigma_x) \tag{3.15}$$

The operator that represents the sum of the magnetization of the two spins in the x direction is $I_x + S_x$. As mentioned in Sec. 3.2, we wish to normalize the intensity of spin half particles, so the actual operator used to measure the FID signal is $M_x = 2(I_x + S_x)$. Due to the form of the Hamiltonian, we can easily see that

$$\begin{aligned}
\langle M_x \rangle (t) &= \mathrm{tr}(U^\dagger \rho_0 M_x) \\
&= \mathrm{tr}(U^\dagger (I_x + S_x) U (I_x + S_x)) \\
&= \mathrm{tr}({U_2}^\dagger {U_1}^\dagger (I_x + S_x) U_1 U_2 (I_x + S_x)) \\
&= \mathrm{tr}({U_1}^\dagger (I_x + S_x) U_1 U_2 (I_x + S_x) {U_2}^\dagger).
\end{aligned} \tag{3.16}$$

Notice the following isomorphic copy of the spin operators

$$\begin{aligned}&\{\frac{I_y+S_y}{2}, I_zS_z - I_xS_x, I_xS_z + I_zS_x\}\\&\{\frac{I_y-S_y}{2}, I_zS_z + I_xS_x, I_xS_z - I_zS_x\}.\end{aligned} \tag{3.17}$$

We can rewrite the evolution operator U_1 as

$$\begin{aligned}U_1 &= e^{-i(\omega^+ \frac{I_y+S_y}{2} + \frac{J}{2}(I_zS_z - I_xS_x))t}\\&= e^{i\beta_1(I_xS_z+I_zS_x)}e^{-i\alpha_1 t\frac{I_y+S_y}{2}}e^{-i\beta_1(I_xS_z+I_zS_x)},\end{aligned} \tag{3.18}$$

where $\alpha_1 = \sqrt{(\omega^+)^2 + (\frac{J}{2})^2}$, $\cos\beta_1 = \frac{\omega^+}{\alpha_1}$, $\sin\beta_1 = \frac{-J/2}{\alpha_1}$.

We can now calculate the evolution of $I_x + S_x$ with the help of the following isomorphic copy of the spin operators

$$\begin{aligned}&\{2(I_xS_z + I_zS_x), I_x + S_x, 2(I_xS_y + I_yS_x)\},\\&\{I_x + S_x, I_y + S_y, I_z + S_z\},\\&\{2(I_xS_y + I_yS_x), I_y + S_y, 2(I_zS_y + I_yS_z)\},\\&\{I_z + S_z, 2(I_xS_z + I_zS_x), 2(I_yS_z + I_zS_y)\}.\end{aligned} \tag{3.19}$$

$$\begin{aligned}&U_1^\dagger(I_x + S_x)U_1 = \cos(\frac{\alpha_1 t}{2})(I_x + S_x) +\\&\cos\beta_1 \sin(\frac{\alpha_1 t}{2})(I_z + S_z) + 2\sin\beta_1 \sin(\frac{\alpha_1 t}{2})(I_yS_z + I_zS_y).\end{aligned} \tag{3.20}$$

Similarly, we can rewrite U_2 as

$$\begin{aligned}U_2 &= e^{-i(\omega^- \frac{I_y-S_y}{2} + \frac{J}{2}(I_zS_z + I_xS_x))t}\\&= e^{i\beta_2(I_xS_z - I_zS_x)}e^{-i\alpha_2 t\frac{I_y-S_y}{2}}e^{-i\beta_2(I_xS_z - I_zS_x)},\end{aligned} \tag{3.21}$$

where $\alpha_2 = \sqrt{(\omega^-)^2 + (\frac{J}{2})^2}$, $\cos\beta_2 = \frac{\omega^-}{\alpha_2}$, $\sin\beta_2 = \frac{-J/2}{\alpha_2}$.

Using the following sets

$$\begin{aligned}
&\{2(I_xS_z - I_zS_x), I_x + S_x, 2(I_xS_y - I_yS_x)\},\\
&\{I_x + S_x, I_y - S_y, I_z - S_z\},\\
&\{2(I_xS_y - I_yS_x), I_y - S_y, 2(I_zS_y + I_yS_z)\},\\
&\{I_z - S_z, 2(I_xS_z - I_zS_x), 2(I_yS_z + I_zS_y)\},
\end{aligned} \tag{3.22}$$

we can calculate the evolution of $I_x + S_x$ under H_2

$$\begin{aligned}
&U_2(I_x + S_x)U_2^\dagger = \cos(\frac{\alpha_2 t}{2})(I_x + S_x) -\\
&\cos\beta_2 \sin(\frac{\alpha_2 t}{2})(I_z - S_z) - 2\sin\beta_2 \sin(\frac{\alpha_2 t}{2})(I_yS_z + I_zS_y).
\end{aligned} \tag{3.23}$$

Therefore,

$$\begin{aligned}
&\langle I_x + S_x\rangle = {}_{\mathrm{tr}}(U_1{}^\dagger(I_x + S_x)U_1U_2(I_x + S_x)U_2{}^\dagger)\\
&= 2\cos(\frac{\alpha_1 t}{2})\cos(\frac{\alpha_2 t}{2}) - 2\sin\beta_1 \sin\beta_2 \sin(\frac{\alpha_1 t}{2})\sin(\frac{\alpha_2 t}{2})\\
&= (1 + \sin\beta_1 \sin\beta_2)\cos(\frac{\alpha_1 + \alpha_2}{2}t)\\
&+ (1 - \sin\beta_1 \sin\beta_2)\cos(\frac{\alpha_1 - \alpha_2}{2}t).
\end{aligned} \tag{3.24}$$

Substitute the values of $\alpha_{1,2}$ and $\beta_{1,2}$ in terms of $\omega_{I,S}$ and J, we arrive at the final result. The FID signal is the sum of two sinusoids with frequencies

$$\frac{1}{2}\left(\sqrt{(\omega_I + \omega_S)^2 + (J/2)^2} \pm \sqrt{(\omega_I - \omega_S)^2 + (J/2)^2}\right) \tag{3.25}$$

having the corresponding intensities

$$1 \pm \frac{J^2}{\sqrt{J^2 + 4(\omega_I + \omega_S)^2}\sqrt{J^2 + 4(\omega_I - \omega_S)^2}}. \tag{3.26}$$

In the limit $J \ll |\omega_I - \omega_S|$, the frequencies simplify to

$$\begin{aligned}
&\omega_I + \frac{1}{16}\left(\frac{J^2}{\omega_I + \omega_S} + \frac{J^2}{\omega_I - \omega_S}\right),\\
&\omega_S + \frac{1}{16}\left(\frac{J^2}{\omega_I + \omega_S} - \frac{J^2}{\omega_I - \omega_S}\right)
\end{aligned} \tag{3.27}$$

and the intensities are almost equal to 1.

That means the spectrum of the FID signal now contains two singlets, instead of two doublets as in the case of H_{Ising}. This is a clear advantage because the singlets have almost equal intensity that are double the intensities of the doublets. The positions of the peaks, however, depend on J. Nevertheless, it is only a weak dependence, so under the condition $J \ll |\omega'_I - \omega'_S|$, where ω'_I and ω'_S are the scaled chemical shifts, we can resolve the resonances to high accuracy even when J is not known precisely.

In the next subsections, we describe a pulse sequence that produces the Hamiltonian H' and then verify its performance by simulation.

3.2.1 The 4-segment pulse sequence

In order to synthesize the Hamiltonian H', we evolve the system under the following four Hamiltonians, each for a small time interval Δt.

$$\begin{aligned} H_1 =& \omega_I I_z + \omega_S S_z + J I_z S_z + A(I_x + S_x), \\ H_2 =& -\omega_I I_z - \omega_S S_z + J I_z S_z + A(I_x + S_x), \\ H_3 =& -\omega_I I_z - \omega_S S_z + J I_z S_z - A(I_x + S_x), \\ H_4 =& \omega_I I_z + \omega_S S_z + J I_z S_z - A(I_x + S_x). \end{aligned} \tag{3.28}$$

These Hamiltonians are realized by applying rf fields in the x direction, and hard π pulses to both spins. We name this a 4-segment pulse sequence; its implementation is illustrated in Fig. 3.1b. In the interaction frame of the Zeeman terms, i.e. the frame represented by $\omega_I I_z + \omega_S S_z$, $-\omega_I I_z - \omega_S S_z$, $-\omega_I I_z - \omega_S S_z$, $\omega_I I_z + \omega_S S_z$ each for an interval Δt, the x components of the rf fields cancel out after four intervals of evolution, while the y components add up. If $\omega_I \Delta t$ is a small angle, then in each

period Δt, the y component of spin I evolves as $\int_0^{\Delta t} A\sin(\omega_I t)dt \approx A(\Delta t)^2\omega_I/2$, a term linear in ω_I. The coupling term JI_zS_z is unaffected since it commutes with the Zeeman terms. As a result, we get a Hamiltonian of the form H' as desired. Similar cycles of the rf Hamiltonian have been recently proposed to design small tip angle-excitation pulses that are robust to rf inhomogeneity [35].

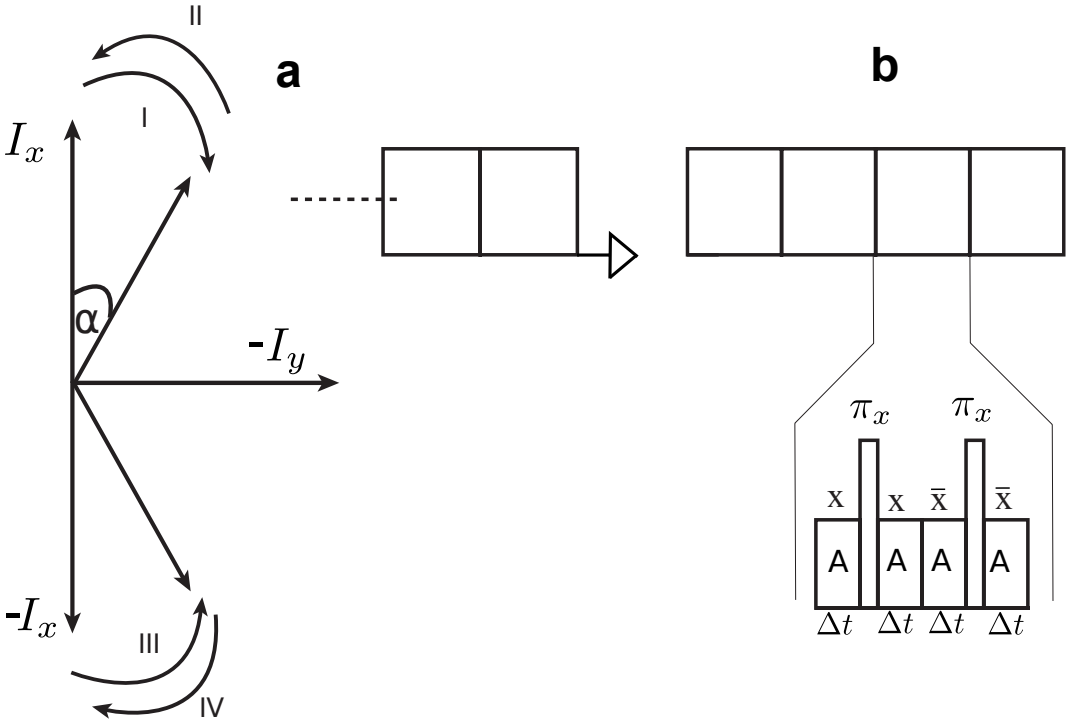

Figure 3.1: (a) shows the evolution of the rf Hamiltonian for spin I in the toggling frame of the chemical shift Hamiltonian. The four stages of the cycle, corresponding to the chemical shift Hamiltonian being $(\omega_I I_z+\omega_S S_z)$, $-(\omega_I I_z+\omega_S S_z)$, $-(\omega_I I_z+\omega_S S_z)$ and $(\omega_I I_z + \omega_S S_z)$, are numbered in the figure. (b) shows a block of the 4-segment pulse sequence that makes the chemical shift and the rf Hamiltonian execute the cycle in (a). This basic building block is repeated throughout the decoupling time. Short windows of free evolution to acquire the signal are denoted by the arrow in the figure.

We now calculate the effective Hamiltonian due to the four stage Hamiltonian in Eq. (3.28), i.e. find H_{eff} such that the unitary operator generated by this 4-segment

pulse sequence

$$U = e^{-iH_4\Delta t}e^{-iH_3\Delta t}e^{-iH_2\Delta t}e^{-iH_1\Delta t} \tag{3.29}$$

can be written as

$$U = e^{-i4(\Delta t)H_{\text{eff}}}. \tag{3.30}$$

Before we proceed, there are a few assumptions to be made. First, we require that the frequency offsets be dispersed over a certain range $[-B, B]$, i.e, $|\omega_I|, |\omega_S| < B$, and secondly Δt be chosen such that $\sqrt{B^2 + A^2}\Delta t \ll 1$.

We use the Baker Campbell Hausdorff formula

$$e^A e^B = e^{A+B+\frac{1}{2}[A,B]+\frac{1}{12}([A,[A,B]]-[B,[A,B]])+\ldots}, \tag{3.31}$$

to calculate U, keeping terms up to the third order in Δt, we have

$$\begin{aligned}
U_1 &= e^{-iH_2\Delta t}e^{-iH_1\Delta t} \\
&= \exp(-i\Delta t 2(JI_zS_z + A(I_x + S_x))+ \\
&i(\Delta t)^2 A(\omega_I I_y + \omega_S S_y) + i\frac{(\Delta t)^3}{3}A(\omega_I^2 I_x + \omega_S^2 S_x)), \\
U_2 &= e^{-iH_4\Delta t}e^{-iH_3\Delta t} \\
&= \exp(-i\Delta t 2(JI_zS_z - A(I_x + S_x))+ \\
&i(\Delta t)^2 A(\omega_I I_y + \omega_S S_y) - i\frac{(\Delta t)^3}{3}A(\omega_I^2 I_x + \omega_S^2 S_x)).
\end{aligned}$$

The total evolution is $U = U_2U_1$.

$$\begin{aligned}
U = \exp(&-4i(\Delta t)JI_zS_z + 2i(\Delta t)^2 A(w_I I_y + w_S S_y) \\
&- 4i(\Delta t)^2 AJ(I_yS_z + I_zS_y) - 2i(\Delta t)^3 A^2(w_I I_z + w_S S_z) \\
&- 16i(\Delta t)^3 A^2 J(I_yS_y - I_zS_z) + O((\Delta t)^4).
\end{aligned} \tag{3.32}$$

The effective Hamiltonian, therefore, has terms up to the second order in Δt.

$$\begin{aligned} H_{\text{eff}} &= JI_zS_z - \frac{1}{2}\theta(\omega_I I_y + \omega_S S_y) + \theta J(I_yS_z + I_zS_y) \\ &+ \frac{1}{2}\theta^2(\omega_I I_z + \omega_S S_z) + \frac{4}{3}\theta^2 J(I_yS_y - I_zS_z) + O((\theta)^3), \end{aligned} \tag{3.33}$$

where $\theta = A\Delta t$. θ has to satisfy the condition $\theta \ll 1$.

The first two terms are precisely what we are seeking to create: the main coupling stays in the z direction, while the main field is scaled down by a factor of $\frac{1}{2}\theta$ and points in the y direction. However, there is a residual field along the z direction, and a coupling term in the y direction that need to be taken into account.

The combined effect of the fields in the y direction, $-\frac{1}{2}\theta(\omega_I I_y + \omega_S S_y)$, and z direction, $\frac{1}{2}\theta^2(\omega_I I_z + \omega_S S_z)$, creates a field pointing in the y' direction, as illustrated in Fig. 3.2.

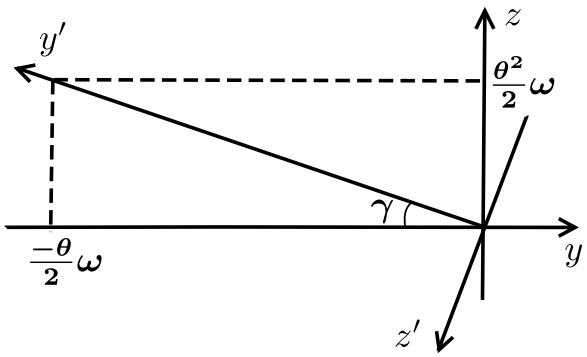

Figure 3.2: The coordinate transformation that aids the calculation of the effective field and coupling strength.

The transformation to the new coordinate $xy'z'$ yields

$$\begin{aligned} I_y &= -\cos\gamma I_{y'} - \sin\gamma I_{z'}, \\ I_z &= \sin\gamma I_{y'} - \cos\gamma I_{z'}, \end{aligned} \tag{3.34}$$

where $\tan\gamma = \theta$. Hence, to first order in θ, the Zeeman Hamiltonian is $\frac{\theta}{2}(w_I I_{y'} + w_S S_{y'})$. Since the effective field points entirely in the y' direction, the most important coupling is the $y'y'$ term. We get this term by projecting the coupling terms in Eq. (3.33) parallel and perpendicular to the effective field in the y' direction and retaining only the parallel component. The coupling strength up to the second order in θ is therefore

$$J' = \frac{1}{3}\theta^2 J, \quad \text{for } \theta \ll 1. \tag{3.35}$$

In summary, when $\theta \ll 1$, the most important terms in the effective Hamiltonian are

$$H'_{\text{eff}} = \frac{\theta}{2}(\omega_I I_{y'} + \omega_S S_{y'}) + \frac{\theta^2}{3} J I_{y'} S_{y'}. \tag{3.36}$$

That means the frequency offsets of the spins are scaled down as θ, while the coupling strength is scaled down as θ^2. Since θ is known, the chemical shift information is preserved. Theoretically, as θ goes to zero, the coupling will vanish. However, scaling down the offsets too much is not preferable because this degrades the resolution. In the simulation section, we will show how to choose θ that works for practical purposes. Finally, assuming no rf-inhomogeneity, we can make the effective Zeeman interaction point along the z axis by appropriate rf rotations.

3.2.2 Simulation results

We verify the effectiveness of this 4-segment pulse sequence by simulation. First, let us identify the relevant parameters. A typical value for J-coupling between protons in the study of amino acids by NMR spectroscopy is $J/(2\pi) = 10$ Hz. For example, $J_{H^N H^\alpha}/(2\pi) = 10$ Hz, $J_{H^\alpha H^\beta}/(2\pi) = 12$ Hz [7]. The chemical shifts of protons are on

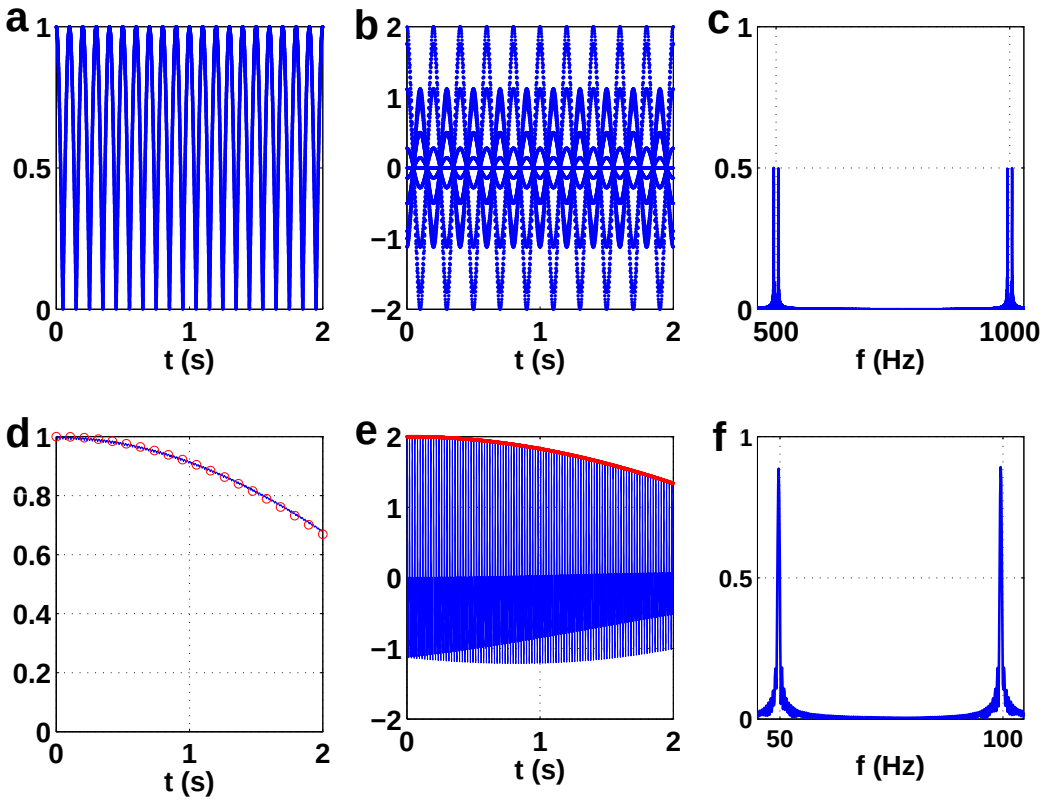

Figure 3.3: This figure shows the simulation results for the Ising coupling. The parameters used are $\omega_I/(2\pi) = 0.5$ kHz, $\omega_S/(2\pi) = 1$ kHz, $J/(2\pi) = 10$ Hz, $\Delta t = 31.8$ μs, $A/(2\pi) = 1$ kHz, $\theta = 1/5$. The observation time is 2 s. All π pulses are assumed to be ideal delta pulses with negligible durations. The first row shows the results for the coupled system. The second row shows the results for the decoupled system due to the application of the 4-segment decoupling sequence. (a) and (d) show the evolution of the total magnetization of spin I, $\sqrt{\langle I_x\rangle^2 + \langle I_y\rangle^2 + \langle I_z\rangle^2}$. In (d), the red circles are the plot of $\cos(\theta^2 Jt/6)$, which perfectly matches the simulation result. (b) and (e) show the evolution of the total x-magnetization of the two spins (the FID signal). (c) and (f) show the Fourier transform of the FID. The locations of the peaks are exactly as expected. It is clear that the applied pulse sequence shows great improvement in preserving the magnetization and increasing the intensity of the peaks.

the order of a few ppm, which for a 500 MHz proton Larmor frequency spectroscopy translates into a few kHz [7]. We want to keep the rf field small, so a value of $A/(2\pi) = 1$ kHz is chosen. Δt is set equal to 31.8 μs such that $\theta = A\Delta t = 1/5$. This

value of θ would scale $J/(2\pi)$ from 10 Hz to 0.13 Hz. An observation time of 2 s is long enough for many experiments. For these parameters, we run simulations for different values of offsets in the range [0, 3] kHz where the condition $\sqrt{A^2+\omega_{I,S}^2}\Delta t \ll 1$ is satisfied.

Starting with the initial state where both spins point in the positive x direction, we simulate the evolution of $s(t) = \langle I_x + S_x \rangle(\mathrm{t})$. In the absence of decoupling, the FID signal $s(t)$ is

$$s(t) = [\cos(\omega_I t) + \cos(\omega_S t)] \cos(\frac{1}{2} J t). \tag{3.37}$$

The coupling term creates an envelope of frequency $\frac{1}{2}J$ on top of a signal that is the sum of two sinusoids. This results in a spectrum that has two doublets, each consisting of two peaks a distance J apart. The coupling can also be easily observed by measuring the total magnetization of one spin, since

$$\sqrt{\langle I_x \rangle^2 + \langle I_y \rangle^2 + \langle I_z \rangle^2} = \cos(\frac{1}{2} J t). \tag{3.38}$$

From Eq. (3.36), the magnetization of spin I should decay at a much slower rate, $\frac{\theta^2}{6}J$, after the application of the decoupling sequence. This is confirmed by simulation. The Fourier spectrum of the decoupled system shows two sharp peaks having a much higher intensity, as shown in Fig. 3.3 for a particular pair of frequency offsets.

In summary, in this section we have proposed a pulse sequence that decouples the Ising term. The sequence is comprised of two hard π pulses and four rf pulses. As a result of this sequence, the frequency offsets are scaled down by a factor of $\frac{1}{2}(A\Delta t)$, while the coupling strength is scaled down by a factor of $\frac{1}{3}(A\Delta t)^2$, where A is the rf amplitude and Δt is a small time, two parameters that are under our control. Effective decoupling is achieved when $A\Delta t$ is small enough.

3.3 Isotropic coupling - weaker coupling strength

The decoupling sequence described in the previous section is only effective for Ising coupling. When applied to the isotropic coupling, $I_xS_x + I_yS_y + I_zS_z$, the planar term $(I_xS_x + I_yS_y)$ is not averaged out, leading to a quick decay of the signal, as shown in Fig. 3.4a. In this section, we attempt to modify the sequence to decouple a system that has isotropic coupling.

The principle behind the design of the new sequence is that we first eliminate $I_xS_x + I_yS_y$, thereby reducing the problem of isotropic coupling, $I \cdot S$, to the problem of Ising coupling, I_zS_z, which we already know how to solve.

We start by rewriting the Hamiltonian as

$$\begin{aligned} H &= \omega_I I_z + \omega_S S_z + J(I \cdot S) \\ &= \omega^+ \frac{I_z + S_z}{2} + \omega^- \frac{I_z - S_z}{2} + J(I_xS_x + I_yS_y) + JI_zS_z, \end{aligned} \tag{3.39}$$

where $\omega^+ = \omega_I + \omega_S,\ \omega^- = \omega_I - \omega_S$.

Observe that the following operators

$$\left(I_xS_x + I_yS_y, \frac{I_z - S_z}{2}, I_xS_y - I_yS_x \right) \tag{3.40}$$

form a $\mathfrak{su}(2)$ algebra, i.e. they obey the same commutation rules as $\{I_x, I_y, I_z\}$. Thus, evolution under $I_z - S_z$ for time $\frac{\pi}{\omega^-}$ will invert $I_xS_x + I_yS_y$. We then need to choose the right free evolution times so as to cancel exactly the effect of positive $I_xS_x + I_yS_y$ created during the application of the 4-segment pulse sequence needed to eliminate I_zS_z. This is illustrated in Fig. 3.4b.

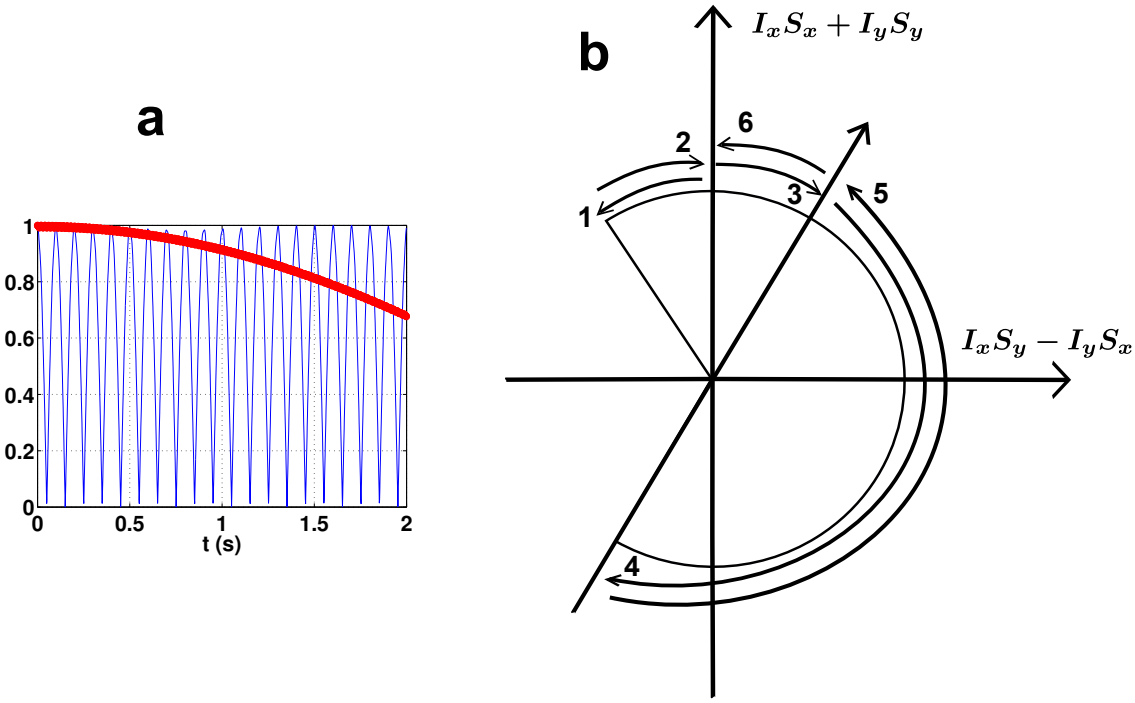

Figure 3.4: (a) plots $\sqrt{\langle I_x\rangle^2 + \langle I_y\rangle^2 + \langle I_z\rangle^2}$ as a function of time under the application of the 4-segment pulse sequence. The red, slowly decaying curve shows the result for the Ising system, and the blue, fast oscillating curve shows the result for the isotropic system. (b) shows the conception of the new sequence by examining the evolution of the planar coupling in the interaction frame of the Zeeman terms. The 4-segment pulse sequence represented by four small arcs, numbered 1, 2, 3, 6, creates $I_xS_x + I_yS_y$ in the positive direction. The two additional free evolution times represented by the two large arcs, numbered 4, 5, create $I_xS_x + I_yS_y$ in the negative direction.

3.3.1 The 6-segment pulse sequence

The following 6-segment pulse sequence aims to first cancel $I_xS_x + I_yS_y$ through free evolution periods, then use rf pulses similar to the original 4-segment pulse se-

quence to eliminate I_zS_z.

$$\begin{aligned}
H_1 =&\omega_I I_z + \omega_S S_z + J(I\cdot S) + A(I_x + S_x), && \Delta t,\\
H_2 =&-\omega_I I_z - \omega_S S_z + J(I\cdot S) + A(I_x + S_x), && \Delta t,\\
H_3 =&-\omega_I I_z - \omega_S S_z + J(I\cdot S) - A(I_x + S_x), && \Delta t,\\
H_4 =&-\omega_I I_z - \omega_S S_z + J(I\cdot S), && \tau = \pi/\omega^-,\\
H_5 =&\omega_I I_z + \omega_S S_z + J(I\cdot S), && \tau = \pi/\omega^-,\\
H_6 =&\omega_I I_z + \omega_S S_z + J(I\cdot S) - A(I_x + S_x), && \Delta t.
\end{aligned} \tag{3.41}$$

The times on the right show the durations for which each Hamiltonian evolves.

We analyze the pulse sequence in the interaction frame of the Zeeman terms. As argued earlier, the free evolution periods represented by H_4 and H_5 help eliminate $I_xS_x + I_yS_y$, leaving only the Ising coupling term. At the same time, the frequency offsets do not really evolve in these periods. We therefore expect that this 6-segment pulse sequence also scales down the I_zS_z coupling and the frequency offsets in the same way that the 4-segment pulse sequence does. We now show a detailed calculation using the average Hamiltonian theory to verify these claims.

The Hamiltonian can be split into two terms

$$H(t) = H_o(t) + V_o(t), \tag{3.42}$$

where $H_o(t)$ contains the linear Zeeman terms, $\pm(\omega_I I_z + \omega_S S_z)$ in different periods of time as specified in Eq. (3.41), and $V_o(t)$ contains the coupling term and the rf. We now go into the interaction frame of the Zeeman term, $H_o(t)$, that produces the unitary operator $U_o(t)$ such that

$$\frac{dU_o(t)}{dt} = -iH_o(t)U_o(t). \tag{3.43}$$

Since $U_o(4\Delta t+2\tau) = \mathbf{1}$, i.e the sequence is cyclic, at the end of the pulse sequence, the state in the interaction frame is the same as the state in the lab frame. Therefore, we do not need to do an inverse transformation, and only have to calculate the effective Hamiltonian in this interaction frame.

$$\bar{V}(t) = U_o^{\dagger}(t)V_o(t)U_o(t). \tag{3.44}$$

It is easy to see that

$$\begin{aligned} U_o(t) &= e^{-i(\omega_I I_z+\omega_S S_z)t}, && 0 < t < \Delta t, \\ U_o(t) &= e^{-i(\omega_I I_z+\omega_S S_z)(2\Delta t-t)}, && \Delta t < t < 3\Delta t + \tau, \\ U_o(t) &= e^{-i(\omega_I I_z+\omega_S S_z)(t-(4\Delta t+2\tau))}, && 3\Delta t + \tau < t < 4\Delta t + 2\tau. \end{aligned} \tag{3.45}$$

Notice that $[I_z + S_z, I_xS_x + I_yS_y] = 0$ and recall Eqs. (3.39) and (3.40), we can calculate the effective Hamiltonian for the coupling term $V_o(t) = I_xS_x + I_yS_y$ as follows

$$\begin{aligned} &e^{i(\omega_I I_z+\omega_S S_z)t}V_o(t)e^{-i(\omega_I I_z+\omega_S S_z)t} = \\ &\cos(\omega^- t)(I_xS_x + I_yS_y) + \sin(\omega^- t)(I_xS_y - I_yS_x). \end{aligned} \tag{3.46}$$

The total value of $(I_xS_x + I_yS_y)$ coupling is therefore

$$\begin{aligned} \int \bar{V}_o(t)dt &= J\left(\int_0^{\Delta t}\cos(\omega^- t) + \int_{\Delta t}^{3\Delta t+\tau}\cos(\omega^-(2\Delta t - t))\right. \\ &\left. + \int_{3\Delta t+\tau}^{4\Delta t+2\tau}\cos(t-(4\Delta t+2\tau))\right)dt \\ &= \frac{2J}{\omega^-}\left(\sin(\omega^-\Delta t) + \sin(\omega^-(\Delta t+\tau))\right). \end{aligned} \tag{3.47}$$

If ω^- is known definitely, we can choose $\tau = \pi/\omega^-$, and the above expression becomes identically zero, i.e., $I_xS_x + I_yS_y$ is eliminated in the first order. The term

$I_xS_y - I_yS_x$ is nonzero, but this does not contribute to the coupling, as the effective field in the y direction averages it out.

3.3.2 Scaling of the frequency offsets

We now calculate the effective frequency offsets resulting from the rf pulses. This is also best done in the interaction frame of the Zeeman Hamiltonian represented by $U_o(t)$.

For a time varying Hamiltonian $H(t)$, the average Hamiltonian between the time 0 and T in the zeroth order is

$$H^{(0)} = \frac{1}{T}\int_0^T dt H(t). \tag{3.48}$$

From the identity

$$e^{i\omega_I I_z t} A I_x e^{-i\omega_I I_z t} = A(I_x \cos(\omega_I t) - I_y \sin(\omega_I t)), \tag{3.49}$$

it is easy to see that through the four evolution times of the rf field, the x components cancel out and the y components add up. Hence, the total effective field in the zeroth order average Hamiltonian is

$$\begin{aligned} &\frac{1}{4\Delta t} 4 \int_0^{\Delta t} dt[-A\sin(\omega_I t) I_y - A\sin(\omega_S t) S_y] = \\ &- \left[\mathrm{sinc}^2(\frac{\omega_I \Delta t}{2}) \frac{A\Delta t}{2} \omega_I I_y + \mathrm{sinc}^2\left(\frac{\omega_S \Delta t}{2}\right) \frac{A\Delta t}{2} \omega_S S_y\right]. \end{aligned} \tag{3.50}$$

Notice that we count the evolution as if it happened only in time $4\Delta t$ instead of $4\Delta t + 2\tau$. This is completely justified because there is no rf field in stages 4 and 5 of the pulse sequence. The effective Zeeman evolution from these stages is zero, so we only need to sum the contributions from stages $1, 2, 3, 6$, i.e. in total time $4\Delta t$.

If the transverse magnetization $\langle I_x + S_x \rangle$ is measured, we will observe two peaks at scaled frequency offsets

$$\text{sinc}^2\left(\frac{\omega_I \Delta t}{2}\right)\frac{\theta}{2}\omega_I \quad \text{and} \quad \text{sinc}^2\left(\frac{\omega_S \Delta t}{2}\right)\frac{\theta}{2}\omega_S,$$

where $\theta = A\Delta t$.

In the limit where $\omega\Delta t$ goes to zero, $\text{sinc}(\omega\Delta t/2)$ goes to 1, and we get back the simple linear scaling as in the 4-segment pulse sequence case. Here, Δt is kept small such that $\Delta t\omega/2 < 1$ and the scaling is almost linear over a wide range of frequency offsets ω. Most importantly, there is a one-to-one mapping between the original and the scaled frequency offsets, as shown in Fig. 3.5.

3.3.3 Compensating cycle for the case of unknown ω^-

In Eq. (3.47), if ω^- is known, we can exactly eliminate the effect of $I_xS_x + I_yS_y$ by choosing $\tau = \pi/\omega^-$. In this subsection, we show how to cancel this planar coupling term when ω^- has a spread, as often the case in practical applications. This is achieved by concatenating several decoupling blocks, each with a different free evolution time $\{\tau_i\}$, $i = 1, 2, \ldots, m$ such that the combined effect of these eliminates the planar coupling term.

Denote ω_o^- as the nominal frequency difference. The actual frequency difference, ω^-, is equal to $\omega^- = \omega_o^-(1+\delta)$, where δ is the range $[0,\ \Delta]$ with Δ given. The total planar coupling $I_xS_x + I_yS_y$ for each $\omega^-(\delta)$ in m blocks is $2Jf(\delta)$, where

$$f(\delta) = \sum_{i=1}^{m}\left[\frac{\sin((1+\delta)\omega_o^-\Delta t) + \sin((1+\delta)\omega_o^-(\Delta t + \tau_i))}{(1+\delta)\omega_o^-}\right]. \tag{3.51}$$

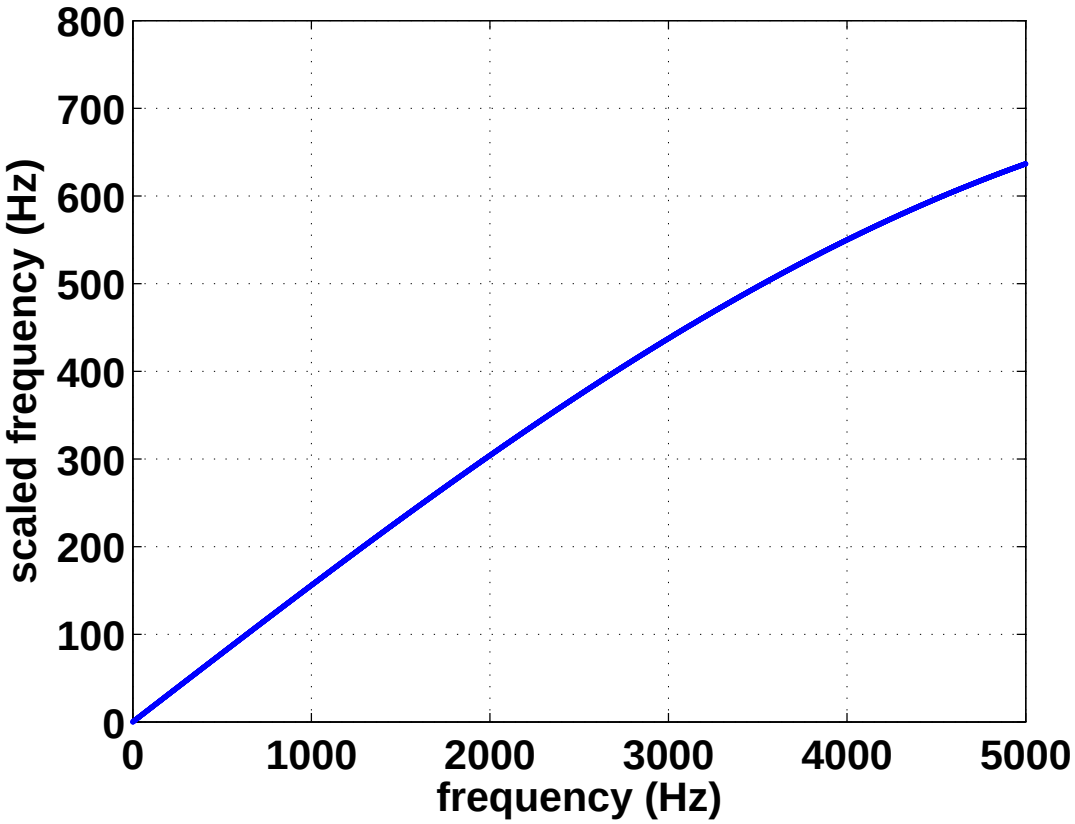

Figure 3.5: Almost linear scaling of the frequency offsets for the 6-segment pulse sequence. The horizontal axis shows the frequency $\omega/(2\pi)$. The vertical axis shows the scaled frequency $\mathrm{sinc}^2\left(\frac{\omega\Delta t}{2}\right)\frac{A\Delta t}{2}\frac{\omega}{2\pi}$. In this plot $\Delta t = 50\mu$s. $A/(2\pi) = 1$ kHz.

We need to find $\{\tau_i\}$, $i = 1, 2, \ldots, m$ such that $f(\delta)$ is close to zero for all δ in the desired range.

Each basic building block of this 6-segment pulse sequence is shown in Fig. 3.6.

3.3.4 Simulation results

We minimize $f(\delta)$ numerically according to Eq. (3.51) for δ in the range $[0, 0.5]$, i.e. 50% tolerance in ω^- for a system with the following parameters:

$J/(2\pi) = 10$ Hz, $\omega_o^-/(2\pi) = 1$ kHz, $\Delta t = 50\mu$s, $\theta = \pi/10$, $A/(2\pi) = 1$ kHz.

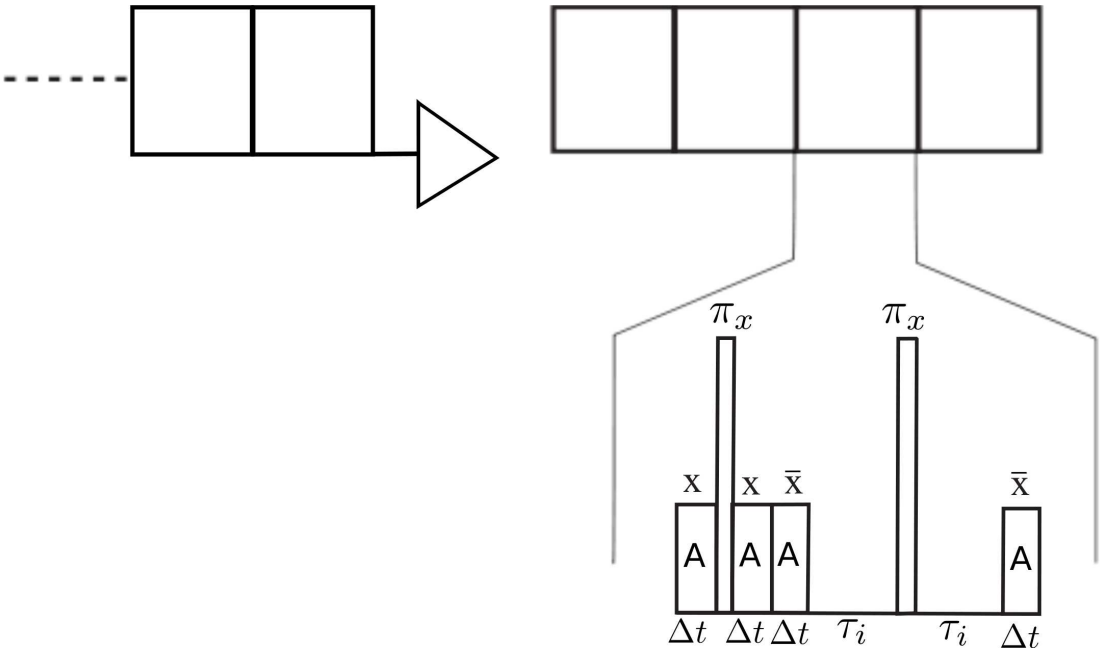

Figure 3.6: A basic building block of the 6-segment decoupling pulse sequence that is repeated throughout the decoupling time. The free evolution times τ_i vary for different blocks and are determined by minimizing the quantity in Eq. (3.51).

According to Eq. (3.51), only ω_o^-, Δt, the range of δ, and m, the number of compensating blocks, are needed for the optimization. We choose m equal to 4, since this gives satisfactory results and the total time of the compensating blocks is not too long. The numerical values found are:

$\{\tau_i\} = \{0.4434,\ 0.5197,\ 0.6151,\ 0.9511\}$ ms.

Notice that these values vary around the nominal value $\pi/\omega_o^- = 0.5$ ms, which partly explains why they successfully minimize the sum.

Figure 3.7 shows the results obtained by simulation for systems that have frequency offset difference, ω^-, in the range $[\omega_o^-,\ 1.5\ \omega_o^-]$. As expected, decoupling is achieved across the dispersion in ω^-. The original offsets are found according to the one-to-one mapping in Fig. 3.5. Precise knowledge of J is not required in the

procedure.

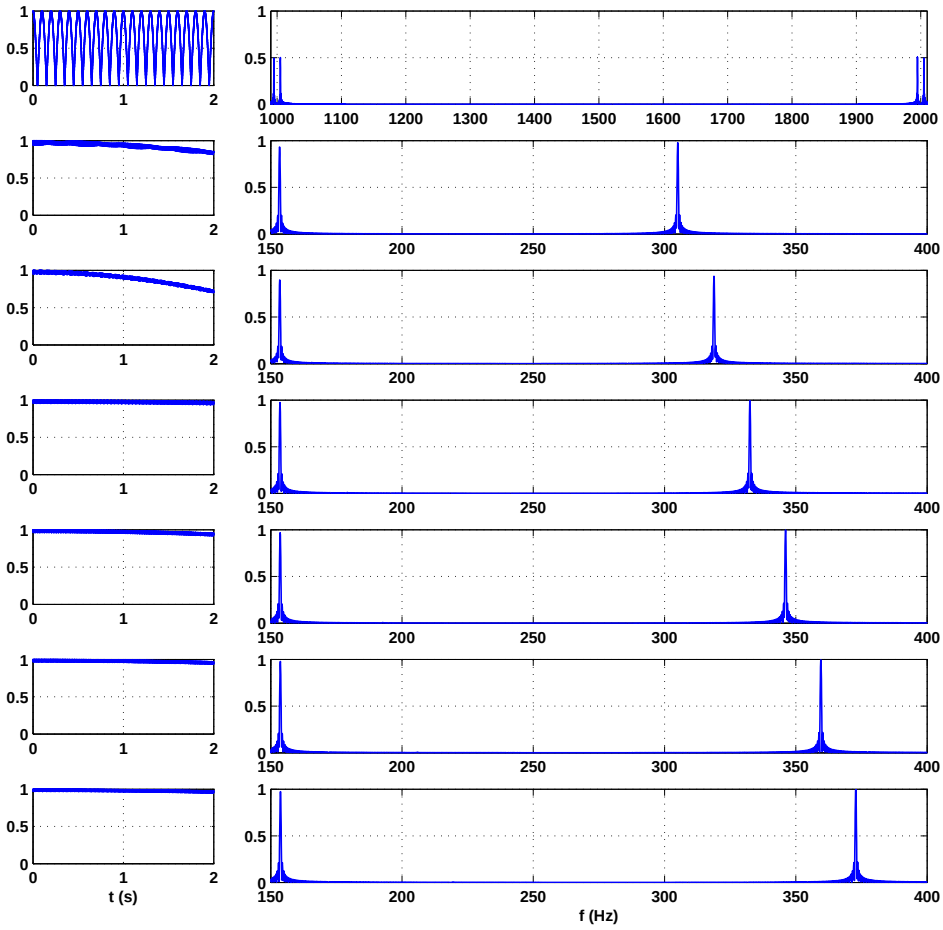

Figure 3.7: The first row shows the signal and spectrum of a coupled system with isotropic coupling $J/(2\pi) = 10$ Hz, $\omega_I/(2\pi) = 1$ kHz, $\omega_S/(2\pi) = 2$ kHz. The remaining rows show the results due to decoupling for a system that has $J/(2\pi) = 10$ Hz, $\omega_I/(2\pi) = 1$ kHz, $\omega_S/(2\pi) = [2, 2.1, 2.2, 2.3, 2.4, 2.5]$ kHz. The first column plots $\sqrt{\langle I_x\rangle^2 + \langle I_y\rangle^2 + \langle I_z\rangle^2}$, the second column plots the Fourier transform of the FID signal $\langle I_x + S_x\rangle$. The designed parameters are $\Delta t = 50\ \mu s$, $A/(2\pi) = 1$ kHz, $\{\tau_i\} = \{0.4434, 0.5197, 0.6151, 0.9511\}$ ms. All π pulses are ideal δ pulses with negligible durations. The results show the robustness of the pulse sequence over the dispersion of the chemical shift difference.

3.3.5 Discussion

We first discuss the details of sampling. Even though each control block is $4\Delta t+2\tau_i$ long, we only count it as $4\Delta t$ for signal processing purposes, since the frequency offsets barely evolve during the free evolution periods. We can sample faster at time intervals $\Delta t,\ 2\Delta t,\ 3\Delta t,\ 4\Delta t + 2\tau_i$, and the performance is as good as sampling at the end of each block. However, since the frequencies are scaled down, we do not need to sample very fast to capture all the frequency components.

Secondly, we want to make a note about the strength of the coupling. The above sequence successfully reduces the problem of isotropic coupling to the problem of Ising coupling. However, as a tradeoff, it actually enhances the strength of the original I_zS_z coupling during the long free evolution time. This large coupling, even in the perpendicular direction to the effective y field, can obscure the real peaks as can be seen from Eq. (3.27). This is why the sequence is only effective for relatively weak coupling strength. However, our simulation above shows that the performance might be adequate for many practical applications.

In conclusion, in this section we design a pulse sequence that successfully decouples an isotropically coupled system, but only for very small values of J compared to ω^-. The advantage of this sequence is that it has a simple, almost linear scaling of the frequency offsets over a broad range.

3.4 Isotropic coupling - stronger coupling strength

The previous section analyzes a decoupling sequence that almost linearly scales down the frequency offsets. This 6-segment pulse sequence eliminates the effect of $I_xS_x + I_yS_y$ by adding free evolution times, and uses a rf pulse to decouple I_zS_z.

In this section, we come back to the original 4-segment pulse sequence and show that with longer evolution times Δt, the sequence can simultaneously eliminate $I_xS_x + I_yS_y$ and I_zS_z with larger coupling strength. There are two trade-offs: a nonlinear scaling of the frequency offsets, and the loss of one-to-one mapping between the original and the scaled frequency offsets. We will show how to circumvent this problem by identifying the range of frequency of interest where a one-to-one mapping exists.

The full Hamiltonian including the control is once again as follows

$$\begin{aligned} H_1 =& \omega_I I_z + \omega_S S_z + J(I \cdot S) + A(I_x + S_x), \\ H_2 =& -\omega_I I_z - \omega_S S_z + J(I \cdot S) + A(I_x + S_x), \\ H_3 =& -\omega_I I_z - \omega_S S_z + J(I \cdot S) - A(I_x + S_x), \\ H_4 =& \omega_I I_z + \omega_S S_z + J(I \cdot S) - A(I_x + S_x), \end{aligned} \tag{3.52}$$

where each Hamiltonian is maintained for a time Δt.

In order to calculate average Hamiltonian in Eq. 3.52, we go into the interaction frame of the Zeeman term. The resulting Hamiltonian is denoted by $V_o(T)$

$$\begin{aligned} V_o(t) &= J(I \cdot S) + A(I_x + S_x) | U_o(t) = e^{-i(\omega_I I_z + \omega_S S_z)t}, \\ V_o(t) &= J(I \cdot S) + A(I_x + S_x) | U_o(t) = e^{-i(\omega_I I_z + \omega_S S_z)(2\Delta t - t)}, \\ V_o(t) &= J(I \cdot S) - A(I_x + S_x) | U_o(t) = e^{i(\omega_I I_z + \omega_S S_z)(t - 2\Delta t)}, \\ V_o(t) &= J(I \cdot S) - A(I_x + S_x) | U_o(t) = e^{i(\omega_I I_z + \omega_S S_z)(4\Delta t - t)}, \end{aligned} \tag{3.53}$$

for time $0 < t < \Delta t$, $\Delta t < t < 2\Delta t$, $2\Delta t < t < 3\Delta t$, $3\Delta t < t < 4\Delta t$, respectively.

Denote the $\mathfrak{su}(2)$ $\{I_xS_x + I_yS_y, \frac{I_z - S_z}{2}, I_xS_y - I_yS_x\}$ as $\{E, F^-, G\}$. The effective Hamiltonian in the four time intervals are

$$
\begin{aligned}
&\bar{V}_1(t) = JI_zS_z + JE\cos(\omega^- t) + JG\sin(\omega^- t) + \\
&A[I_x\cos(\omega_I t) - I_y\sin(\omega_I t) + S_x\cos(\omega_S t) - S_y\sin(\omega_S t)] \\
&= f_1(t), \\
&\bar{V}_2(t) = JI_zS_z + JE\cos(\omega^-(2\Delta t - t)) + JG\sin(\omega^-(2\Delta t - t)) \\
&+ A[I_x\cos(\omega_I(2\Delta t - t)) - I_y\sin(\omega_I(2\Delta t - t)) + \\
&S_x\cos(\omega_S(2\Delta t - t)) - S_y\sin(\omega_S(2\Delta t - t))] \\
&= f_1(2\Delta t - t), \\
&\bar{V}_3(t) = JI_zS_z + JE\cos(\omega^-(t - 2\Delta t)) - JG\sin(\omega^-(t - 2\Delta t)) \\
&+ A[-I_x\cos(\omega_I(t - 2\Delta t)) - I_y\sin(\omega_I(t - 2\Delta t)) - \\
&S_x\cos(\omega_S(t - 2\Delta t)) - S_y\sin(\omega_S(t - 2\Delta t))] \\
&= f_3(t - 2\Delta t), \\
&\bar{V}_4(t) = JI_zS_z + JE\cos(\omega^-(4\Delta t - t)) - JG\sin(\omega^-(4\Delta t - t)) \\
&+ A[-I_x\cos(\omega_I(4\Delta t - t)) - I_y\sin(\omega_I(4\Delta t - t)) - \\
&S_x\cos(\omega_S(4\Delta t - t)) - S_y\sin(\omega_S(4\Delta t - t))] \\
&= f_3(4\Delta t - t).
\end{aligned}
\tag{3.54}
$$

For a time varying Hamiltonian $H(t)$, the average Hamiltonian between time 0 and

T in the first three orders are

$$\begin{aligned} H^{(0)} &= \frac{1}{T}\int_0^T dt H(t), \\ H^{(1)} &= \frac{-i}{2T}\int_0^T dt \int_0^t dt'[H(t), H(t')], \\ H^{(2)} &= \frac{-1}{6T}\int_0^T dt \int_0^t dt' \int_0^{t'} dt'' \\ &\quad \{[H(t), [H(t'), H(t'']] + [[H(t), H(t')], H(t'')].\} \end{aligned} \tag{3.55}$$

In order to evaluate the integrals, notice the following useful identities obtained by appropriate changes of variables

$$\begin{aligned} &\int_0^{\Delta t} f(t)dt = \int_{\Delta t}^{2\Delta t} f(2\Delta t - t)dt \\ &= \int_{2\Delta t}^{3\Delta t} f(t - 2\Delta t)dt = \int_{3\Delta t}^{4\Delta t} f(4\Delta t - t)dt. \end{aligned} \tag{3.56}$$

$$\begin{aligned} \int_0^{\Delta t} \bar{V}_1(t) \int_0^t \bar{V}_1(t')dt'dt &= \int_0^{\Delta t} f_1(\sigma) \int_0^{\sigma} f_1(\sigma')d\sigma'd\sigma, \\ \int_{\Delta t}^{2\Delta t} \bar{V}_2(t) \int_{\Delta t}^t \bar{V}_2(t')dt'dt &= \int_0^{\Delta t} f_1(\sigma) \int_{\sigma}^{\Delta t} f_1(\sigma')d\sigma'd\sigma, \\ \int_{2\Delta t}^{3\Delta t} \bar{V}_3(t) \int_{2\Delta t}^t \bar{V}_3(t')dt'dt &= \int_0^{\Delta t} f_3(\sigma) \int_0^{\sigma} f_3(\sigma')d\sigma'd\sigma, \\ \int_{3\Delta t}^{4\Delta t} \bar{V}_4(t) \int_{3\Delta t}^t \bar{V}_4(t')dt'dt &= \int_0^{\Delta t} f_3(\sigma) \int_{\sigma}^{\Delta t} f_3(\sigma')d\sigma'd\sigma. \end{aligned} \tag{3.57}$$

In addition, denote

$$\begin{aligned}\int_0^{\Delta t} f_1(t) &= F_1 = Q_1 + Q_2,\\ \int_0^{\Delta t} f_3(t) &= F_3 = Q_1 - Q_2,\end{aligned} \tag{3.58}$$

where Q_1 is equal to

$$\begin{aligned}&\int_0^{\Delta t} dt[JI_zS_z - A\sin(\omega_I t)I_y - A\sin(\omega_S t)S_y + J\cos(\omega^- t)E)]\\ &= \Delta t\left[JI_zS_z - \frac{\theta}{2}\mathrm{sinc}^2(\frac{\omega_I\Delta t}{2})\omega_I I_y - \right.\\ &\left.\frac{\theta}{2}\mathrm{sinc}^2\left(\frac{\omega_S\Delta t}{2}\right)\omega_S S_y + J\mathrm{sinc}(\omega^-\Delta t)(I_xS_x + I_yS_y)\right],\end{aligned} \tag{3.59}$$

and Q_2 is

$$\begin{aligned}&\int_0^{\Delta t} dt\left[JG\sin(\omega^- t) + A\cos(\omega_I t)I_x + A\cos(\omega_S t)S_x\right]\\ &= \mathrm{sinc}^2\left(\frac{\omega^-\Delta t}{2}\right)\frac{J\omega^-(\Delta t)^2}{2}(I_xS_y - I_yS_x)\\ &+ \theta\mathrm{sinc}(\omega_I\Delta t)I_x + \theta\mathrm{sinc}(\omega_S\Delta t)S_x.\end{aligned} \tag{3.60}$$

As before, in the expressions for Q_1, Q_2, and in what follows, $\theta = A\Delta t$.

The zeroth order term is

$$H^{(0)} = \frac{1}{4\Delta t}\int_0^{4\Delta t} dtH(t) = \frac{1}{4\Delta t}2(F_1 + F_3) = \frac{Q_1}{\Delta t}. \tag{3.61}$$

In order to calculate the first order term, let us have a closer look at an integral of this kind

$$\int_0^{4\Delta t} dt[\bar{V}(t), \int_0^t dt'\bar{V}(t')]. \tag{3.62}$$

The commutator consists of two terms, the first of which can be broken down as

$$\begin{aligned}
&\int_0^{\Delta t} \bar{V}_1(t) \int_0^{t} \bar{V}_1(t') + \int_{\Delta t}^{2\Delta t} \bar{V}_2(t) \left(\int_0^{\Delta t} \bar{V}_1(t') + \int_{\Delta t}^{t} \bar{V}_2(t') \right) \\
&+ \int_{2\Delta t}^{3\Delta t} \bar{V}_3(t) \left(\int_0^{\Delta t} \bar{V}_1(t') + \int_{\Delta t}^{2\Delta t} \bar{V}_2(t') + \int_{2\Delta t}^{t} \bar{V}_3(t') \right) + \\
&\int_{3\Delta t}^{4\Delta t} \bar{V}_4(t) \left(\int_0^{\Delta t} \bar{V}_1(t') + \int_{\Delta t}^{2\Delta t} \bar{V}_2(t') + \int_{2\Delta t}^{3\Delta t} \bar{V}_3(t') + \int_{3\Delta t}^{t} \bar{V}_4(t') \right).
\end{aligned} \tag{3.63}$$

where the integrals are over t' and t. This simplifies to $2(F_1^2 + F_3^2 + 2F_3F_1)$ according to Eq. (3.57).

The first order term can then be shown as equal to

$$\begin{aligned}
H^{(1)} &= \frac{-i}{8\Delta t}[2(F_1^2 + F_3^2 + 2F_3F_1) - 2(F_1^2 + F_3^2 + 2F_1F_3)] \\
&= \frac{-i}{8\Delta t} 4[F_3, F_1] = \frac{-i}{\Delta t}[Q_1, Q_2].
\end{aligned} \tag{3.64}$$

Substitute the explicit expressions for Q_1, Q_2 we have

$$\begin{aligned}
H^{(0)} &= JI_zS_z - \frac{\theta}{2}\mathrm{sinc}^2\left(\frac{\omega_I\Delta t}{2}\right)\omega_I I_y \\
&\quad - \frac{\theta}{2}\mathrm{sinc}^2\left(\frac{\omega_S\Delta t}{2}\right)\omega_S S_y + J\mathrm{sinc}(\omega^-\Delta t)(I_xS_x + I_yS_y),
\end{aligned} \tag{3.65}$$

$$\begin{aligned}
&H^{(1)} = J\theta\left(\mathrm{sinc}(\omega_I\Delta t)I_yS_z + \mathrm{sinc}(\omega_S\Delta t)I_zS_y\right) + \\
&\frac{\theta^2}{2}\left[\mathrm{sinc}^2\left(\frac{\omega_I\Delta t}{2}\right)\frac{\sin(\omega_I\Delta t)}{\Delta t}I_z + \mathrm{sinc}^2\left(\frac{\omega_S\Delta t}{2}\right)\frac{\sin(\omega_S\Delta t)}{\Delta t}S_z\right] \\
&+ \left(\frac{J^2\omega^-(\Delta t)^2}{2}\right)\mathrm{sinc}(\omega^-\Delta t)\sin^2(\frac{\omega^-\Delta t}{2})(I_z - S_z) + \\
&J\theta\mathrm{sinc}^2\left(\frac{\omega_I\Delta t}{2}\right)\mathrm{sinc}^2\left(\frac{\omega^-\Delta t}{2}\right)\frac{\omega^-\omega_I(\Delta t)^2}{4}I_zS_y \\
&- J\theta\mathrm{sinc}^2\left(\frac{\omega_S\Delta t}{2}\right)\mathrm{sinc}^2\left(\frac{\omega^-\Delta t}{2}\right)\frac{\omega^-\omega_S(\Delta t)^2}{4}I_yS_z.
\end{aligned} \tag{3.66}$$

Notice that the largest contribution of the Larmor frequencies now points in the y direction, so in the next order term, H^2, we only look for the strength of the yy coupling term. We first separate C_o the coupling due to the Ising coupling term in the original Hamiltonian.

$$\begin{aligned} C_o = & \frac{-1}{24\Delta t} JA^2[-48\text{sinc}(\omega_I\Delta t)\text{sinc}(\omega_S\Delta t)(\Delta t)^3 + \\ & 6\text{sinc}(\omega_I\Delta t)\text{sinc}^2\left(\frac{\omega_S\Delta t}{2}\right)(\Delta t)^3 + 6\text{sinc}(\omega_S\Delta t)\text{sinc}^2\left(\frac{\omega_I\Delta t}{2}\right)(\Delta t)^3 \\ & + \frac{12\Delta t}{\omega_S^2}(\text{sinc}(\omega_I\Delta t) - 1) + \frac{12\Delta t}{\omega_I^2}(\text{sinc}(\omega_S\Delta t) - 1) \\ & + \left(\frac{6\Delta t}{\omega_I^2} + \frac{6\Delta t}{\omega_S^2}\right)(1 - \text{sinc}(\omega^+\Delta t) + 1 - \text{sinc}(\omega^-\Delta t))]. \end{aligned} \tag{3.67}$$

Under the condition $\omega\Delta t \ll 1$, $\text{sinc}(\omega\Delta t) \approx 1$, for $\omega = \omega_I, \omega_S$, the main field in $H^{(0)}$ reduces to

$$-\frac{A\Delta t}{2}(\omega_I I_y + \omega_S S_y), \tag{3.68}$$

which is the linear scaling as in the Ising coupling case. In addition, C_o reduces to $\frac{4}{3}(A\Delta t)^2 J I_y S_y$, which is consistent with the result derived in Eq. (3.33).

The total yy coupling in $H^{(2)}$ is

$$\begin{aligned} H_{yy}^{(2)} = & C_0 - \frac{JA^2}{24\Delta t}[C_1(\omega_I, \omega_S, \Delta t) + C_1(\omega_S, \omega_I, \Delta t)] \\ & - \frac{J^3}{24\Delta t}[C_2(\omega_I, \omega_S, \Delta t) + C_2(\omega_S, \omega_I, \Delta t)], \end{aligned} \tag{3.69}$$

where C_1 and C_2 are terms that arise from the planar coupling $I_xS_x + I_yS_y$ Hamiltonian.

The explicit formulae for C_1 and C_2 are shown below. Let

$$\begin{aligned} f_1(x, y, z, \psi_x, \psi_y, \psi_z, T) = & \int_0^T dt_3 \cos(xt_3 + \psi_x) \\ & \int_0^T dt_2 \cos(yt_2 + \psi_y) \int_0^T dt_1 \cos(zt_1 + \psi_z). \end{aligned} \tag{3.70}$$

In the following integrals, the integrands are exactly those that appear in Eq. (3.70), so we choose to omit them

$$\begin{aligned}
f_2(x,y,z,\psi_x,\psi_y,\psi_z,T) &= \int_0^T \int_0^{t_3} \int_0^{t_2}, \\
f_3(x,y,z,\psi_x,\psi_y,\psi_z,T) &= \int_0^T \int_{t_3}^T \int_{t_2}^T, \\
f_4(x,y,z,\psi_x,\psi_y,\psi_z,T) &= \int_0^T \int_{t_3}^T \int_0^T, \\
f_5(x,y,z,\psi_x,\psi_y,\psi_z,T) &= \int_0^T \int_0^T \int_0^{t_2}, \\
f_6(x,y,z,\psi_x,\psi_y,\psi_z,T) &= \int_0^T \int_0^T \int_{t_2}^T .
\end{aligned} \tag{3.71}$$

In addition let

$$\begin{aligned}
A_1 &= -7f_1 + 2(f_2 + f_3 + f_4) + f_5 - f_6, \\
A_2 &= f_1 + 2(f_2 + f_3 + f_4) + f_5 - f_6, \\
A_3 &= 2(f_2 + f_3 + f_4 + f_5).
\end{aligned} \tag{3.72}$$

Denote $\omega^- = \omega_I - \omega_S$, we have

$$\begin{aligned}
C_1(\omega_I,\omega_S,\Delta t) = &-2A_1(\omega_I,\omega^-,\omega_I,0,0,0,\Delta t) - 2A_1(\omega_I,\omega_I,\omega^-,0,\frac{\pi}{2},-\frac{\pi}{2},\Delta t) \\
&- 2A_1(\omega^-,\omega_I,\omega_I,-\frac{\pi}{2},\frac{\pi}{2},0,\Delta t) + A_2(\omega_I,\omega^-,\omega_I,0,-\frac{\pi}{2},\frac{\pi}{2},\Delta t) \\
&A_2(\omega^-,\omega_I,\omega_I,-\frac{\pi}{2},0,\frac{\pi}{2},\Delta t) + A_2(\omega_I,\omega_I,\omega^-,0,0,0,\Delta t) \\
&+ A_3(\omega^-,\omega_I,\omega_I,0,0,0,\Delta t) + A_3(\omega_I,\omega_I,\omega^-,\frac{\pi}{2},0,-\frac{\pi}{2},\Delta t) \\
&+ A_3(\omega_I,\omega^-,\omega_I,\frac{\pi}{2},-\frac{\pi}{2},0,\Delta t).
\end{aligned} \tag{3.73}$$

$$\begin{aligned}
C_2(\omega_I,\omega_S,\Delta t) = &\, 4A_1(\omega^-,\omega^-,\omega^-,-\frac{\pi}{2},0,-\frac{\pi}{2},\Delta t) \\
&+ 2A_2(\omega^-,\omega^-,\omega^-,-\frac{\pi}{2},-\frac{\pi}{2},0,\Delta t) + 2A_3(\omega^-,\omega^-,\omega^-,0,-\frac{\pi}{2},-\frac{\pi}{2},\Delta t).
\end{aligned} \tag{3.74}$$

Since f_k, $k = 1, 2, \ldots, 6$ are upper bounded by $(\Delta t)^3$, C_1 and C_2 are on the order of $(\Delta t)^3$. $\theta = \Delta t A$ and $\Delta t J$ are both small parameters, therefore, the strength of the coupling in $H^{(2)}$ is on the order of $J\theta^2$, which is much smaller than the original coupling J. Simulations have been performed to confirm our calculations.

The total value of $I_x S_x + I_y S_y$ is

$$\frac{4J}{\omega^-} \sin(\omega^- \Delta t). \tag{3.75}$$

Hence, if ω^- is known with certainty, we can choose $\Delta t = \pi/\omega^-$ to eliminate $I_x S_x + I_y S_y$ in the first order. However, this knowledge is usually not available because of chemical shift dispersion. In the next section, we show how to compensate for this.

3.4.1 Compensation for unknown chemical shift difference

As was done in the case of the 6-segment pulse sequence, when the chemical shift difference has a dispersion, we eliminate the planar coupling term by concatenating several elementary control blocks shown in Fig. 3.1, each with a different value of Δt_i, $i = 1, 2, \ldots, m$.

Denote ω_o^- as the nominal frequency difference. The actual frequency difference, ω^-, is equal to $\omega^- = \omega_o^-(1 + \delta)$, where δ is in the range $[0,\ \Delta]$ with Δ given. The total planar coupling $I_x S_x + I_y S_y$ for each $\omega_o(\delta)$ is $4Jg(\delta)$, where

$$g(\delta) = \sum_{i=1}^{m} \frac{\sin((1+\delta)\omega_o^- \Delta t_i)}{(1+\delta)\omega_o^-}. \tag{3.76}$$

We need to find a set of parameters $\{\Delta t_i\}$, $i = 1, 2, \ldots, m$ such that $g(\delta)$ is close to zero for all δ in a desired range.

3.4.2 Scaling of the frequency offsets and rf amplitude modulation

With the concatenating blocks, and with a fixed value of rf amplitude, A, throughout the blocks, the scaled frequency offset is

$$\frac{\sum_{i=1}^{m} \mathrm{sinc}^2(\frac{\omega\Delta t_i}{2})(\frac{A\Delta t_i}{2})\omega 4\Delta t_i}{\sum_{i=1}^{m} 4\Delta t_i}. \tag{3.77}$$

This nonlinear relationship between the scaled and the original frequencies is rarely one to one. This makes it difficult to retrieve the chemical shifts without additional information. To circumvent this problem, we vary the rf amplitude over the concatenating blocks so that, over the range of frequencies of interest, there is a one-to-one mapping between the scaled and the original offsets. This is done by first obtaining Δt_i by minimizing g in Eq. (3.76), and then adjusting the value of A in each block. Now, denote A as the vector that contains the modulated rf amplitude. The new scaled frequency offset is equal to

$$\omega_{\mathrm{scaled}} = \frac{\sum_{i=1}^{m} \mathrm{sinc}^2(\frac{\omega\Delta t_i}{2})(\frac{A(i)\Delta t_i}{2})\omega 4\Delta t_i}{\sum_{i=1}^{m} 4\Delta t_i}. \tag{3.78}$$

Higher rf amplitudes lead to higher scaled frequencies. However, the highest frequency that can be captured is limited by how fast we can sample. For simplicity, here we choose to sample uniformly at the end of each compensating cycle, i.e. after each interval of $4\sum_{i=1}^{m} \Delta t_i$. However, it is worth noting that nonuniform sampling after each compensating block $4\Delta t_i$ has the potential to capture higher frequencies. This would allow the use of higher rf amplitudes, leading to higher scaled frequencies, and eventually the ability to decouple systems that have higher coupling strength.

3.4.3 Simulation results

We run simulations for a system that has $\omega^-/(2\pi)$ in the range $[1, 1.5]$ kHz. First, we find a set of $\{\Delta t_i\}$ that minimizes $g(\delta)$ in Eq. (3.76) for $\omega_o^-/(2\pi) = 1$ kHz and δ in the range $[0,\ 0.5]$. The optimization yields the following set of times $\{\Delta t_i\} = \{0.1650,\ 0.5309,\ 0.4900,\ 0.8739\}$ ms. With these values of $\{\Delta t_i\}$, we manually adjust the values of A such that the frequency scaling curve has a nice linear region. A good choice for A is $A/(2\pi) = [200,\ 100,\ 120,\ 60]$ Hz. This is roughly equivalent to keeping $A(i)\Delta t_i$ a constant. Figure 3.8 shows the scaling of the frequency offsets for the set of parameters found.

It should be noted that our design is most effective when the actual frequencies fall in a linear range of the frequency scaling curve. However, the design is able to decouple systems with higher coupling strength compared to the previous case for the same chemical shift difference because it does not enhance the zz coupling.

Figure 3.9 shows simulation results for a range of frequency offsets $\omega^- = [1, 1.5]$ kHz.

3.5 Discussion of experimental issues

The pulse sequences described successfully decouple a coupled two spin $\frac{1}{2}$ system with isotropic scalar coupling. The design uses relatively low rf amplitude, and most importantly, the rf irradiation is non-selective, which is a major challenge in *isotropic scalar* coupling. The paper primarily presents the theory behind the design of such pulse sequences. In this section, we address some of the experimental issues.

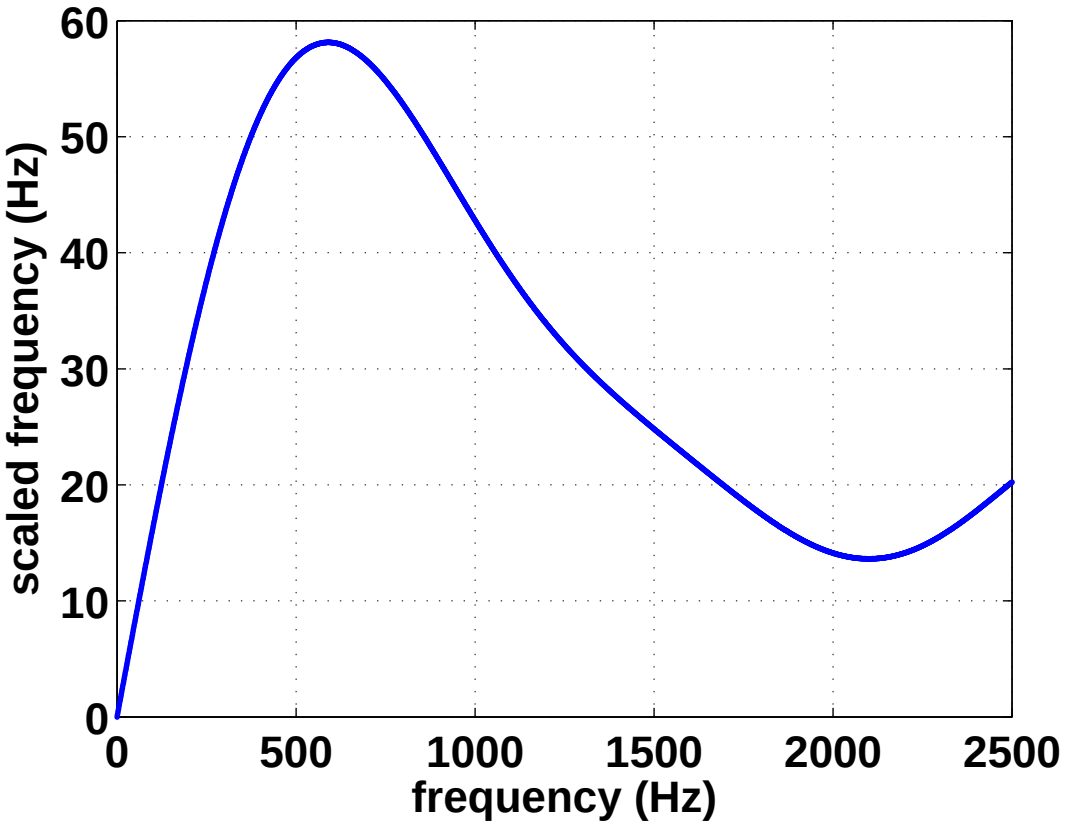

Figure 3.8: Nonlinear scaling of the frequency offsets under modulation of Δt and rf amplitudes. The horizontal axis shows $\omega/(2\pi)$, the vertical axis shows $\omega_{\text{scaled}}/(2\pi)$ according to Eq. (3.78). For this plot, $\Delta t = [0.1650,\ 0.5309,\ 0.4900,\ 0.8739]$ ms, $A/(2\pi) = [200,\ 100,\ 120,\ 60]$ Hz.

The sequences are well suited in 2D NMR. An ideal setting is to transfer the spin coherence after it has acquired a phase under chemical shift evolution to a coupled spin for readout, as in the indirect evolution periods in multi-dimensional NMR. This does not require windows of free evolution in the pulse sequence for measurement. Measurement in direct dimension, however, can be done by adding periods of non rf irradiation as shown in Fig. 3.1.

Another point we wish to discuss is the ideal π pulses used in the simulations. For

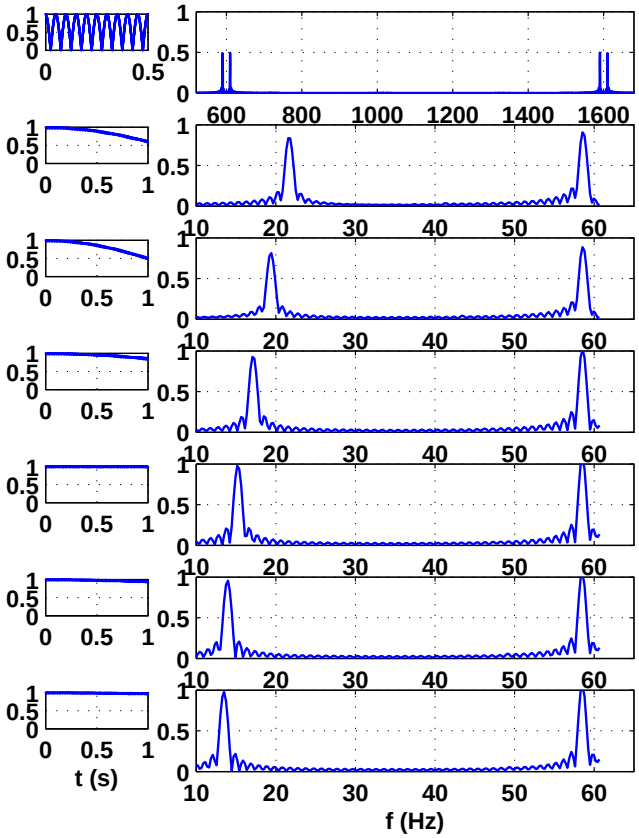

Figure 3.9: The first row shows the signal and spectrum of a coupled system that has chemical shift difference equal to 1 kHz and frequency offsets located at 0.6 and 1.6 kHz. The spectrum consists of two doublets each with 2 peaks separated by the coupling strength. The remaining rows show the results due to decoupling for a system that has frequency offsets $\omega_I/(2\pi) = 0.6$ kHz, $\omega_S/(2\pi) = [1.6,\ 1.7,\ 1.8,\ 1.9,\ 2.0,\ 2.1]$ kHz. The first column plots $\sqrt{\langle I_x\rangle^2 + \langle I_y\rangle^2 + \langle I_z\rangle^2}$, and the second column plots the Fourier transform of the FID signal $\langle I_x + S_x\rangle$. The designed parameters are $\Delta t = [0.1650,\ 0.5309,\ 0.4900,\ 0.8739]$ ms, $A/(2\pi) = [200,\ 100,\ 120,\ 60]$ Hz. All π pulses are ideal δ pulses. In all cases , $J/(2\pi) = 20$ Hz, which is twice as big as the coupling in the 6-segment pulse sequence case. The results show the robustness of our pulse sequence over the dispersion of the chemical shift difference.

applications where peak power is not a constraint, the pulse sequences are readily usable. For applications where power is limited, suitable phase cycling can be employed

to mitigate the effects that finite power inversion pulses have on decoupling. So far, we have assumed that the π pulses are instantaneous pulses for easier analysis of the decoupling sequences. In practice, however, the π pulses as depicted in Fig. 3.6 have maximum amplitude A_m and finite duration π/A_m. During this finite duration, the system's Hamiltonian still evolves leading to reduced performance of our decoupling sequence. We can mitigate this problem by inverting the phase of the rf. pulses. The Hamiltonians for practical π pulses are:

$$H_\pi^\pm = \omega_I I_z + \omega_S S_z + J(I_x S_x + I_y S_y + I_z S_z) \pm A_m(I_x + S_x) \tag{3.79}$$

Specifically, in the first cycle, we use H_π^+ and H_π^- and in the second cycle, we use H_π^- and H_π^+. For the parameters indicated Fig. 3.7, $A_m = 40$ produces results that are comparable with the results obtained using instanteneous pulses provided that the chemical shift difference must be known. When the chemical shift difference is unknown and a compensation cycle needs to be used, A_m needs to be higher, around 100 kHz.

Finally, the decoupling sequences scale down the frequency offsets. This obviously degrades the resolution, but because we can decouple effectively, we can make spins precess for longer periods and restore resolution. Since the frequency offsets are scaled down by a factor that involves the strength of the applied rf field, in the presence of rf inhomogeneity, the observed spectrum is blurred by the point spread function $\chi(f)$. The observed spectrum is therefore

$$Z(f) = \sum_i X(f_i)\chi(f - f_i) + N(f) \tag{3.80}$$

where the true spectrum is comprised of spikes at f_i. $N(f)$ is the noise spectrum. We wish to deconvolve the observed spectrum $Z(f)$ to recover $X(f_i)$. To do this, first

calibrate $\chi(f)$ from an isolated peak. $\chi(f)$ reflects the inhomogeneity of the sample. We can then deconvolve using techniques such as the least square estimation.

3.6 Conclusion and outlook

In conclusion, we have introduced two new pulse sequences to decouple homonuclear spins with isotropic scalar coupling in liquid-state NMR. The pulse sequences successfully collapsed doublets into singlets with higher peak intensities. The original chemical shifts can be read off from the observed spectrum. This was done by first eliminating the planar coupling term $I_xS_x + I_yS_y$, and creating an effective field pointing in the y direction to effectively cancel the coupling in the z direction I_zS_z. As a result of the sequences, the frequency offsets were scaled down by a factor depending on the rf amplitudes and durations. The effective coupling was scaled down faster than the frequency offsets. We laid the detailed analysis and methods to design the parameters for the pulses, and presented numerical examples. In an actual implementation, care has to be taken in choosing the right parameters.

The main advantages of the decoupling sequences are that the pulses are non-selective, having low rf power, and they work for a range of coupling strength and chemical shifts. While very weak irradiation can selectively invert one spin, precise chemical shifts need to be known ahead of time. In our scheme, this information is not necessary, making it useful in exploring new molecules.

The pulses have limitations. The chemical shifts are scaled down. Numerical optimization is required for a specific system. The scaling factor of the frequency offsets depends on the rf amplitude, which is not homogeneous throughout the sample.

We discuss how to circumvent this and some other experimental issues in Sec. 3.5.

Solving for the strong coupling case is a desirable extension of the current work.

Chapter 4

Reducing coupling between quantum bits using global pulses

4.1 Introduction

Decoherence is one of the biggest obstacles in quantum information processing (QIP) since random phase errors reduce the fidelity of a quantum operation [36]. Maintaining coherence is therefore a very important aspect in realization of a quantum computer. It turns out that many techniques developed in NMR can find immediate applications in quantum computing. Here, we will apply the decoupling sequence developed in chapter 3 to show how to extend the coherence time of a quantum system that has Ising type coupling among the qubits.

There are different mechanisms that lead to decoherence in QIP systems. In liquid state NMR, which is used as a test bed for many quantum algorithms [12], spin-spin coupling among the nuclei is mainly responsible for the transverse relaxation

T_2 [37]. In solid state systems such as an NV center, the coupling between the electron spin of the NV center and the surrounding spin bath of ^{13}C nuclei is the dominant dephasing mechanism [38]. In superconducting qubits, the origin of decoherence has been shown to involve the coupling between the flux qubits and a microscopic two-level system [39, 40, 41, 42].

Decoupling therefore will help prolong coherence in these systems. Various decoupling techniques have been proposed and experimentally realized. Randomized dynamical decoupling [43] uses randomly selected pulses at regular intervals. Uhrig dynamical decoupling [44] consists of an optimized CPMG sequence that has varying interval between the application of the π pulses. Several extensions of this decoupling scheme have been reported [45, 46, 47, 48] together with its implementation in ion traps [49, 50]. In fact, many decoupling schemes rely on the refocusing π pulse first developed in NMR for decoupling purposes in QIP [51, 16, 15].

A common feature of these decoupling schemes is that they assume selective controls on the system. However, for many quantum systems, selective addressing of each qubit could be very challenging. In addition, selective pulses increase the complexity of a system. For example, in Ref. [52] it is shown that the number of selective pulses needed to decouple a system with two-body couplings grows linearly with the number of qubits. Here, we examine the use of global pulse sequences to decouple the Ising interaction between the qubit spins as well as the coupling between the system and the environment. The advantage of global pulses is that the number of pulses needed for decoupling will be independent of the number of qubits, i.e. the complexity of the pulses is $O(1)$.

Consider the general Hamiltonian of a quantum system denoted S coupled to a heat bath denoted as H [53]

$$H = H_S + H_B + H_{SB} \tag{4.1}$$

A global pulse transforms an initial Hamiltonian H_o to

$$H_i = (U \otimes U \otimes \cdots \otimes U)^\dagger H_o U \otimes U \otimes \cdots \otimes U,$$

where U represents the propagator generated by the global pulse on each single qubit. Global pulses can be used to decouple systems with special symmetries such as dipole-dipole coupling. In this case, the coupling Hamiltonian takes the following form

$$H_1^{dd} = \sum_{jk} d^{jk}(2I_{jz}I_{kz} - I_{jx}I_{kx} - I_{jy}I_{ky}), \tag{4.2}$$

in which $I_{\ell\nu}$ denotes the operator that acts as I_ν, $\nu = x, y, z$ on the ℓth spin.

Applying global $\frac{\pi}{2}_x$ pulse and $\frac{\pi}{2}_y$ pulse on the system, one gets

$$\begin{aligned} H_2^{dd} &= \sum_{jk} d^{jk}(2I_{jy}I_{ky} - I_{jx}I_{kx} - I_{jz}I_{kz}), \\ H_3^{dd} &= \sum_{jk} d^{jk}(2I_{jx}I_{kx} - I_{jz}I_{kz} - I_{jy}I_{ky}). \end{aligned} \tag{4.3}$$

It is easy to see that averaging these three Hamiltonians decouples the dipole-dipole coupling:

$$e^{-iH_1^{dd}\delta t}e^{-iH_2^{dd}\delta t}e^{-iH_3^{dd}\delta t} = e^{-i\bar{H}3\delta t},$$

where $\bar{H} = 0$. This is the basic building block of WAHUHA [54], and MREV sequences such as MREV-16 [55], whose effectiveness of for decoupling dipole-dipole interaction has been experimentally demonstrated [56]. Such decoupling schemes, however, cannot be generalized to systems with Ising coupling.

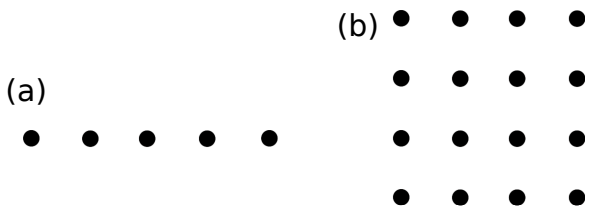

Figure 4.1: Spin topology: (a) Linear Chain (b) Square Lattice

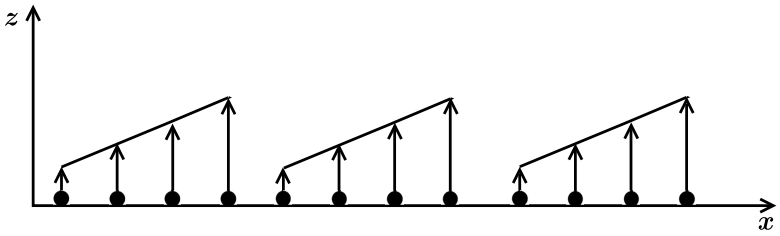

Figure 4.2: Periodic gradient magnetic field on a spin chain.

4.2 Reducing decoherence with global pulses

Consider a quantum register with N qubits which has two-body couplings among the qubits. The coupling topology can take various shapes, for example, it can be a spin chain or square lattice as in Fig. 4.1.

A gradient magnetic field is added upon the system which causes the Zeeman splitting on the qubits. The magnetic field and its gradient is made big enough such that the difference of Zeeman splitting between coupled qubits is much larger than the coupling strength between the qubits. In a long spin chain, the gradient field is made periodic as shown in Fig. 4.2.

Under such gradient magnetic field, the Hamiltonian of the system takes the form

$$H = \sum_{j=1}^{N} \omega_j I_{jz} + \sum_{(jk)\in G} J_{jk} I_{jz} I_{kz} \tag{4.4}$$

where $\omega_j = -\vec{\mu} \cdot \vec{B_j}$, $\vec{\mu}$ is the magnetic moment and B_j indicates the magnetic field at site j. G is a graph indicating the coupling topology of the system, i.e., if the edge $(jk) \in G$, then the qubits at site j and k are coupled. We assume $\omega_i >> J_{jk}$, $|\omega_j - \omega_k| >> J_{jk}, \forall i, j, k$.

We will first use a two-qubit system to illustrate the decoupling strategy, then generalize it to N qubits.

For a system of two qubits denoted I and S coupled via J coupling, the Hamiltonian is

$$H_0 = \omega_I I_z + \omega_S S_z + J I_z S_z. \tag{4.5}$$

Consider the effect of the following pulse sequence

$$\begin{aligned} H_1 &= \omega_I I_z + \omega_S S_z + J I_z S_z + A(I_x + S_x) \\ H_2 &= -\omega_I I_z - \omega_S S_z + J I_z S_z + A(I_x + S_x) \\ H_3 &= -\omega_I I_z - \omega_S S_z + J I_z S_z - A(I_x + S_x) \\ H_4 &= \omega_I I_z + \omega_S S_z + J I_z S_z - A(I_x + S_x) \end{aligned} \tag{4.6}$$

where H_1 is obtained simply by applying a magnetic field in the x direction with effective amplitude A, H_2 is obtained from H_1 by conjugating a π pulse along the x direction, i.e., $H_2 = e^{-i\pi(I_x+S_x)} H_1 e^{-i\pi(I_x+S_x)}$. H_4 and H_3 are obtained similarly with a control field along the $-x$ direction. Each Hamiltonian is maintained for a period of Δt. The π pulses here are assumed to be infinitely narrow pulses.

Using the average Hamiltonian theory and keeping terms up to the second order, we obtain the following average Hamiltonian over an interval of $4\Delta t$

$$\begin{aligned} H_{1eff} &= JI_zS_z + \frac{A\Delta t}{2}(\omega_I I_y + \omega_S S_y) + A\Delta t J(I_yS_z + I_zS_y) \\ &- \frac{(A\Delta t)^2}{2}(\omega_I I_z + \omega_S S_z) + \frac{4}{3}(A\Delta t)^2 J(I_yS_y - I_zS_z) + O((A\Delta t)^3) \end{aligned} \tag{4.7}$$

Denote $\theta = \Delta t A$ and choose Δt such that $\theta << 1$. The coupling along the J direction and the newly created Zeeman term in the y direction are the most important terms in H_{1eff}. Let us first look at these terms

$$H_1 = \frac{\theta}{2}(\omega_I I_y + \omega_S S_y) + JI_zS_z. \tag{4.8}$$

By applying a π_x rotation on H_1 we obtain

$$H_2 = -\frac{\theta}{2}(\omega_I I_y + \omega_S S_y) + JI_zS_z \tag{4.9}$$

Now consider the combined effect of raising H_1 and H_2 to some order k. The resulting unitary operator is

$$U = (U_1)^k(U_2)^k = e^{-iH_1 4\Delta tk}e^{-iH_2 4\Delta tk} \tag{4.10}$$

In the interaction frame of $\frac{\theta}{2}(\omega_I I_y + \omega_S S_y)$ for time $k4\Delta t$, and then $-\frac{\theta}{2}(\omega_I I_y + \omega_S S_y)$ for another period of $4k\Delta t$, the J coupling term becomes

$$J[I_z(\cos(2\theta kt\omega_I) + I_x(\sin(2\theta kt\omega_I)][S_z(\cos(2\theta kt\omega_S) + S_x(\sin(2\theta ktt\omega_S)]. \tag{4.11}$$

The coupling will be bounded from above by

$$\frac{1}{2\theta|\omega_I - \omega_S|k4\Delta t}J \tag{4.12}$$

For large enough k, the coupling is eliminated and U is approximately equal to identity, which is our goal.

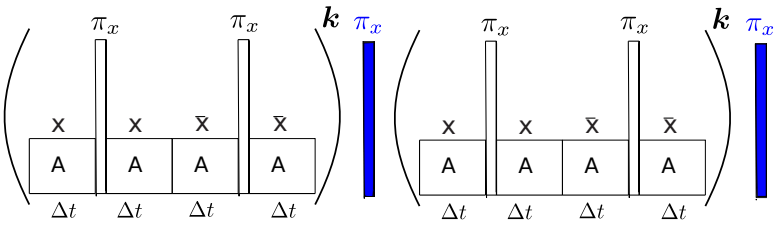

Figure 4.3: Pulse sequence for decoupling.

Notice that

$$\begin{aligned} U_2^k &= (e^{-i\pi(I_x+Sx)}e^{-iH_1 4\Delta t}e^{i\pi(I_x+Sx)})^k \\ &= e^{-i\pi(I_x+Sx)}(e^{-iH_1 4\Delta t})^k e^{i\pi(I_x+Sx)} \end{aligned} \tag{4.13}$$

so the pulse sequence can be implemented as shown in Fig. 4.3.

This decoupling strategy can be generalized to N qubits with nearest neighbors coupling. The Hamiltonian of the two-qubit system for the basic sequence in (4.6) is generalized for N qubits

$$\begin{aligned} H_1 &= \sum_{j=1}^{N}\omega_j I_{jz} + \sum_{(jk)\in G} J_{jk}I_{jz}I_{kz} + \sum_{j}^{N} AI_{jx}, \\ H_2 &= -\sum_{j=1}^{N}\omega_j I_{jz} + \sum_{(jk)\in G} J_{jk}I_{jz}I_{kz} + \sum_{j}^{N} AI_{jx}, \\ H_3 &= -\sum_{j=1}^{N}\omega_j I_{jz} + \sum_{(jk)\in G} J_{jk}I_{jz}I_{kz} - \sum_{j}^{N} AI_{jx}, \\ H_4 &= \sum_{j=1}^{N}\omega_j I_{jz} + \sum_{(jk)\in G} J_{jk}I_{jz}I_{kz} - \sum_{j}^{N} AI_{jx}, \end{aligned} \tag{4.14}$$

One way to see why this generalization works is to partition the Hamiltonians into

pairs of coupled spins. For the case of 4 spins we can partition the Hamiltonians into

$$\begin{aligned} H_1 &= H_{12}^1 + H_{23}^1 + H_{34}^1 + H_{41}^1, \\ H_2 &= H_{12}^2 + H_{23}^2 + H_{34}^2 + H_{41}^2, \\ H_3 &= H_{12}^3 + H_{23}^3 + H_{34}^3 + H_{41}^3, \\ H_4 &= H_{12}^4 + H_{23}^4 + H_{34}^4 + H_{41}^4. \end{aligned} \tag{4.15}$$

The subscrip jk denotes the coupling between spin j and k. In particular,

$$\begin{aligned} H_{12}^1 &= \frac{\omega_1}{2} I_{1z} + \frac{\omega_2}{2} I_{2z} + J_{12} I_{1z} I_{2z} + \frac{A}{2}(I_{1x} + I_{2x}) \\ H_{23}^2 &= -\frac{\omega_2}{2} I_{2z} - \frac{\omega_3}{2} I_{3z} + J_{23} I_{2z} I_{3z} + \frac{A}{2}(I_{2x} + I_{3x}) \\ &\vdots \end{aligned} \tag{4.16}$$

Here we partition the strength of the Larmor term for each spin equally between the Hamiltonians with the assumption that the strengths of the J coupling do not vary much between pairs of spins. Let us look at a 'cross' term that is the commutator between H_{12}^1 and H_{23}^1.

$$[H_{12}^1, H_{23}^2] = (\Delta t)^2 i \frac{JA}{2}(I_{1z} I_{2y} - I_{2y} I_{3z}). \tag{4.17}$$

With a small enough value for Δt, this commutator can be approximated as zero. Hence, the main contributions to the commutator between H_1 and H_2 come from the following commutators $[H_{12}^1, H_{12}^2]$, $[H_{23}^1, H_{23}^2]$, $[H_{34}^1, H_{34}^2]$, and $[H_{41}^1, H_{41}^2]$, i.e. commutators between the same pairs of spins. The calculation of H_{eff} for multiple spins is therefore very similar to the calculation for two spins.

Decoherence of a quantum system is the result of the coupling with the environment. Our decoupling scheme can reduce decoherence in certain cases. One case is when the effect of the environment is manifest in small random fluctuations over time

in the coupling strengths J_{jk}. This, to a large extent, does not effect our results since at every step in our analysis, the precise knowledge of the coupling is not needed, only its relative size compared to the difference in the strength of the Zeeman splittings.

Another case in which decoherence can be mitigated is when the coupling with the environment is a purely dephasing mechanism. The coupling Hamiltonian can be modeled as

$$H_{SB} = \sum \hbar\sigma_z(g_k b_k^\dagger + g_k^\dagger b_k), \tag{4.18}$$

where $b_k^\dagger$ and b_k are bosonic operators for the k^{th} field mode of the environment, characterized by a generally complex coupling parameter. Our decoupling scheme with the use of the π pulses also averages out the net effect of H_{SB},

Finally, we present a numerical simulation. Fig. 4.4 illustrate the effects of our decoupling strategy. The vertical axis represents the fidelity of U with respect to the identity operator, where fidelity measurement between two unitary operators U_1 and U_2 is defined as

$$\phi = \frac{|tr(U_1 U_2^\dagger)|^2}{|tr(U_2 U_2^\dagger)||tr(U_1 U_1^\dagger)|)}; \tag{4.19}$$

The simulation was done on a square lattice with one iteration of the pulses. The coupling strengths between adjacent qubits follow independent normal distributions with mean values $J = [10, 12.1, 11.4, 9.2]$ Hz and variance equal to the square of the mean of mean values $\bar{J} = 10.7$ Hz. The Zeeman splitting caused by the gradient magnetic field is 17.29kHz, 32.35kHz, 10kHz, 32.4kHz respectively, Δt is taken to be 10^{-7}s and $A \approx 8$kHz, $\theta = \frac{1}{20}$. It can be seen that the global pulses reduce the decoherence rate by about two orders of magnitude. The results are almost identical to the case where the coupling strengths are constant, confirming our conclusion

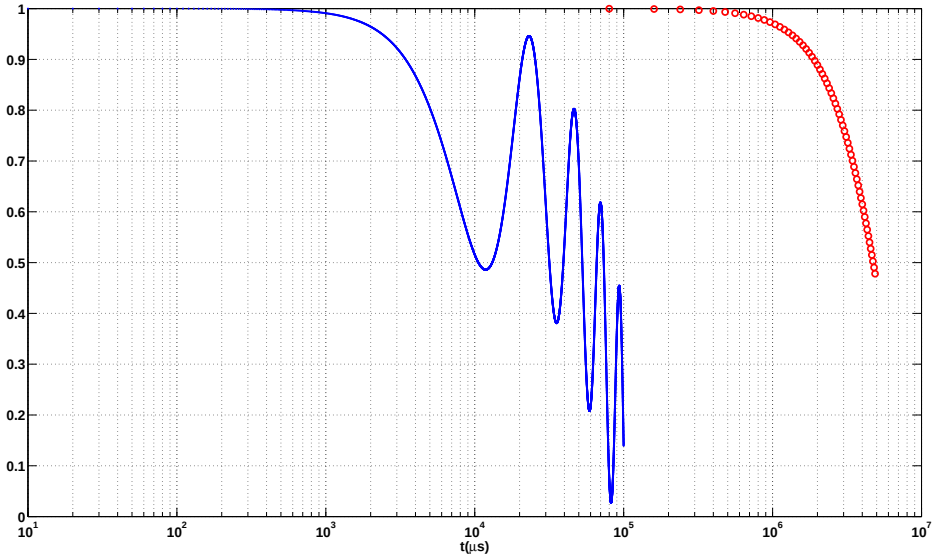

Figure 4.4: he simulation was on a square lattice with four qubits, the coupling strengths of four edges of this lattice follow independent normal distributions with mean values $2\pi[10, 12.1, 11.4, 9.2]$ and variance equal to the square of mean of the mean values $\bar{J} = 10.7$ Hz. The Zeeman splitting caused by the gradient field is $2\pi 10^4[1.729, 3.235, 1.0, 3.24]$ respectively, $\Delta t = 10^{-7}$, $\theta = \frac{1}{20}$, $A \approx 2\pi 8 \times 10^3 = 8kHz$. The blue line shows the fidelity without the decoupling pulses, the red circles show the fidelity with the application of the decoupling pulses.

about the robustness of the decoupling sequence against fluctuations of the coupling strengths. Without the application of the decoupling sequence, the fidelity shows unpredictable behavior after it reaches zero so we do not show the data on the plot.

In conclusion, we have shown the effectiveness of our pulse sequence, which is a global pulse, in reducing the coupling strength of register qubits. This can be used to reduce the residual coupling of quantum memories, where selective addressing may be hard or undesirable. The building block constructed here can be symmetrized to incorporate inhomogeneities of magnetic field, similarly to how MLEV-16 was constructed to decouple the dipole-dipole coupling. Other extensions on decoupling

using global pulses can also be made along this approach.

Chapter 5

New refocusing and excitation pulses for the CPMG sequence

5.1 NMR well logging

Well logging is a technique in which sensors lowered down in a bore hole are used to measure properties of earth formations. NMR along with mechanical, electromagnetic, acoustic, and nuclear sensors are routinely used in well logging for the evaluation of hydrocarbon reservoirs [10]. Although NMR was not used in the oil fields until much later, the research on NMR for well logging started as early as 1948. With the development of logging tools, especially the invention of the inside-out configuration of a strong permanent magnet [57], and the improvement of measurement techniques, NMR became a successful commercial tool for well logging starting in the 1980s. From the measured relaxation time, diffusion constant, and other parameters, a great deal of information about the formation being explored can be obtained. This

includes, but not limited to, porosity (the fraction of fluid in the rock), the types of fluids (brine or hydrocarbon, light or heavy oils), pore size distribution, and fluid properties such as viscosity, permeability, etc. [9, 10].

Let us look at a particular example of how NMR data are used in characterizing physical properties of a fluid. The T_2 distribution has a close relationship to many parameters that characterize the formation. In a water-saturated rock, the larger T_2 is the larger the pore size is. Bigger pores contain free water, middle-size pores contain capillary-bound water, and smaller pores contain clay-bound water. In addition, T_2 is approximately proportional to molecular weight, so it can be used to qualitatively characterize heavy and light oil [58].

Relaxation and diffusion constants are two of the most frequently measured quantities in NMR well logging. Both quantities can be measured using the CPMG sequence [59]. Our goal in this chapter is to design refocusing and excitation pulses that improve SNR in highly inhomogeneous field, i.e., when the dispersion in the Larmor offsets is much bigger than the amplitude of the rf. irradiation. This is often the case in NMR well logging.

5.2 CPMG sequence

The Carr-Purcell-Meiboom-Gill (CPMG) sequence is one of the most important sequences used to generate spin echoes. It was first developed by Carr and Purcell [60] and later was modified by Meiboom and Gill [61] both in the 1950s. Despite its long history, the sequence is still used today in a variety of applications ranging from magnetometry[62], quantum information processing [15] to well logging [63].

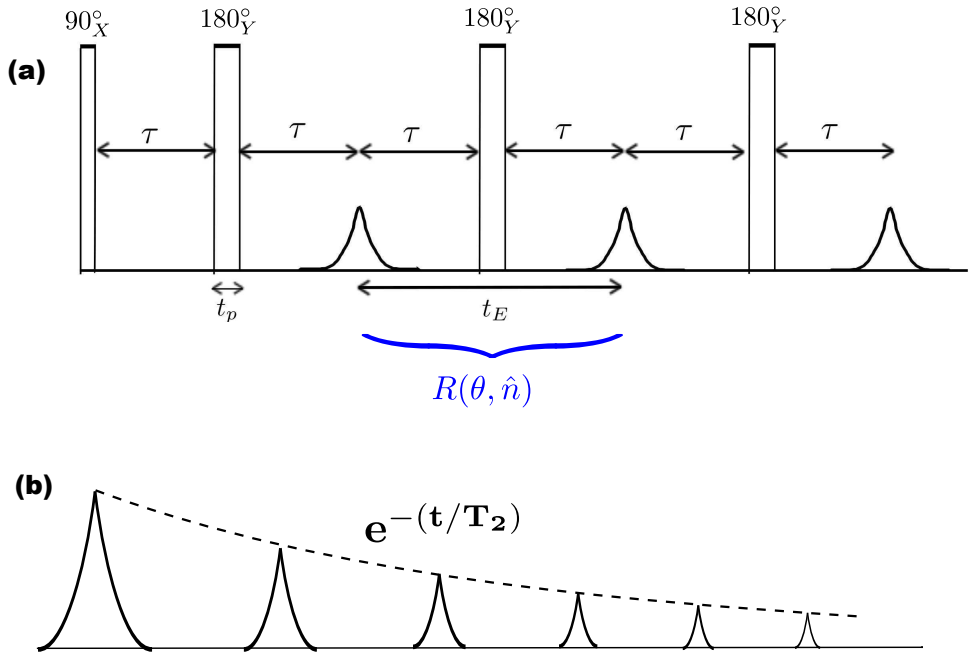

Figure 5.1: (a) Illustration of the CPMG sequence. t_E is the echo spacing. t_p is the length of the refocusing pulse. For a rectangular pulse, $t_p = \frac{1}{2A}$, where A is the rf. amplitude measured in Hz. τ indicates a free precession period.(b) The echo peaks decay exponentially with time constant T_2 caused by the spin-spin relaxation.

The CPMG sequence consists of an initial excitation pulse 90°_X that brings the longitudinal magnetization to the transverse plane, and a train of 180° pulses that are equally spaced and phase shifted by 90° compared to the excitation pulse, i.e. 180°_Y in this case. A schematic illustration of the CPMG sequence is shown in Fig. 5.1(a).

After the initial excitation pulses, all spins are aligned along the y direction. During the first free precession period, spin isochromats of slightly different precession frequencies move with different speed and therefore are separated from one another. The 180° pulse flips them along the y axis making the faster one closer to the start line and the slower ones further away from the start line, hence after the second free precession period equal in length to the first one, all isochromats are brought back to

the same point creating an echo. This process is repeated many times giving rise to a train of echoes. The refocusing pulses which are 90° phase shifted to the excitation pulse have an additional advantage. This phase shift makes the sequence more robust against pulse length errors because the errors do not accumulate from one echo to the next.

While the refocusing pulses in the CPMG sequence correct for the dephasing of the isochoromats due to field inhomogeneity, they do not correct for the decoherence due to spin-spin interaction. The echo peaks do not maintain a constant height but instead experience an exponential decay as shown in Fig. 5.1(b). The time constant of this decay is the spin-spin relaxation constant T_2.

Ideally, the pulses are instantaneous pulses that have infinite excitation and refocusing bandwidths (BW). In practice, however, the rf. amplitudes are always limited due to various constraints imposed on the system. The effective bandwidth for a pulse of finite amplitude is approximately its amplitude. In very inhomogeneous field, this places a severe limit on the number of spins that can be excited or refocused, thereby limiting the signal-to-noise ratio (SNR). We will refer to a constant amplitude pulse as a rectangular pulse, for example a rectangular 180° pulse of amplitude A Hz would have duration $\frac{1}{2A}$ s. Currently, rectangular pulses are still the standard in most well logging tools. Our goal here is to design excitation and refocusing pulses that replace the rectangular 90° and 180° pulses to significantly improve the SNR in very inhomogeneous fields. We impose an upper limit on the rf. amplitude in the design of the pulses, as often the case in well logging and many other NMR applications.

5.3 Challenges in improving signal-to-noise ratio

In most measurements, a high SNR is always desirable. It is even more so in well logging. The logging tools have to penetrate a depth exceeding 10 kilometers underground under harsh conditions (high temperature up to 175° C, high pressure around 140 MPa) [9, 10]. This makes drilling and the operation in the bore hole extremely costly. Measurements can be taken while drilling in the so-called logging while drilling technique, or taken after a drill has been completed. In either cases, increasing the SNR by not increasing the measurement time and power will be attractive and beneficial.

NMR in the context of well logging is markedly different from that in high field NMR spectroscopy or MRI. The sample to be probed is outside the magnet resulting in grossly inhomogeneous Larmor frequency offsets. The magnet used in the borehole is a permanent magnet whose field usually does not exceeds 500 G. Nevertheless, the inhomogeneity in the Larmor frequency offsets is still at least an order of magnitude larger than the rf. amplitude. The only compensation for all the harsh conditions we have to deal with is that the sample here, which is the volume of the earth formation under the irradiation of the magnetic field, is large. Effectively, we have an infinite-bandwidth sample at our disposal. Since the goal is to improve SNR, it it not essential to completely excite and refocus *all* spins in a given bandwidth but rather excite and refocus spins in *as large a bandwidth* as possible.

Another important point in our problem is that the pulses should have short durations. Since the relaxation times can be from sub-milliseconds to several seconds, the echo spacing should be kept short in order to capture a wide range of relaxation

times. Short pulses also result in a large number of echoes, which can go up to several thousand per measurement. Averaging adjacent echoes is another way to improve the SNR. Since the refocusing pulse is to be repeated many times, it is essential to keep this pulse short. Surprisingly, we were able to find refocusing pulses as short as the rectangular π pulse that have the potential to triple the SNR.

We will first describe the spin dynamics in grossly homogeneous fields, outline the method used to look for the pulses, and finally present the findings of the refocusing pulses and the excitation pulses.

5.4 Spin dynamics in inhomogeneous fields

The Hamiltonian for a system of spins in the rotating frame consists of the natural Hamiltonian and the rf. Hamiltonian

$$\begin{aligned} H(t) &= \Delta\omega_o I_z + \omega_1(t)(\cos(\phi(t))I_x + \sin(\phi(t))I_y) \\ &= \Delta\omega_o I_z + u(t)I_x + v(t)I_y. \end{aligned} \tag{5.1}$$

where $\omega_1(t) = \gamma B_1(t)$ is the rf amplitude, $\Delta\omega_o$ is the Larmor offsets. The rf. pulse can be specified by its amplitude $\omega_1(t)$ and phase $\phi(t)$ or by its x and y components: $u(t)$ and $v(t)$. Coupling can be ignored in this case so the Bloch equation is conveniently used to describe the evolution of the magnetization. Relaxation will be taken into account at the last step by multiplying the signal by a decaying exponential.

This Hamiltonian can be used to advance the spin ensembles in time by brute force calculation. However, when the Larmor field is inhomogeneous enough, the calculation can be greatly simplified. In this case, the echoes go through some transient states and quickly approach an asymptotic form. The decay in the observed echo

amplitude is purely due to relaxation. Below we summarize the spin dynamics that was discussed in detail in Ref. [64].

Let $\vec{M}(0^+)(\Delta\omega_o, \omega_1)$ be the magnetization after the initial excitation pulse. Denote $\hat{n}(\Delta\omega_0, \omega_1)$ the axis and $\theta(\Delta\omega_0, \omega_1)$the angle of the effective rotation that describes the evolution from one echo to the next. This evolution consists of two periods of free precession sandwiched by a period of evolution under the effect of the refocusing pulse denoted as the rotation $R(\theta, \hat{n})$ shown in Fig. 5.1(a). Note that the analysis here is complete general and is independent of the exact implementation of the 180°_Y pulse. It is also important to note that here we assume the echo spacing t_E is much shorter compared to T_2 and is short enough such that diffusion is negligible. We will omit the decay rate e^{-t/T_2} until the final result.

To facilitate the analysis, we break the the initial magnetization into two components, one parallel to the axis of rotation, and one perpendicular to the axis of rotation in the plane spanned by the two vectors. Under the effect of a rotation, the first one remains "locked" along the axis of rotation while the latter rotates by the corresponding angle and can be further broken into two components perpendicular to each other. The magnetization at the center of the k^{th} echo can be written as

$$\begin{aligned}\vec{M}(k)(\Delta\omega_o, \omega_1) &= (R(\theta, \hat{n}))^k \vec{M}(0^+) \\ &= R(k\theta, \hat{n})\vec{M}(0^+) \\ &= (\hat{n} \cdot \vec{M}(0^+))\hat{n} + (\vec{M}(0^+) - \hat{n}(\hat{n} \cdot \vec{M}(0^+)))\cos(k\theta) + (\hat{n} \times \vec{M}(0^+))\sin(k\theta)\end{aligned} \tag{5.2}$$

The total magnetization is calculated by summing over the contributions from all the spins. When the field is inhomogeneous enough such that we have a fairly large

dispersion of the angle θ, the last two terms are oscillatory and sum up to zero for sufficiently large k. They only contribute to the initial transient behavior. For our applications, when the bandwidth of the frequency offsets is more than 10 times the rf. amplitude, this approximation holds. The asymptotic magnetization is solely due to the first term

$$\vec{M}_{asy}(\Delta\omega_o, \omega_1) = (\hat{n} \cdot \vec{M}(0^+))\hat{n} \tag{5.3}$$

Denote

$$\begin{aligned} M_\perp &= M_{asy}(x) + iM_{asy}(y) \\ \hat{n}_\perp &= \hat{n}_x + i\hat{n}_y \end{aligned} \tag{5.4}$$

we have

$$\vec{M}_\perp = (\hat{n} \cdot \vec{M}(0^+))\hat{n}_\perp. \tag{5.5}$$

During the free precession periods, under the effect of the Larmor frequency offset, the two components of the transverse magnetization evolve as

$$\begin{aligned} M_{asy}(x) \rightarrow & M_{asy}(x)\cos(\Delta\omega_o t) + M_{asy}(y)\sin(\Delta\omega_o t), \\ M_{asy}(y) \rightarrow & M_{asy}(y)\cos(\Delta\omega_o t) - M_{asy}(x)\sin(\Delta\omega_o t), \end{aligned} \tag{5.6}$$

i.e. during this period, $M_\perp$ acquires a phase of $e^{-i\Delta\omega_o t}$.

If we integrate the magnetization over the distribution of the rf. inhomogeneity and Larmor offsets, we obtain the asymptotic echo in the time domain $m_{asy}(t)$. In other words, $m_{asy}(t)$ and $M_\perp$ are a Fourier transform pair.

$$m_{asy}(t) = \int\int \mathrm{d}\Delta\omega_o \omega_1 f(\Delta\omega_o, \omega_1) e^{-i\Delta\omega_o t}(\hat{n} \cdot \vec{M}(0^+))\hat{n}_\perp, \tag{5.7}$$

where $f(\Delta\omega_o, \Delta\omega_1)$ is the field distribution.

It should be emphasized again that we can discard the transients since as shown in experiment, the echo shape approaches the asymptotic form given by Eq.(5.7) very quickly, usually after the first three echoes.

Assume that the noise has a constant power spectral density and assume that a matched filter is used, the signal power to noise ratio is

$$SNR = \frac{\int_{-T/2}^{T/2} \mathrm{d}t m_{asy}(t) m_{asy}^*(t)}{N_o^2} \tag{5.8}$$

where T is the acquisition time and N_o^2 is the noise power. We will drop the constant N_o^2 from now on for convenience.

In principle, we can optimize the SNR directly by maximizing the value of this integral. However, evaluating this integral repeatedly at each step of an optimization algorithm is very inefficient. Thus, we desire a means of either approximating the integral or optimizing another metric that closely relates to SNR.

5.5 Method of optimizing SNR

According to the Parseval's theorem, for $T \to \infty$, the power in the time domain is equal to the power in the frequency domain. Ignoring the normalization factor of $\frac{1}{4\pi}$ we have

$$SNR(\infty) = \int\int d\Delta\omega_o d\omega_1 |f(\Delta\omega_o, \omega_1)|^2 [(\hat{n} \cdot \vec{M}(0^+))^2 \hat{n}_x^2 + (\hat{n} \cdot \vec{M}(0^+))^2 \hat{n}_y^2] \tag{5.9}$$

In addition, assume a perfect 90° excitation pulse so that $\vec{M}(0^+) = (0, 1, 0)$, we obtain $M_{asy}(x) = \hat{n}_x \hat{n}_y$, and $M_{asy}(y) = \hat{n}_y^2$. With the goal of maximizing the in phase component in the y direction, we wish to maximize

$$SNR^*(\infty) = \int\int d\Delta\omega_o d\omega_1 f^2(\Delta\omega_o, \omega_1) \hat{n}_y^4 \tag{5.10}$$

Furthermore, for simplicity, let us assume a uniform distribution of the Larmor offsets $\Delta\omega_o$ and no RF inhomogeneity, the quantity to be maximized is

$$\tilde{\Phi}' = \sum_{\Delta\omega_0} \hat{n}_y^4(\Delta\omega_0) \tag{5.11}$$

The number of parameters involved in the optimization of $\tilde{\Phi}'$ is very large and the function is highly non convex, i.e. we can easily get stuck to a local minimum. Towards this end, the GRAPE algorithm [65] proves to be a very efficient and successful method. It requires calculating analytically the gradient of the function that needs to be optimized and uses the result to update the direction in the search space in which we have to move in each step of the optimization process. We will now proceed to calculate the gradient of $\hat{n}_y$.

The unitary operator that performs a counter clockwise rotation of angle θ around an axis $\hat{n}$, where $\hat{n}$ is a unit vector, has the form

$$U(\theta, \hat{n}) = e^{-i\frac{\theta}{2}\hat{n}\cdot\sigma} \tag{5.12}$$

Given U, one can determine $\hat{n}$ up to a sign. To avoid ambiguity, we impose the constraint $\hat{n}_y \geq 0$.

The Hamiltonian of the spin system is

$$H(t) = H_0 + \sum_{k=1}^{m} u_k(t) H_k \tag{5.13}$$

where H_0 is the natural Hamiltonian, which in our case is $-\Delta w_0 I_z$. H_k represents the control Hamiltonians, which are I_x and I_y.

Denote the evolution due to free precession as U_0. If we discretize the controls in N small time steps and assume that the controls are constant in each time step Δt,

then

$$U = U_0 U_N \dots U_j \dots U_1 U_0, \tag{5.14}$$

where $U_j = \exp(-i\Delta t(H_o + \sum_{k=1}^{m} u_k(j) H_k))$.

If we perturb the control $u_k(j)$ by a small amount $\delta u_k(j)$, the resulting small change in U_j to first order in $\delta u_k(j)$ is

$$\delta U_j = -i\Delta t H_k U_j \delta u_k(j) \tag{5.15}$$

The proof to the above equation is given at the end of this section.

Therefore, to first order, the change in the total unitary operator is

$$\begin{aligned} \delta U &= \underbrace{U_0 U_N \dots (-i\Delta t) H_k U_j \dots U_1 U_0}\, \delta u_k(j) \\ &= \tilde{U} \delta u_k(j) \end{aligned} \tag{5.16}$$

We can write U in the explicit matrix representation that involves the Pauli matrices:

$$\begin{aligned} U &= e^{-i\frac{\theta}{2}\hat{n}\cdot\vec{\sigma}} \\ &= I\cos(\frac{\theta}{2}) + i\sin(\frac{\theta}{2})\hat{n}\cdot\sigma \\ &= \begin{bmatrix} \cos(\frac{\theta}{2}) + i\sin(\frac{\theta}{2})\hat{n}_z & \sin(\frac{\theta}{2})\hat{n}_y - i\sin(\frac{\theta}{2})\hat{n}_x \\ -\sin(\frac{\theta}{2})\hat{n}_y - i\sin(\frac{\theta}{2})\hat{n}_x & \cos(\frac{\theta}{2}) - i\sin(\frac{\theta}{2})\hat{n}_z \end{bmatrix}. \end{aligned} \tag{5.17}$$

Hence, $\hat{n}_y$ can easily be found from U. Also taking into account the constraint that $\hat{n}_y \geq 0$, we have

$$\hat{n}_y = \sqrt{\frac{\Re^2(U_{12})}{1 - \Re^2(U_{11})}} \tag{5.18}$$

Finally, the increment of $\hat{n}_y$ due to a small change in U is

$$\begin{aligned}\delta\hat{n}_y = &\frac{1}{2\sqrt{\frac{\Re^2(U_{12})}{1-\Re^2(U_{11})}}} \\ &\left(\frac{2\Re(U_{12})\delta\Re(U_{12})(1-\Re^2(U_{11})) + 2\Re(U_{11})\delta\Re(U_{11})\Re^2(U_{12})}{(1-\Re^2(U_{11}))^2}\right)\end{aligned} \tag{5.19}$$

From Eqs. (5.16) and (5.19) we can find $\delta\hat{n}_y$ in terms of $\delta u_k(j)$

$$\begin{aligned}\frac{\delta\hat{n}_y}{\delta u_k(j)} = &\frac{1}{2\hat{n}_y} \\ &\left(\frac{2\Re(U_{12})(1-\Re^2(U_{11}))\Re(\tilde{U}_{12}) + 2\Re(U_{11})\Re^2(U_{12})\Re(\tilde{U}_{11})}{(1-\Re^2(U_{11}))^2}\right)\end{aligned} \tag{5.20}$$

This is the analytical expression for the derivative of $\hat{n}_y$ with respect to the controls, to the first order. We can then numerically optimize any function of $\hat{n}_y$ using conjugate gradient instead of gradient descent for faster convergence.

The effective axis and angle of rotation is calculated step by step. Two consecutive rotation around axis $\hat{n}_1$ with angle θ_1 and axis $\hat{n}_2$ with angle θ_2 result in a rotation around axis $\hat{n}_{12}$ with angle θ_{12} that can be calculated using the quarternion representation of rotation [66]

$$\begin{aligned}\cos\left(\frac{\theta_{12}}{2}\right) =& \cos\left(\frac{\theta_1}{2}\right)\cos\left(\frac{\theta_2}{2}\right) - \sin\left(\frac{\theta_1}{2}\right)\sin\left(\frac{\theta_2}{2}\right)\vec{n}_1\cdot\vec{n}_2, \\ \sin\left(\frac{\theta_{12}}{2}\right)\hat{n}_{12} =& \sin\left(\frac{\theta_1}{2}\right)\cos\left(\frac{\theta_2}{2}\right)\hat{n}_1 + \cos\left(\frac{\theta_1}{2}\right)\sin\left(\frac{\theta_2}{2}\right)\vec{n}_2 \\ &- \sin\left(\frac{\theta_1}{2}\right)\sin\left(\frac{\theta_2}{2}\right)\hat{n}_1\times\hat{n}_2.\end{aligned} \tag{5.21}$$

Proof of Eq. 5.15

Let $\tilde{H} = H_o + \sum_{k=1}^{m} u_k(j)H_k$. The corresponding unitary evolution and its infinitesimal increment are

$$\begin{aligned}U_j &= \exp(-i\Delta t\tilde{H}) \\ \delta U_j &= \exp(-i\Delta t\tilde{H} - i\Delta t\delta u_k(j)H_k) - \exp(-i\Delta t\tilde{H})\end{aligned} \tag{5.22}$$

First, notice that if A is a time independent matrix, the solution to the vector differential equation

$$\frac{d}{dt}X(t) = AX(t) + B(t) \tag{5.23}$$

is given by

$$X(t) = e^{At}X(0) + e^{At}\int_0^t e^{-A\tau}B(\tau)d\tau \tag{5.24}$$

Now we wish to find the following quantity

$$\left(\frac{d}{dx}e^{A+Bx}\right)|_{x=0} \tag{5.25}$$

In order to do so, we introduce the scalar parameter λ and the function

$$g(x,\lambda) = \frac{d}{dx}e^{\lambda(A+Bx)}. \tag{5.26}$$

Denote $f(\lambda)$ the value of $g(x,\lambda)$ evaluated at $x = 0$, we have

$$f(\lambda) = \left(\frac{d}{dx}e^{\lambda(A+Bx)}\right)|_{x=0} \tag{5.27}$$

Notice that the quantity of interest is just $f(1)$.

Taking the derivative of f with respect to λ we have

$$\begin{aligned}\frac{df}{d\lambda} &= \left(\frac{d}{dx}[(A+Bx)e^{\lambda(A+Bx)}]\right)|_{x=0} \\ &= \left(Be^{\lambda(A+Bx)} + (A+Bx)\frac{d}{dx}e^{\lambda(A+Bx)}\right)|_{x=0} \\ &= Be^{\lambda A} + Af(\lambda)\end{aligned} \tag{5.28}$$

We already know how to solve this equation for f. Using Eq. 5.24 we have

$$f(\lambda) = e^{A\lambda}f(0) + e^{A\lambda}\int_0^\lambda e^{-A\tau}Be^{A\tau}d\tau \tag{5.29}$$

Notice that $f(0) = 0$ and with the appropriate change of variable, we can rewrite the above expression as

$$\left(\frac{d}{dx}e^{\lambda(A+Bx)}\right)|_{x=0} = \left(\int_0^{\lambda} e^{A\tau}Be^{-A\tau}d\tau\right)e^{\lambda A} \tag{5.30}$$

Therefore,

$$\left(\frac{d}{dx}e^{A+Bx}\right)|_{x=0} = \left(\int_0^{1} e^{A\tau}Be^{-A\tau}d\tau\right)e^{A} \tag{5.31}$$

In order to simplify the RHS of (5.22) , it is actually more convenient to use Eq.(5.29) with $\lambda = \Delta t$. To first order in $\delta u_k(j)$

$$\delta U_j = \left(\int_0^{\Delta t} e^{-i\tilde{H}\tau}(-iH_k)e^{i\tilde{H}\tau}d\tau\right)U_j\delta u_k(j). \tag{5.32}$$

For small enough Δt, $\Delta t \ll |\tilde{H}||^{-1}$, the above expression further simplifies to

$$\delta U_j = -i\Delta t H_k U_j \delta u_k(j). \tag{5.33}$$

5.6 Short refocusing pulses

5.6.1 Short Symmetric Phase Alternating pulses

We first limit ourselves to a perfect excitation pulse that brings all the magnetization to the y axis and search for a refocusing pulse that has the same length as that of a rectangular 180°, i.e. $t_p = t_{180}$. It is surprising that there exist pulses of such a short duration that are capable of greatly improving the SNR of the echoes. They all have the form $\alpha_{-y}\,\beta_{+y}\,\alpha_{-y}$. It turned out that pulses of this form were called Symmetric Phase Alternating (SPA) that were studied in Ref. [67]. However, they were studied in the context of designing a perfect rotation over a certain bandwidth

centered at the resonance frequency. In particular, the paper demonstrated that the pulse $60^\circ_{-x}360^\circ_{x}60^\circ_{-x}$ acts as a π refocusing pulse over a wider bandwidth than the standard π pulse. Nevertheless this pulse is more than twice as long as t_{180} and does not provide a significant increase in SNR. In fact, perfect rotation has always been the goal a large body of literature on 180° pulses.Our pulses are distinctive from the above mentioned ones because they do not provide perfect rotation near resonance but instead sacrifice the performance near resonance to refocus more spins off resonance. The total number of spins that are refocused is increased leading to an increase in SNR.

In this section, we analyze the performance of short SPA pulses of the form $\alpha_{-y}\beta_{y}\alpha{-}y$. Let us consider the following three specific implementations of the SPA pulses

- SPA -1.0 $\{\alpha, \beta\} \approx \{0.14\pi, 0.72\pi\}$
- SPA -1.3 $\{\alpha, \beta\} \approx \{0.2\pi, 0.9\pi\}$
- SPA -1.9 $\{\alpha, \beta\} \approx \{0.3\pi, 1.3\pi\}$

The standard refocusing pulse corresponds to the configuration $\alpha = 0, \beta = \pi$. The number next to SPA indicates the total length of the pulse in unit of t_{180}, which is the length of the standard hard pulse.

Figure 5.2 shows the pulse profiles. All SPA pulses use the same rf. amplitude as that of the standard pulse. Compared to the standard pulse, the new pulses are of equal length or not much longer. Therefore, they introduce either no or little penalty with regards to power or the ability to measure short relaxation times.

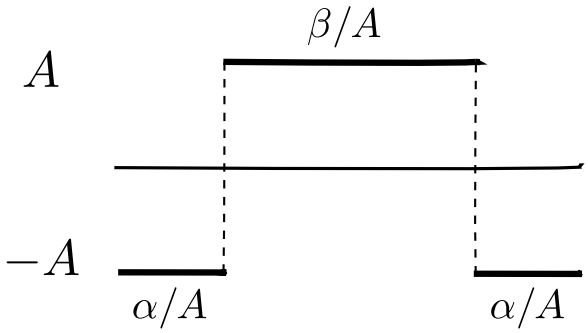

Figure 5.2: Profile of an SPA pulse. A is the nominal rf amplitude. The pulse has constant amplitude and alternating phases $-y$ and y. A rectangular hard pulse corresponds to $\alpha = 0$, $\beta = \pi$.

Apart from these specific values, there are many other combinations of α and β that can be used. Combinations that give improved SNR compared to the standard pulse are indicated by the red colors in Fig 5.3.

Ideally, a good refocusing pulse displays $n_y^2 = 1$ over a very large region of the $(\Delta\omega_0, \omega_1)$ space. Figure 5.4 shows the distribution of $\hat{n}_y^2$ for the new pulses and the standard pulse. The spacing between the application of two consecutive refocusing pulses is chosen to be equal to $6t_{180}$. As shown in the figure, compared to the standard pulse, the in phase magnetization for the new pulses is bigger in a larger region of field inhomogeneities. At the nominal rf. frequency, it is clear that the new pulses can focus more spins far off resonance. In particular, the performance of SPA-1.0 is inferior in the close vicinity of resonance, but this is more than compensated for by the performance off-resonance.

Next, we examine the asymptotic echo shapes and the SNR of the new pulses. Figure 5.5 shows the echo shape $m(\omega_1, t)$ for different values of ω_1. The echo peaks for the new pulses are constantly high compared to that of the standard pulse. In

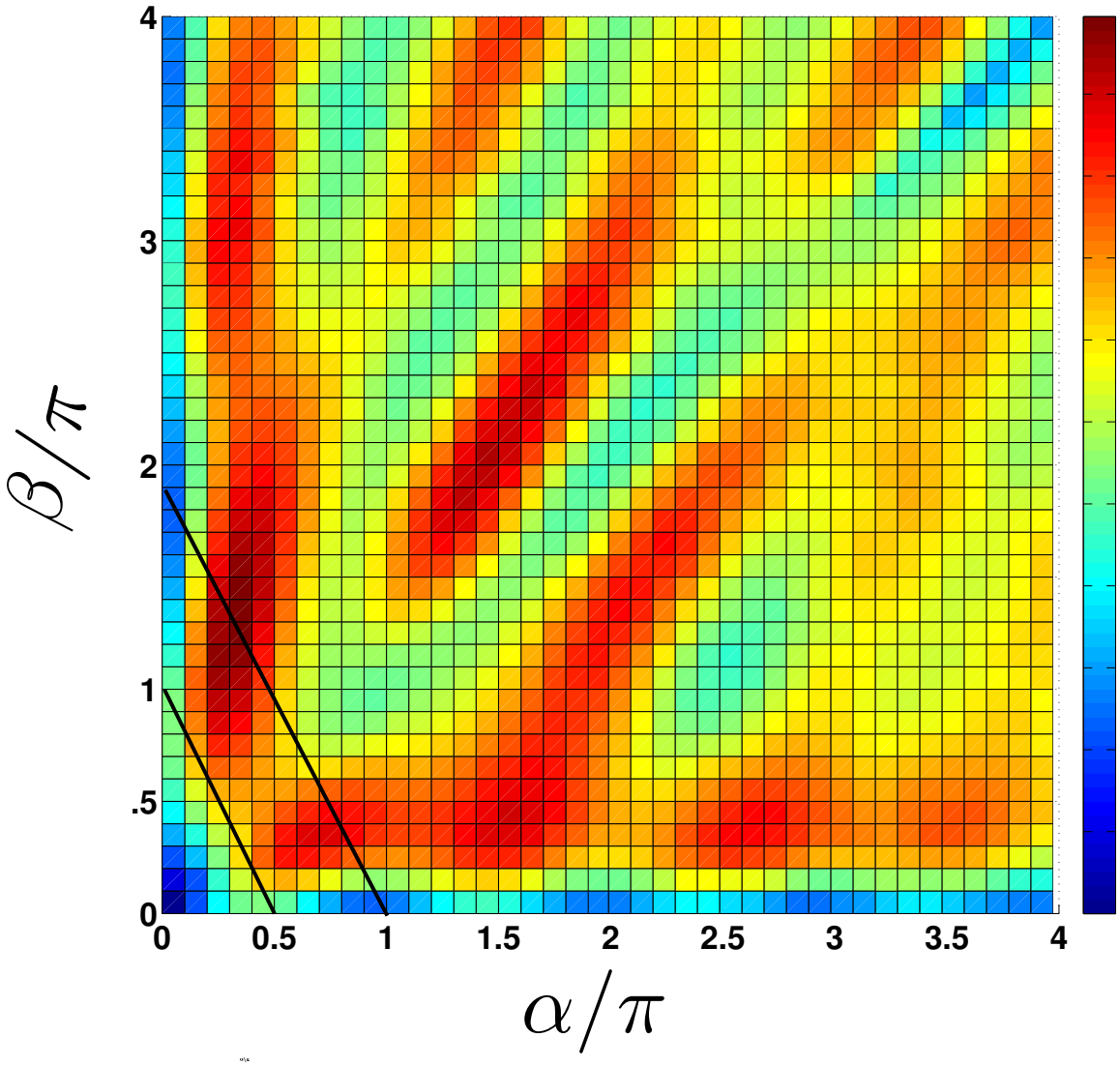

Figure 5.3: $\sum \hat{n}_y^2$ for different combinations of α and β. The color bar shows improving performance in the upward direction.

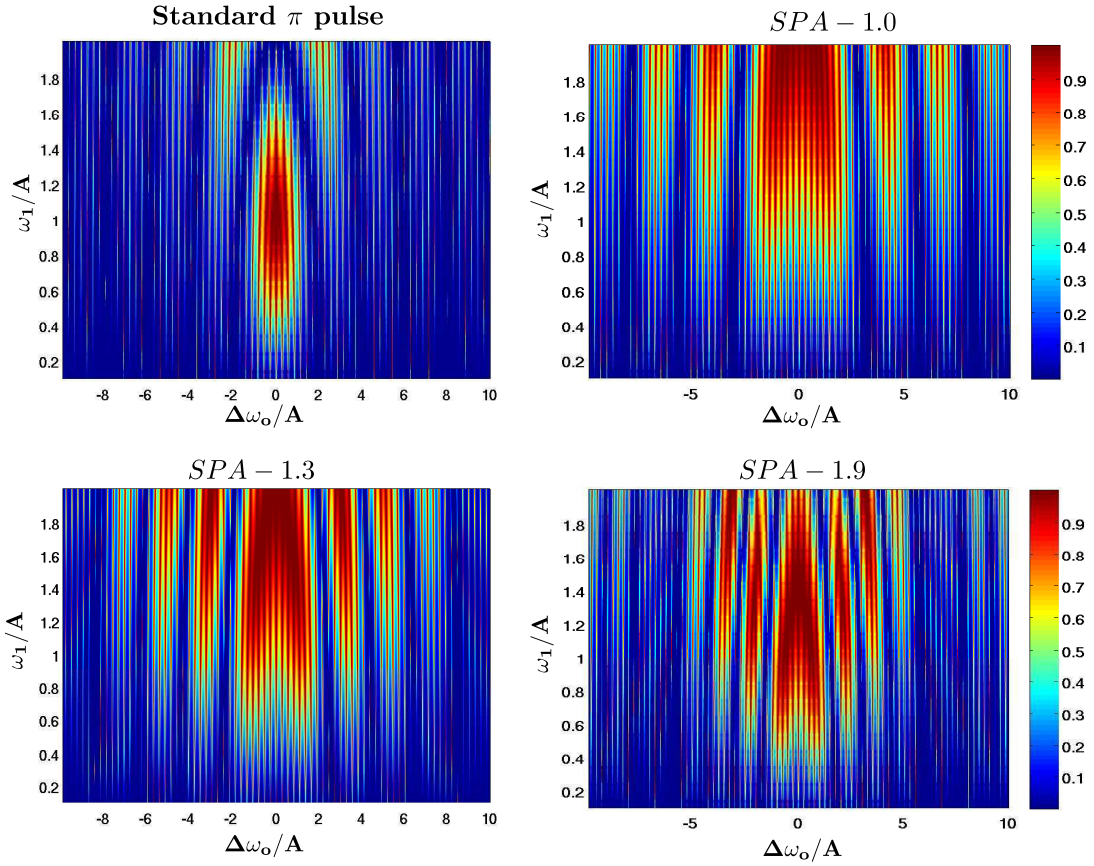

Figure 5.4: $\hat{n}_y^2$ over the field inhomogeneities for different pulses. The echo spacing is $t_E = 6t_{180} + t_p$, where t_p is the corresponding pulse duration. A is the nominal rf. amplitude.

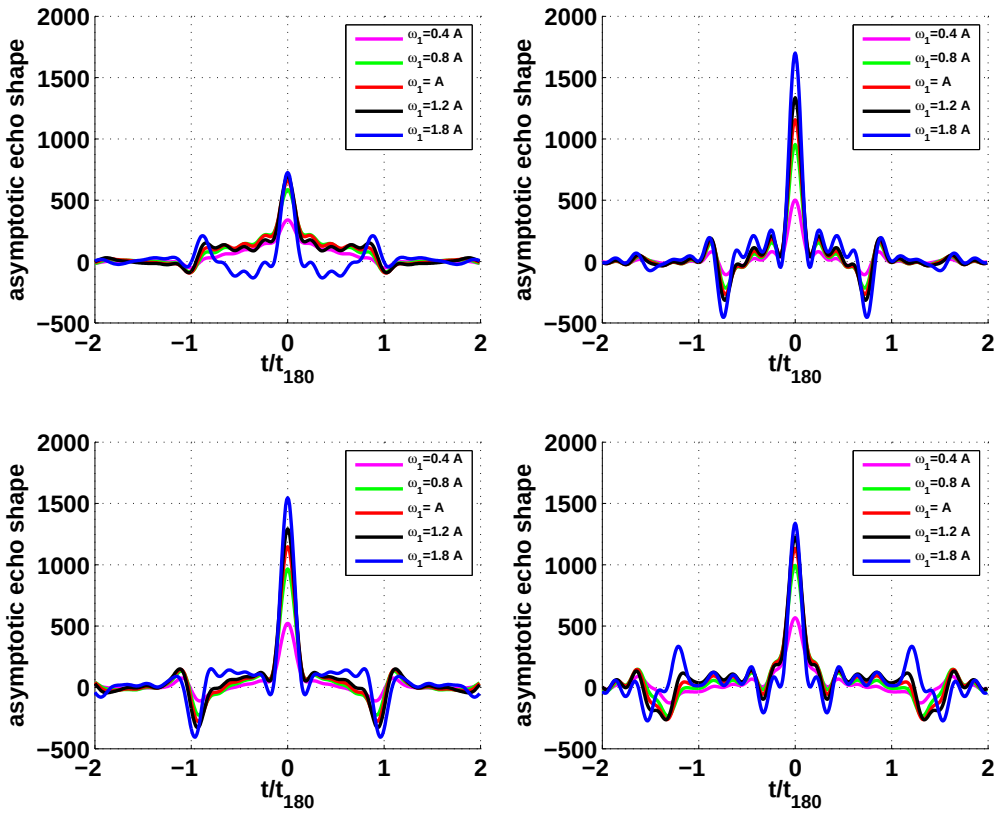

Figure 5.5: The asymptotic echo shape for different pulses with rf. inhomogeneity assuming a perfect initial 90° pulse. A is the nominal rf. amplitude

particular, the peak for SPA-1.0 increases as the rf. amplitude increases.

Now assume a uniform distribution for the rf. inhomogeneity. We calculate the SNR for all for pulses and normalize it with respect to the SNR for the hard pulse at the nominal rf amplitude. The result is shown in Fig. 5.6. The SNR stays constantly high for the new pulses in the presence of large rf. inhomogeneity. In particular, SPA-1.0 is less sensitive to rf inhomogeneity than the hard pulse. At 90% rf. inhomogeneity, the hard pulse looses half of the nominal value, while the SPA

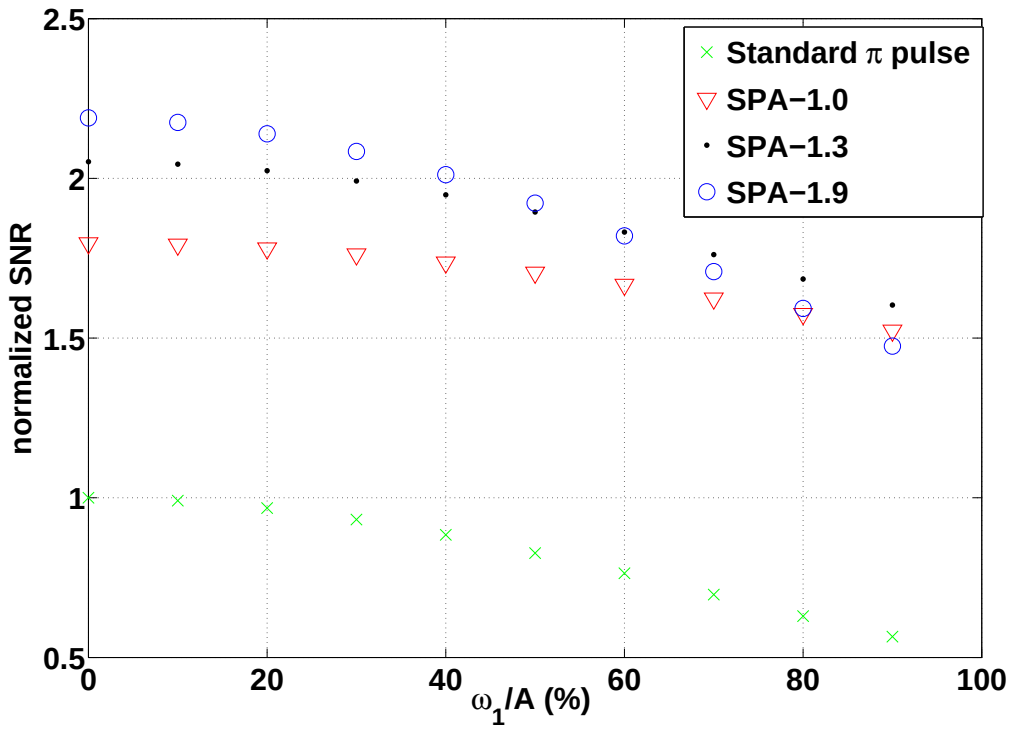

Figure 5.6: SNR in the presence of rf inhomogeneity. SNR normalized to the SNR of the standard refocusing pulse at the nominal rf amplitude A. A perfect 90° excitation pulse is assumed. The SPA pulses are clearly less sensitive to mis calibration of rf. amplitude than the standard 180° pulse. The acquisition window is $t_p + 6t_{180}$, where t_p is the pulse length.

pulses still produce an SNR 1.5 times the nominal value.

Table 5.1 summarizes the performance of the SPA pulses at the nominal rf. amplitude with the assumption of a strong 90°_X excitation pulse. This excitation pulse tips all spins from the z axis to the y axis. That means the only limiting factor to the SNR is the refocusing ability of the refocusing pulse. Obviously, the SPA pulses can potentially yield much higher SNR than what the hard pulse can possibly achieve thanks to their ability to refocus more spins outside the reach of the standard 180°

Table 5.1: SNR of the standard refocusing pulse and SPA pulses with a perfect 90° excitation pulse. The SNR is normalized with respect to the SNR for the hard 180° pulse with a perfect 90° excitation pulse. We assume nominal rf amplitude for all these calculations. The acquisition window is $t_p + 6t_{180}$, where t_p is the pulse length.

Pulse name	Normalized SNR
Standard 180°pulse	1.00
SPA-1.0	1.80
SPA-1.3	2.05
SPA-1.9	2.19

pulse.

The simulations for these three pulses show that SPA pulses possess similar characteristics. While SPA pulses of various lengths can be useful for different applications, we are here most interested in $SPA - 1.0$ because it has the same duration as that of the standard π pulse.

5.6.2 Experimental verification

Several experiments were conducted to confirm the performance of the new refocusing pulse $SPA-1.0$ and they yield excellent agreement with the simulation. From now on, we will refer to this pulse simply by SPA.

Asymptotic magnetization and asymptotic echo shape

We first measure the asymptotic magnetization and asymptotic echo shape. The results reported here are from experiments conducted using a Bruker Avance-II spectrometer. The superconducting magnet (Oxford) was set up at 1 T, that is 42.57 MHz proton frequency. The sample was placed inside a cylindrical tube with diameter 5 mm and length 15 cm. The tube in turn was centered within an imaging probe with

inner diameter 12 cm that was placed parallel to the bore of the magnet. A gradient coil along z direction was turned on to create a uniformly distributed frequency offsets. The gradient strength was chosen to be small $g = 1G/cm$ to minimize diffusion effect. An rf field of low power level $A = 1$ kHz was chosen. With this value of A, the length of a nominal π pulse is $t_{180} = 500\mu s$, which is also the length of $SPA - 1.0$. The echo spacing is $t_E = 6.5$ ms, which is $13t_{180}$. This echo spacing is long enough to ensure that we can capture the entire echo shape and at the same time short enough to safely neglect the effects of diffusion. As a double check, the characteristic length of the refocused region was $\omega_1/(\gamma g) = 2.3$ mm, which is much shorter than the length of the sample. As seen in the simulations, significant contribution to the SNR comes from spins as far as $\pm 20\omega_1$.

Fig 5.7 shows the asymptotic echo shape. In the first case, both standard 90° excitation and 180° refocusing pulses are used. Both have finite bandwidths that limit the total number of spins that are irradiated. When the standard 90° is then replaced by a strong 90° that is 10 times higher in amplitude and subsequently 10 times shorter in duration, there is an obvious increase in the echo peak, which means the total magnetization is increased. This shows that the standard 180° is capable of refocusing spins over a wider bandwidth than the excitation bandwidth of the standard 90°. With the use of the strong 90°, the limiting factor is now the refocusing pulse. Replacing the standard 180° by the SPA pulse provides another boost to the SNR.

Fig 5.8 shows the asymptotic magnetization. Again, experiment agrees very well with simulation. It is clear that the SPA refocusing pulse does not refocus spins

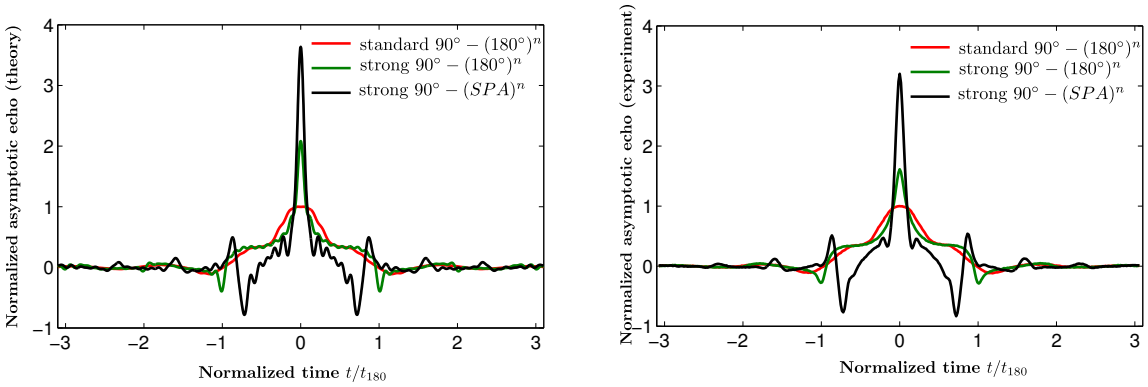

Figure 5.7: Asymptotic echo shapes produced by different excitation and refocusing pulses. The left figure shows the result obtained by simulation, while the right one shows the experimental results. The peak amplitude for each echo is normalized with respect to that of the standard CPMG sequence. The sample was dionized (DI) water with transverse relaxation time $T_2 = 1.9$ s. $t_{180} = 500\mu$ s. The echo spacing was 6.5 ms. The acquisition time for each echo was 3.07 ms long. Data taken with permission from the co-authors in [1]

close to resonance as well as the standard 180° pulse. However, this is more than compensated by the large number of spins refocused far from resonance, as shown in the big side lopes in the corresponding spectrum.

Relaxation measurement with a practical excitation pulse

Until now, we have ignored the effect off relaxation. Relaxation causes a decay in the amplitudes of the echoes over time. In the simplest case where both the 90° excitation and 180° excitation pulses are instantaneous pulses that excite and refocus all spins, then the magnetization is always on the traverse plane and the echo peaks decay exponentially with time constant T_2. However, when the pulses are not perfect, there is magnetization in the longitudinal direction that can contribute to the echoes, an effect called indirect echo. As a consequence, the decay rate is a function of both

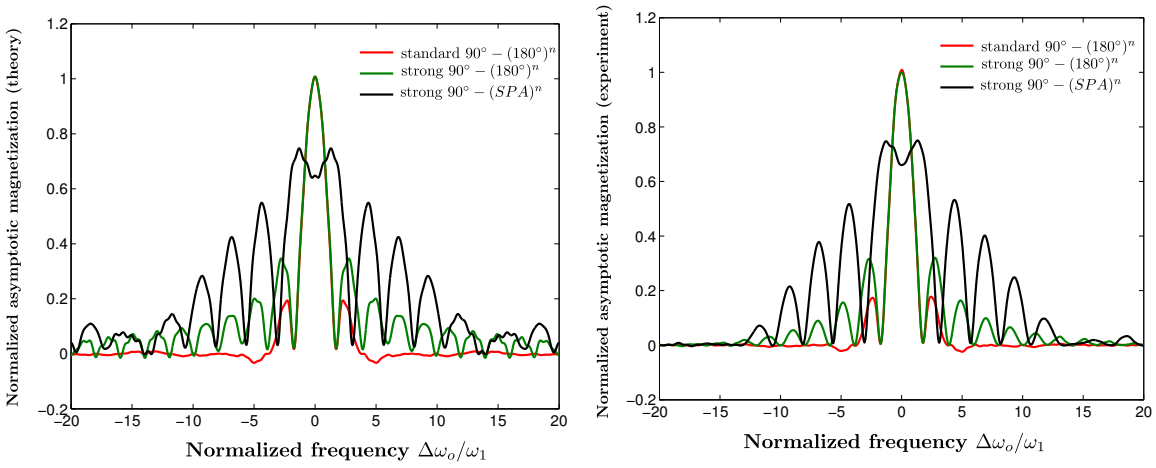

Figure 5.8: Asymptotic magnetization, the y component of $\vec{M}_{asy}$, produced by different excitation and refocusing pulses. The left figure shows the results obtained by simulation, while the right one shows the experimental results. The sample was deionized (DI) water with transverse relaxation time T_2= 1.9 sec. $t_{180} = 500\mu$ s. The echo spacing was 6.5 ms. The acquisition time for each echo was 3.07 ms long. Data taken with permission from the co-authors in [1]

T_1 and T_2.

This decay has time constant $T_{2,eff}$ is a weighted sum of T_1 and T_2 according to the following equation [64]

$$\frac{1}{T_{2,eff}} = \langle \hat{n}_y^2 \rangle \frac{1}{T_2} + \langle \hat{n}_z^2 \rangle \frac{1}{T_1} \tag{5.34}$$

where $\langle \hat{n}_y^2 \rangle$ and $\langle \hat{n}_z^2 \rangle$ are the average of the square of the transverse and longitudinal components of $\hat{n}$. Since $\langle \hat{n}_y^2 \rangle + \langle \hat{n}_z^2 \rangle = 1$ in the simple case $T_1 = T_2$ we have $T_{2,eff} = T_1$ and the decay is independent of what pulse sequences are used. On the other hand, when $T_1 \neq T_2$, we need to calculate $\langle \hat{n}_y^2 \rangle$ and $\langle \hat{n}_z^2 \rangle$ from the refocusing pulses used in order to find out the value of $T_{2,eff}$.

$$\langle \hat{n}_y^2 \rangle = \frac{\int\int d\Delta\omega_o d\omega_1 f(\Delta\omega_o, \omega_1) F(\Delta\omega_o) \hat{n}_y^2 M_{asy}(y)}{\int\int d\Delta\omega_o d\omega_1 f(\Delta\omega_o, \omega_1) F(\Delta\omega_o) M_{asy}(y)}, \tag{5.35}$$

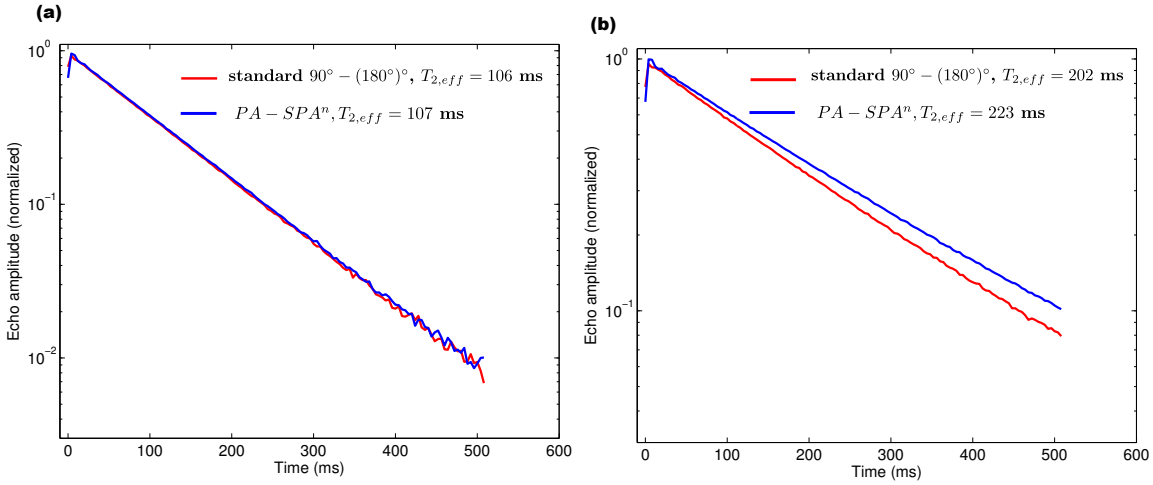

Figure 5.9: Measured echo amplitudes of (a) NiCl solution with $T_1 = T_2$ and (b) skim milk with $T_1 > T_2$. The echo amplitudes are normalized with respect to the amplitudes extrapolated to $t = 0$. Data taken with permission from the coauthors in Ref. [2].

where $f(\Delta\omega_o, \omega_1)$ is the field distribution and $F(\Delta\omega_o)$ is the frequency response of the filter. Here the field distribution is uniform and the filter used is a matched filter.

In this experiment, we use a practical excitation pulse that has the same amplitude as that of the SPA pulse and duration $6.1698t_{180}$. This pulse is called $PA1$ and is discussed in detail in Ref. [2]. Two sets of measurement were conducted. One uses the standard 90° as the excitation pulse and the standard 180° as the refocusing pulse. The other uses PA1 as the excitation pulse and $SPA - 1.0$ as the refocusing pulse.

We first performed measurements on a sample of water doped with NiCl that has $T_1 = T_2$. $T_{2,eff}$ was measured to be 106 ± 1 ms for both pairs of excitation and refocusing pulses. This result is close enough to the value of $T_1 = 111$ ms measured by an inversion-recovery scheme. The results are shown in Fig. 5.9(a).

Next, we use skim milk as a sample. This sample is known to have $T_1 > T_2$. The

pair $PA1-SPA$ yields a larger $T_{2,eff}$ meaning that the echoes decay at a slower rate compared to the case when rectangular 90° and 180° are used. The results are shown in Fig. 5.9(b). Using $T_1 = 1.51$ s and the values of $\langle \hat{n}_z^2 \rangle$ calculated for each pair of pulses we obtained similar results for T_2: 179.2 ms for the $PA1-SPA$ and 179.8 ms for the rectangular 90° and 180° pair.

5.6.3 Summary

In summary, we have described a class of new refocusing pulses named SPA that have the form $\alpha_{-y}\beta y\alpha_{-y}$. The key difference of these pulses compared to traditional refocusing pulses is that they do not perform well near resonance but this is more than compensated for by the performance far off resonance. In applications where the fields are highly inhomogeneous, the new SPA pulses outperform the standard refocusing pulses in all aspects. They are able to focus spins over a thicker slice and stay less insensitive to rf inhomogeneity. In particular $SPA-1.0$ which is $27^\circ_{-y}146^\circ_{y}27^\circ_{-y}$ does not consume any more power than the standard refocusing pulse but has the potential to nearly double the SNR of the echoes.

5.7 Excitation pulse

In this section we discuss the excitation pulses that exploit the full potential of the SPA refocusing pulse. Unlike the refocusing pulse, the excitation pulse is only used once in the CPMG sequence so we can relax the constraint on the pulse length since the increase in power is only minimal. Nevertheless, shorter excitation pulse are desirable in order to capture short relaxation times. We also limit the maximum rf.

amplitude to that of the refocusing pulse.

A rectangular 90° excitation is guaranteed to produce a bad performance as shown previously. Many previous works have successfully generated excitation pulses with wide bandwidths under limited rf. amplitude [68, 69, 70]. For example, in [69] a phase-modulated excitation pulse of length $20t_{180}$ can transfer longitudinal magnetization to the y axis with less than 1% errors over a bandwidth of $\pm 2.5\omega_1$. Nevertheless, this pulse does not increase the SNR significantly when using with the SPA refocusing pulse because the latter has refocusing regions extending over $\pm 10\omega_1$. The excitation pulse $PA1$ in Ref. [2] is shorter, only $6.2t_{180}$, and also has a BW of $\pm 2.5\omega_1$ although with smaller fidelity. $PA1$ produces a higher SNR because it is tailored to the SPA pulse and not the perfect excitation profile near resonance. Nevertheless, it is still suboptimal because it only tries to bring the initial magnetization to the y axis. As shown in Eq. 5.3, since $|\hat{n} \cdot \vec{M}(0+)| \leq 1$, for a given refocusing pulse, making $\hat{n}(\Delta\omega_0, \omega_1)$ and $\vec{M}(0+)(\Delta\omega_0, \omega_1)$ collinear is key to further improve SNR. $\hat{n}$ for an instantaneous refocusing pulse points along the y direction, but in general has both the transverse and longitudinal components. Therefore the full potential of the SPA pulse will be realized with an excitation pulse that can tip each spin to a position that matches the axis of rotation of the refocusing cycle corresponding to the same frequency offset. We named such a pulse $AMEX$. Table 5.2 shows the performance of the standard and the SPA refocusing pulses in conjunction with different excitation pulses. The perfect 90° is infinitely narrow. The perfect $AMEX$ pulse brings all the spins to their corresponding axes of refocusing cycles.

Here we assume no dispersion in the rf. amplitude ω_1 and a uniformly distibution

Table 5.2: The table shows the SNR obtained by using different pairs of excitation and refocusing pulses. All SNRs are normalized with respect to the SNR obtained by using the standard excitation and refocusing pulse. The perfect 90° brings all magnetization to the y axis. The perfect $AMEX$ brings all magnetization to the corresponding axes of the refocusing cycle.

Pulse name	Standard 180° pulse	$SPA-1.0$
Standard 90°	1	¡1
Perfect 90°	1.3	2.3
Perfect $AMEX$	2.4	4.6

of the Larmor frequency offsets $\Delta\omega_o$ in a gradient field. We first calculated the overall axis of rotation $\hat{n}$ as a function of the $\Delta\omega_o$ and $\tau = \frac{1}{2}(t_E - t_p)$. Only $\hat{n}_y$ and $\hat{n}_z$ are non zero due to the symmetry of the pulse. Even though the SPA pulse is quite simple, the expression for $\hat{n}$ is not simple enough to design a closed loop analytical solution for the excitation pulse that works for all values of echo spacing. We then limit ourselves to one particular value of the echo spacing and search for the excitation pulse numerically.

5.7.1 AMEX pulses

We started with a state-to-state transfer that brings the magnetization from the z axis to $\hat{n}(\Delta\omega_o)$. This pulse consists of 100 segments, each having length $0.1 \times t_{180}$ resulting in a total pulse duration of $10t_{180}$. The pulse is named $AMEX_{SPA,0}$ and its profile is shown in Fig. 5.7.1. This pulse is both phase- and amplitude-modulated.

In combination with the refocusing pulse $SPA-1.0$, this produces an SNR of 1.79 the value of the SNR for the hard refocusing pulse with a perfect 90° pulse. The excitation pulse is 20 times as long as a hard 90° pulse, but since it is only applied once for the acquisition of thousands of echoes, this is not a big issue. With respect

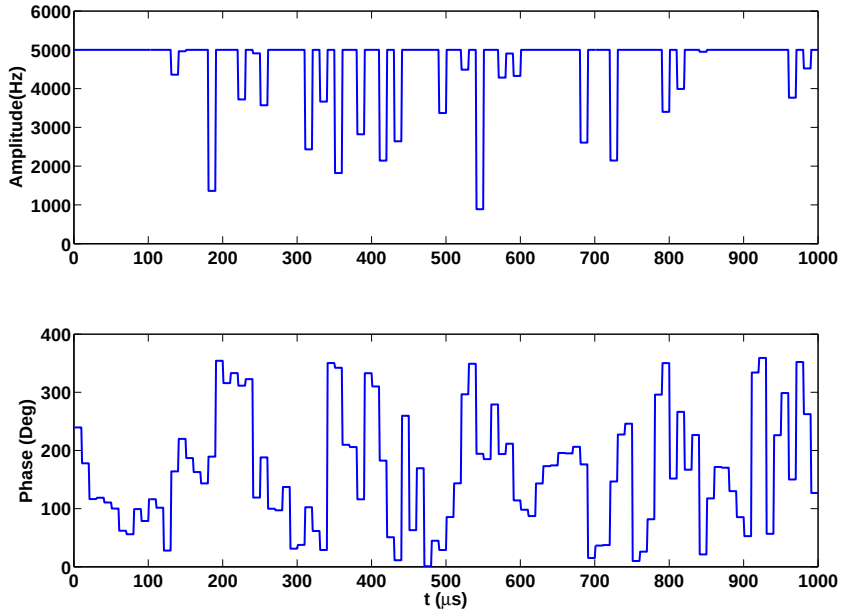

Figure 5.10: Amplitude and phase of $AMEX_{SPA,0}$. The nominal rf amplitude used is $A = 5kHz$. Therefore, $t_{180} = 100\mu$ s. The pulse is 1 ms long.

to the current excitation pulse used in well logging, which is also a hard 90° pulse with a reduced free precession time before the first echo of t_{180}/π, this ratio is 2.04, which is a 100% improvement. The echo shapes of the current implementation and the proposed implementation are shown in Fig. 5.7.1 for comparison.

$AMEX_{SPA,0}$ is then used as an initial guess for more iterations of optimization by keeping the pulse amplitude at the maximally allowed value and varying the phase only. The step size was chosen to be $\Delta t = 0.078t_{180}$. This new search yielded results that are much closer to the theoretical limit. Two of the representative pulses are $AMEX_A$ and $AMEX_B$. They have length $12.636t_{180}$ and $15.756t_{180}$ respectively. More pulses of this kind are discussed in detail in Ref. [3].

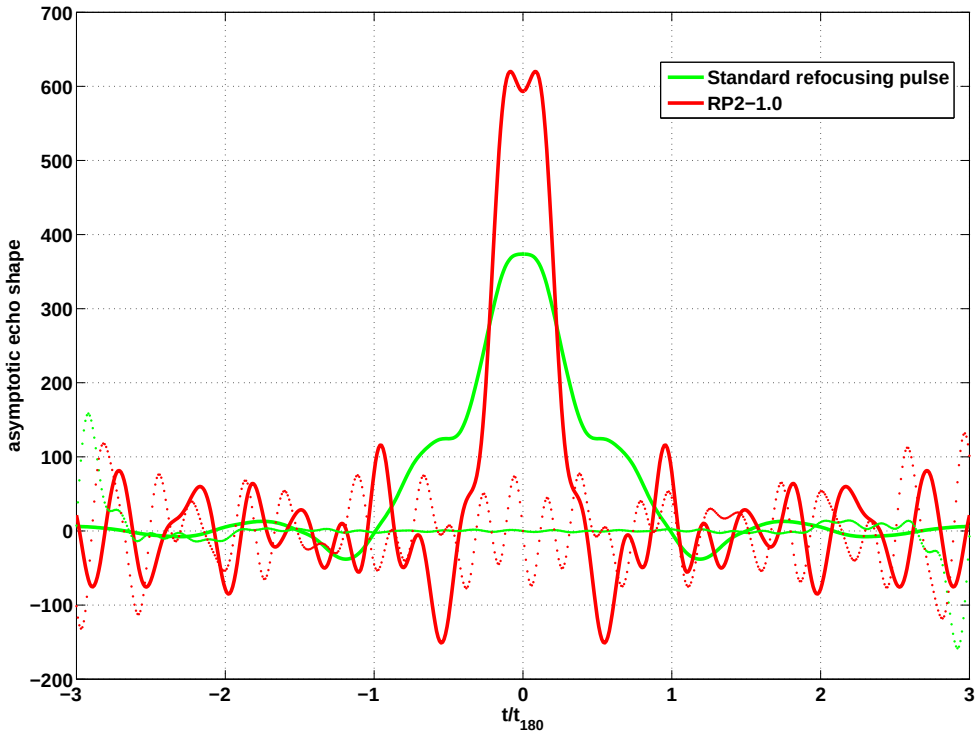

Figure 5.11: Comparison of the echo shapes generated from 3126 spins in a constant gradient. The green curves show the echo shape of the standard refocusing pulse with a hard 90° pulse and a reduced delay free precession time t_{180}/π. The red curves show the echo shape of SPA-1.0 with the new excitation pulse. The solid curves show the in phase components, while the dotted curves show the out of phase components.

Optimal pulse length

One reason for the improved performance of $AMEX_{SPA,A}$ and $AMEX_{SPA,B}$ compared with the performance of $AMEX_{SPA,0}$ is the smaller step size. Decreasing the step size too much will, however, increase the number of parameters and will make the search more prone to getting stuck in a local minimum. In addition, a closer look at the components of $\hat{n}$ provides some insight into the minimum length of the excitation pulse.

The SPA pulse comprises of three rotations around the y, $-y$, and y axis by angles $\theta_1, \theta_2, \theta_1$ respectively. The angles satisfy the condition $2\theta_1 + \theta_2 = \pi$.

A rotation around an axis in the $y - z$ plane

$$e^{-i\phi\hat{n}\cdot\vec{\sigma}} = \cos(\phi)I - i\sin(\phi)(\hat{n}_x\sigma_x + \hat{n}_z\sigma_z) \tag{5.36}$$

Let us denote 2τ as the free precession period between the application of two consecutive refocusing pulses, and

$$\begin{aligned} \theta_1' &= \frac{\sqrt{\Delta\omega^2 + A^2}}{A}\theta_1, \\ \theta_2' &= \frac{\sqrt{\Delta\omega^2 + A^2}}{A}\theta_2. \end{aligned} \tag{5.37}$$

where $\Delta\omega$ is the Larmor offset and A is the amplitude of the r.f. pulse.

In addition, define

$$\begin{aligned} \sin\alpha &= \frac{A}{\sqrt{\Delta\omega^2 + A^2}} \\ \cos\alpha &= \frac{\Delta\omega}{\sqrt{\Delta\omega^2 + A^2}}. \end{aligned} \tag{5.38}$$

We have

$$\begin{aligned} V_y &= -\sin(\phi)\hat{n}_y \\ &= -\sin(\theta_1')\sin(\alpha)\cos(\frac{\theta_2'}{2}) - \sin\alpha\sin(\frac{\theta_2'}{2})[\cos^2(\frac{\theta_1'}{2}) + 4(\cos^2\alpha - 1)\sin^2(\frac{\theta_1'}{2})] \end{aligned} \tag{5.39}$$

$$\begin{aligned} &V_z = -\sin(\phi)\hat{n}_z \\ &\sin(\frac{\theta_2'}{2})[\cos^2(\frac{\theta_1'}{2})\cos(\Delta\omega\tau)\cos\alpha - \sin(\theta_1')\sin(\Delta\omega\tau)\cos(2\alpha) - \sin^2(\frac{\theta_1'}{2})\cos(\Delta\omega\tau)\cos(3\alpha)] \\ &- \cos(\frac{\theta_2'}{2})[\cos(\theta_1')\sin(\Delta\omega\tau) + \sin(\theta_1')\cos(\omega\tau)\cos\alpha]. \end{aligned} \tag{5.40}$$

$$\begin{aligned} V_x &= f(\Delta\omega, P) \\ V_z &= g_1(\Delta\omega, P)\cos(\Delta\omega\tau) + g_2(\Delta\omega, P)\sin(\Delta\omega\tau) \end{aligned} \tag{5.41}$$

Impose the condition that $\hat{n}_y$ is always positive, we have

$$\hat{n}_x = \frac{|V_y|}{\sqrt{V_y^2 + V_z^2}} \tag{5.42}$$

$$n_z = {}_{\text{sign}}(V_y V_z)\frac{|V_z|}{\sqrt{V_y^2 + V_z^2}} \tag{5.43}$$

It is easy to see that V_y is an even and V_z is an odd function of $\Delta\omega$. Therefore, $\hat{n}_y$ is an even, while $\hat{n}_z$ is an odd function of $\Delta\omega$ as expected.

Both the transverse and longitudinal components of $\hat{n}$ exhibit oscillatory behavior with frequency with respect to $\Delta\omega_o$ on the order of $1/t_E$. The excitation pulse must be able to produce magnetization that closely matches this behavior in order to contribute to the overall SNR. That is the why the length of the excitation pulse cannot be smaller than t_E. In the case considered here $t_E = 7t_{180}$ so the lengths of the $AMEX$ pulses are of the same order of magnitude with t_E.

5.7.2 Phase cycling

We next discuss phase cycling, an important issue in the application of the $AMEX$ pulses. Phase cycling is a standard practice in NMR experiment to eliminate residual effects such as voltage offsets and pulse ringing. To achieve this goal, for each measurement, two experiments are done with an appropriate phase shift of the pulses in the second experiment compared to the firs one. The results are then added or

subtracted from each other to yield the desired result. For a standard CPMG experiment, only the transverse component of the magnetization in the y direction is inverted by a π pulse. For AMEX pulses, however, both the transverse and longitudinal components need to be retained, which require a different procedure for phase cycling. The goal is to invert both the transverse and the longitudinal components in the second experiment.

Because of the symmetry of the refocusing pulse $\alpha_y\beta_{-y}\alpha_y$ it is easy to show that the axis of the refocusing cycle $\hat{n}$ lies entirely on the $y-z$ plane and has the following properties:

$$\begin{aligned} \hat{n}_x(\Delta\omega_o, \omega_1) &= 0 \\ \hat{n}_y(\Delta\omega_o, \omega_1) &= \hat{n}_y(-\Delta\omega_o, \omega_1) \\ \hat{n}_z(\Delta\omega_o, \omega_1) &= -\hat{n}_z(-\Delta\omega_o, \omega_1) \end{aligned} \tag{5.44}$$

i.e., $\hat{n}_y$ is even, $\hat{n}_z$ is odd with respect to the Larmor offsets, and $\hat{n}_x$ is equal to zero.

We will assume that there is no dispersion in the rf. amplitude ω_1. Let us look at the effect of a phase change in the excitation pulse. In the rotating frame of the rf. frequency, a pulse of amplitude ω_1 and phase ϕ operating at the offset frequency $\Delta\omega_o$ for a period Δt is equivalent to a rotation that has axis $\hat{m}$ and angle α given by

$$\begin{aligned} \hat{m} &= \left(\frac{\omega_1\cos(\phi)}{\Omega}, \frac{\omega_1\sin(\phi)}{\Omega}, \frac{\Delta\omega_0}{\Omega}\right) \\ \alpha &= \Omega\Delta t. \end{aligned} \tag{5.45}$$

Here $\Omega = \sqrt{\Delta\omega_o^2 + \omega_1^2}$ is called the nutation frequency.

By making the phase change $\phi \to -\phi + \pi$, the new excitation pulse, denoted by the superscript ^{p} does not affect the nutation angle Ω, but has the following axis of

rotation

$$\hat{m}^p = (-\frac{\omega_1 \cos(\phi)}{\Omega}, \frac{\omega_1 \sin(\phi)}{\Omega}, \frac{\Delta\omega_o}{\Omega}) \tag{5.46}$$

Comparing Eq. 5.45 and Eq. 5.46, we see that

$$\hat{m}^p(-\Delta\omega_o) = e^{-i\pi\Omega_y}\hat{m}^p(\Delta\omega_o)e^{i\pi\Omega_y} \tag{5.47}$$

Rotations corresponding to the two cases are related by

$$R^p(\Delta\omega_o) = e^{-i\pi\Omega_y}R(-\Delta\omega_o)e^{i\pi\Omega_y} \tag{5.48}$$

In general, the pulse has a train of phases $\{\phi_1, \phi_2, \cdots, \phi_n\}$. If we make the change of phase $\{-\phi_1 + \pi, -\phi_2 + \pi, \cdots, -\phi_n + \pi\}$, it can be seen from Eq. 5.48, the overall rotations $R^p = R^p(1)R^p(2)\cdots R^p(n)$ and $R = R(1)R(2)\cdots R(n)$ are related by exactly the same way.

The magnetization created by R^p is

$$\begin{aligned}
\begin{bmatrix} M_x^p(0^+)(\Delta\omega_o) \\ M_y^p(0^+)(\Delta\omega_o) \\ M_z^p(0^+)(\Delta\omega_o) \end{bmatrix} &= R^p(\Delta\omega_o) \begin{bmatrix} 0 \\ 0 \\ 1 \end{bmatrix} \\
&= e^{-i\pi\Omega_y}R(-\Delta\omega_o)e^{-i\pi\Omega_y} \begin{bmatrix} 0 \\ 0 \\ 1 \end{bmatrix} \\
&= \begin{bmatrix} M_x(0^+)(-\Delta\omega_o) \\ M_y(0^+)(-\Delta\omega_o) \\ M_z(0^+)(-\Delta\omega_o) \end{bmatrix}
\end{aligned} \tag{5.49}$$

From Eqs. 5.44 and 5.49, the net magnetization that is the signal difference between the two runs of the initial excitation pulse and the phase modified excitation pulse is

$$\begin{aligned}\bar{M} =&(\vec{M}(0^+)\cdot\hat{n} - \vec{M}^p(0^+)\cdot\hat{n})\hat{n}_\perp \\ &[(M_y(\Delta\omega_o) + M_y(-\Delta\omega_o))\hat{n}_y(\Delta\omega_o) + (M_z(\Delta\omega_o) - M_z(-\Delta\omega_o))\hat{n}_z(\Delta\omega_o)]\hat{n}_\perp\end{aligned} \tag{5.50}$$

The term inside the square bracket is an even function of $\Delta\omega_o$. In addition $\hat{n}_\perp = \hat{n}_x + i\hat{n}_y = i\hat{n}_y$ is also even, so the total signal is symmetric with respect to the frequency offset.

5.7.3 Experimental verification

Experiments were carried out under the same conditions as described in Sec. 5.6.2. A perfect agreement between simulation and experimental data confirm the analysis and the effectiveness of the pulses.

As noted earlier, the echoes approach an asymptotic form after some transient state [63, 64]. From Eq. 5.2 it is clear that for a perfect matching case $\hat{n} = \vec{M}(0^+)$ there would be no transient. Our AMEX pulses make $n = \vec{M}(0^+)$ closely follow the profile of $\hat{n}$, therefore we would expect that there is less transient compared to the case where the excitation pulse is a rectangular pulse.

5.8 Conclusion

In conclusion, we have found practical refocusing and excitation pulses that more than triple the SNR. The refocusing pulse does not require any additional power compared to a rectangular 180° pulse. The $AMEX$ excitation pulses are less than

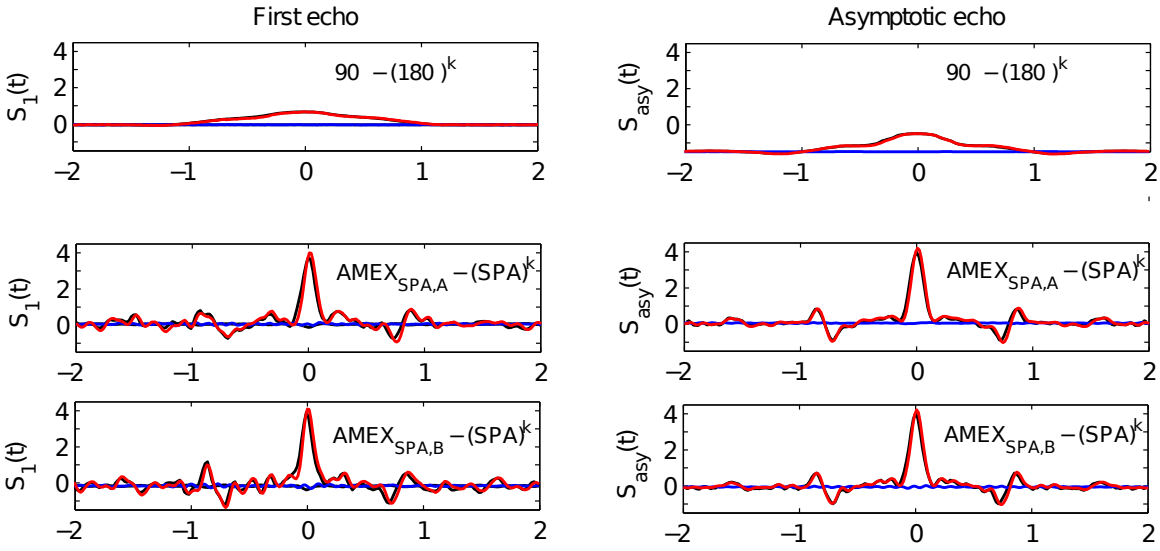

Figure 5.12: Echo shapes for different pairs of excitation and refocusing pulses. Black curves show the results obtained by simulation. Red curves are experimental data for the in-phase components. Blue curves are experimental data for the out-of-phase components, which are almost identically zero as expected. Data were taken with permission from the co authors in Ref. [3]

$16t_{180}$, which only require minimum increase in power since they are applied only once over a train of several thousand echoes.

We have also studied the how the SNR per unit power depends on pulse length. In particular, we have found that increasing the pulse length will increase the SNR but the SNR per unit power does not increase linearly with the pulse length, rather it peaks at a certain pulse length. This result will be reported in the forthcoming publication [71].

Some open problems are the role of symmetry in the pulse sequences and the trade offs between phase and amplitude modulation vs. pure phase modulation.

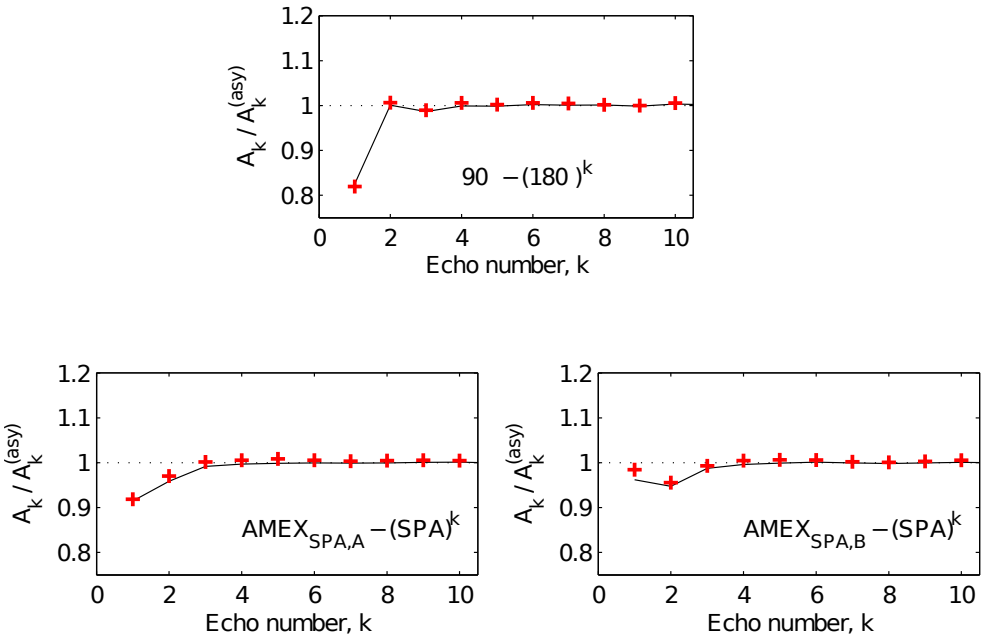

Figure 5.13: Amplitudes of the first ten echoes for different pairs of excitation and refocusing pulses. Solid lines show results obtained by simulation while red crosses show experimental results. Data were taken with permission from the co authors in Ref. [3].

Bibliography

[1] Van D. M. Koroleva, Soumyajit Mandal, Yi-Qiao Song, and Martin D. Hürlimann. Broadband cpmg sequence with short composite refocusing pulses. *J. Mag. Reson.*, 230:64–75, 2013.

[2] Van D. M. Koroleva and Navin Khaneja. Homonuclear decoupling for liquid-state nmr. *J. Chem. Phys.*, 137:094103, 2012.

[3] Soumyajit Mandal, Van Koroleva, Troy W. Borneman, Yi-Qiao Song, and Martin D. Hürlimann. Axis-matching excitation pulses for the CPMG-like sequences in inhomogeneous fields. *under review*, pages –, 2013.

[4] I.I. Rabi, J.R. Zacharias, S. Millman, and P Kusch. A New Method of Measuring Nuclear Magnetic Moment. *Phys. Rev.*, 53:318–327, 1938.

[5] F Bloch. Nuclear induction. *Phys. Rev.*, 70:460–474, 1946.

[6] E. M. Purcell, H. C. Torrey, and R. V. Pound. Resonance Absorption by Nuclear Magnetic Moments in a Solid. *Phys. Rev.*, 69:37–38, 1946.

[7] John Cavanagh, Wayne J. Fairbrother, Arthur G. Palmer, III, Mark Rance, and Nicholas J. Skelton. *Protein NMR Spectroscopy: Principles and Practices*. Elsevier Academic Press, 2007.

[8] Ray Freeman. *Magnetic Resonance in Chemistry and Medicine*. Oxford University Press, 2003.

[9] Robert L. Kleinberg and Jasper A. Jackson. An introduction to the history of nmr well logging. *Concepts in Magnetic Resonance*, 13:340–342, 2001.

[10] Martin D. Hürlimann. Well logging. *eMagRes.*, page DOI: 10.1002/9780470034590.emrstm0593.pub2, 2012.

[11] L. M. K. Vandersypen and I. L. Chuang. NMR techniques for quantum control and computation. *Rev. Mod. Phys.*, 76:10371069, 2005.

[12] Paola Cappellaro. *Quantum Information Processing in Multi-Spin Systems*. PhD thesis, Massachusetts Institute of Technology, 2006.

[13] R. Ernst, G. Bodenhausen, and A. Wokaun. *Principles of Nuclear Magnetic Resonance in One and Two Dimensions*. Clarendon Press, 1987.

[14] L. Childress, M. V. Gurudev Dutt, A. S. Zibrov, F. Jelezko, J. Wrachtrup, P. R. Hemmer, and M. D. Lukin. Coherent Dynamics of Coupled Electron and Nuclear Spin Qubits in Diamond. *Science*, 314:281–285, 2006.

[15] C A Ryan, J S Hodges, and D G Cory. Robust Decoupling Techniques to Extend Quantum Coherence in Diamond. *Phys. Rev. Lett.*, 105:200402, 2010.

[16] W. M. Witzel and S. Das Sarma. Multiple-Pulse Coherence Enhancement of Solid State Spin Qubits. *Phys. Rev. Lett.*, 98:077601, 2007.

[17] F Casnova, J. Perlo, and editors Blumich, B. *Single-Sided NMR*. Springer, 2011.

[18] O. W. Sörensen, G. W. Eich, M. H. Levitt, Bodenhausen G., and R. R. Ernst. Product operator formalisim for the description of NMR pulse experiment . *Prog. NMR. Spectrosc.*, 16:163–192, 1983.

[19] Roger W. Brockett. *Finite Dimensional Linear Systems*. John Wiley & Sons, 1970.

[20] Michael Baake and Ulrike Schlägel. The Peano-Baker Series. In *Proceedings of the Steklov Institute of Mathematics, Vol 275, pp. 155-159*. Pleiades Publishing, Ltd., 2011.

[21] Ray Freeman. *Spin Choreography: Basic steps in high resolution NMR*. Oxford University Press, 1998.

[22] Gordon S. Rule and T. Kevin Hitchens. *Fundamentals of Protein NMR Spectroscopy (Focus on Structural Biology)*. Springer, 2006.

[23] M. Goldman. *Quantum Description of High-Resolution NMR in Liquids*. Oxford University Press, 1988.

[24] A. J. Shaka, P. B. Barker, and Ray Freeman. Computer-Optimized Decoupling Scheme for Wideband Applications and Low-Level Operation. *J. Mag. Reson.*, 64:547–552, 1985.

[25] A. J Shaka, James Keeler, and Ray Freeman. Evaluation of a new broadband decoupling sequence: WALTZ-16. *J. Mag. Reson.*, 53:313–340, 1983.

[26] E. Kupce and R. Freeman. Adiabatic Pulses for Wideband Inversion and Broadband Decoupling. *J. Mag. Reson.*, 115:273–276, 1995.

[27] Z. Starcuk, K. Bartusek, and Z. Starcuk. Heteronuclear Broadband Spin-Flip Decoupling with Adiabatic Pulses. *J. Mag. Reson.*, 107:24–31, 1994.

[28] Riqiang Fu and Geoffrey Bodenhausen. Broadband decoupling in NMR with frequency-modulated 'chirp' pulse. *J. Mag. Reson.*, 245:415–420, 1995.

[29] Haribabu Arthanari, Gerhard Wagner, and Navin Khaneja. Heteronuclear decoupling by multiple rotating frame technique. *J. Mag. Reson.*, 209:8–18, 2011.

[30] Malcolm H. Levitt, Ray Freeman, and Tom Frenkiel. Supercycles for Broadband Heteronuclear Decoupling. *J. Mag. Reson.*, 50:157–160, 1982.

[31] Malcolm H. Levitt. Composite Pulses. *Prog. NMR Spect.*, 18:61, 1986.

[32] M. A. McCoy and L. Mueller. Selective shaped pulse decoupling in NMR: homonuclear [carbon-13]carbonyl decoupling. *J. Am. Chem. Soc.*, 114:2108–2112, 1992.

[33] Eriks Kupce and Gerhard Wagner. Multisite Band-Selective Decoupling in Proteins. *J. Mag. Resons. Series B*, 110:309–312, 1996.

[34] Eriks Kupce and Gerhard Wagner. Wideband Homonuclear Decoupling in Protein Spectra. *J. Mag. Resons. Series B*, 109:329–333, 1995.

[35] Philip Owrutsky and Navin Khaneja. Control of Inhomogeneous Ensembles on the Bloch Sphere. *Phys. Rev. A*, 86:022315, 2012.

[36] Michael A. Nielsen and Issac L. Chuang. *Quantum Computation and Quantum Information*. Cambridge University Press, 2000.

[37] Malcolm H. Levitt. *Spin dymanics: basics of Nuclear Magnetic Resonance*. John Wiley & Sons Ltd, 2001.

[38] J. R. Maze, J. M. Taylor, and M. D. Lukin. Electron spin decoherence of single nitrogen-vacancy defects in diamond. *Phys. Rev. B.*, 78:094303, 2008.

[39] R.W. Simmonds, K.M. Lang, D. A. Hite, S. Nam, D. P. Pappas, and John M. Martinis. Decoherence in Josephson Phase Qubits from Junction Resonators. *Phys. Rev. Lett.*, 93:077003, 2004.

[40] A. M. Zagoskin, S. Ashhab, J. R. Johansson, and Franco Noril. Quantum Two-Level Systems in Josephson Junctions as Naturally Formed Qubits. *Phys. Rev. Lett.*, 97:077001, 2006.

[41] A. Lupascu, P. Bertet, E. F. C. Driessen, C. J. P. M. Harmans, and J. E. Mooij. One- and two-photon spectroscopy of a flux qubit coupled to a microscopic defect. *Phys. Rev. B.*, 80:172506, 2009.

[42] Simon Gustavsson, Fei Yan, Jonas Bylander, Fumiki Yoshihara, Yasunobu Nakamura, Terry P. Orlando, and William D. Oliver. Dynamical Decoupling and Dephasing in Interacting Two-Level Systems. *Phys. Rev. Lett.*, 109:010502–, 2012.

[43] L. Viola and E. Knill. Random Decoupling Schemes for Quantum Dynamical Control and Error Suppression. *Phys. Rev. Lett.*, 94:060502, 2005.

[44] G. S. Uhrig. Keeping a Quantum Bit Alive by Optimized π-Pulse Sequences. *Phys. Rev. Lett.*, 98:100504, 2007.

[45] K. Khodjasteh and D. A. Lida. Fault-Tolerant Quantum Dynamical Decoupling. *Phys. Rev. Lett.*, 95:180501, 2005.

[46] K. Khodjasteh and D. A. Lida. Performance of deterministic dynamical decoupling schemes: Concatenated and periodic pulse sequences. *Phys. Rev. A*, 75: 062310, 2007.

[47] J. R. West, B. H. Fong, and D. A. Lidar. Near-Optimal Dynamical Decoupling of a Qubit. *Phys. Rev. Lett.*, 104:130501, 2010.

[48] Wang Z.Y. and Liu R.B. Protection of quantum systems by nested dynamical decoupling. *Phys. Rev. A*, 83:022306, 2011.

[49] M. Biercuk, H. Uys, A. VanDevender, N. Shiga, W. Itano, and J. Bollinger. Optimized dynamical decoupling in a model quantum memory. *Nature*, 458: 996–, 2009.

[50] M. Biercuk, H. Uys, A. VanDevender, N. Shiga, W. Itano, and J. Bollinger. Experimental Uhrig dynamical decouping using trapped ions. *Phys. Rev. A*, 79: 062324, 2009.

[51] Wang Yao, Ren-Bao Liu, and L. J. Sham. Restoring Coherence Lost to a Slow Interacting Mesoscopic Spin Bath. *Phys. Rev. Lett.*, 98:077602–, 2007.

[52] P. Wocjan. Efficient decoupling schemes with bounded controls based on Eulerian orthogonal arrays. *Phys. Rev. A.*, 73:062317, 2006.

[53] L. Viola and S. Lloyd. Dynamical suppression of decoherence in two-state quantum systems. *Phys. Rev. A*, 58:2733, 1998.

[54] J. S. Waugh, L. M. Huber, and U. Haeberlen. Approach to high-resolution NMR in solids. *Phys. Rev. Lett.*, 20:180, 1968.

[55] T. D. T. D. Ladd, D. Maryenko, Y. Yamamoto, E. Abe, and K. M. Itoh. Coherence time of decoupled nuclear spins in silicon. *Phys. Rev. B.*, 71:014401–, 2005.

[56] H. G. Krojanski and D. Suter. Reduced Decoherence in Large Quantum Registers. *Phys. Rev. Lett.*, 97:150503, 2006.

[57] Jasper A. Jackson. Los Alamos NMR Well Logging project. *Concepts in Magnetic Resonance*, 13:368–378, 2001.

[58] R. Freedman and N. Heaton. Fluid Characterization using Nuclear Magnetic Resonance Logging. *Petrophysics*, 45:241–250, 2004.

[59] M. D. Hürlimann. Diffusion and relaxation effects in general stray field nmr experiments. *J. Mag. Reson.*, 148:367–378, 20001.

[60] H. Y. Carr and E. M. Purcell. Effects of diffusion on free precession in nuclear magnetic resonance experiments. *Phys. Rev.*, 94:630–638, 1954.

[61] S. Meiboom and D. Gill. Modified spin-echo method for measuring nuclear relaxation times. *Rev. Sci. Instrum.*, 29:688–691, 1958.

[62] M. S. Grinolds, S. Hong, P. Malentinsky, L. Luan, M. D. Lukin, R. L. Walsworth, and A. Yacoby. Nanoscale magnetic imaging of a single electron spin under ambient conditions. *Nature Physics*, 9:215–219, 2013.

[63] G. Goelman and M. G. Prammer. The CPMG pulse sequence in strong magnetic field gradients with applications to oil-well logging. *J. Mag. Reson.*, 113:11–18, 1995.

[64] M. D. Hürlimann and D. D. Griffin. Spin dynamics of carr-purcell-meiboom-gill like sequences in grossly inhomogeneous b_o and b_1 fields and application to nmr well logging. *J. Mag. Reson.*, 143:120–135, 2000.

[65] N. Khaneja, T. Reiss, C. Kehlet, T. Schulte-Herbruggen, and S. J. Glaser. Optimal control of coupled spin dyanmis: design of nmr pulse sequences by gradient ascent algorithms. *J. Mag. Reson.*, 172:296–305, 2005.

[66] C. Counsell, M. H. Levitt, and R. R. Ernst. Analytical theory of composite pulses. *J. Mag. Reson.*, 63:133–141, 1985.

[67] A. J. Shaka and A. Pines. Symmetric phase-alternating composite pulses. *J. Mag. Reson.*, 71:495–503, 1987.

[68] Thomas E. Skinner, Timo O. Reiss, Burkhard Luy, Navin Khaneja, and Steffen J. Glaser. Application of optimal control theory to the design of broadband excitation pulses for high-resolution NMR. *J. Mag. Reson.*, 163:8–15, 2003.

[69] T. E. Skinner, K. Kobzar, B. Luy, M. R. Bendall, Bermel W., Navin Khaneja, and S. J. Glaser. Optimal control design fof constant amplitude phase-modulated pulses: Application to calibration-free broadband excitation. *J. Mag. Reson.*, 179:241–249, 2006.

[70] Kyryl Kobzar, Thomas E. Skinner, Navin Khaneja, Steffen J. Glaser, and Burkhard Luy. Exploring the limits of broadband excitation and inversion: II. RF-power optimized pulses. *J. Mag. Reson.*, 194:58–66, 2008.

[71] Soumyajit Mandal, Troy Borneman, Van D. M. Koroleva, and Martin Hürlimann. Performance limits of CPMG-like sequences in inhomogeneous fields (*in preparation*).